UNIVERSITY OF CALIFORNIA SAN DIEGO

SAN DIEGO STATE UNIVERSITY

Drosophila as a Model for Myosin-Induced Dilated Cardiomyopathy

A dissertation submitted in partial satisfaction of the
requirements for the degree Doctor of Philosophy

in

Biology

by

Adriana Sara Trujillo

Committee in charge:

San Diego State University

Professor Sanford I. Bernstein, Chair
Professor Tom Huxford, Co-chair
Professor Christopher C. Glembotski

University of California San Diego

Associate Professor Amy Kiger
Professor Deborah Yelon

2020

The Dissertation of Adriana Sara Trujillo is approved, and it is acceptable in quality and form for publication on microfilm and electronically:

_____

_____

_____

_____
Co-chair

_____
Chair

University of California San Diego

San Diego State University

2020

Dedication

This dissertation is dedicated in loving memory to my Nana (grandmother), Ernestine “Tina” Bleecker, whose life stories, passion for learning, and curious nature inspired me to pursue a career in life sciences.

Table of contents

List of figures

List of tables

Acknowledgements

I wish to thank Dr. Sanford Bernstein for giving me the opportunity to work in his lab. I am incredibly grateful for his support, patience, positive encouragement, and for always being available to provide experimental guidance and feedback. I also wish to thank my committee members, Drs. Tom Huxford and Chris Glembotski from SDSU, and Drs. Amy Kiger and Deborah Yelon from UCSD, for their support, wisdom, and guidance. I also acknowledge Dr. Huxford for providing instructional support for X-ray diffraction data collection and guidance in performing structural biology work.

The greatest pleasure during my doctoral studies was the opportunity to mentor the following undergraduate student researchers: Yusur AL-Qaraghuli performed analyses of cardiac physiology data. Hassler Rengifo and Julia Platter performed fly line validation experiments. Additionally, Mr. Rengifo assisted with fly husbandry and performed skeletal muscle functional tests. In addition to producing excellent work, they are all wonderful, positive individuals, and I foresee a bright future ahead of them.

I also wish to acknowledge the following individuals who made this work possible: Cryo-electron microscopy and negative staining trials of actomyosin were performed in collaboration with Drs. Dorit Hanein and Niels Volkmann (Sanford Burnham Prebys MDI). Dr. James Caldwell provided procedures and guidance for purifying the myosin motor domain in bulk from His-tagged flies. Dr. Karen Hsu provided ATPase data for S532P and R369H myosin. Jennifer Suggs and Floyd Sarsoza provided assistance in IFM microdissections for ATPase assays. Additionally, Ms. Suggs provided guidance in fly husbandry, fly crosses, and general lab procedures. William Kronert provided assistance and guidance in molecular cloning experiments. Joy Puthawala and Amy Loya provided mechanics data on isolated muscle fibers (collaboration with Dr. Douglas Swank, Rensselaer PI). Meera Viswanathan provided cardiac physiology data of 3 week-old heterozygous mutant flies (collaboration with Dr. Anthony

Cammarato, Johns Hopkins Medicine). Drs. Steven Barlow and Ingrid Niesman (SDSU EM Facility) provided guidance and technical support for TEM ultrastructure work.

This work was supported by an NIH NRSA F31 Predoctoral Fellowship, a Rees-Stealy Research Foundation Phillips Gausewitz, M.D. Scholar of the SDSU Heart Institute Fellowship, a SDSU Graduate Fellowship, and a scholarship from the Achievement Rewards for College Scientists (ARCS) San Diego Chapter.

Chapter 1, in full, contains unpublished material coauthored by Trujillo, Adriana S.; Bernstein, Sanford I. The dissertation author was the primary investigator and author of this chapter.

Chapter 2, in full, contains unpublished material coauthored by Trujillo, Adriana S.; Volkmann, Niels; Hanein, Dorit; Bernstein, Sanford I. The dissertation author was the primary investigator and author of this chapter.

Chapter 3, in full, contains unpublished material coauthored by Trujillo, Adriana S.; Puthawala, Joy; Hsu, Karen; Loya, Amy; Swank, Douglas; Bernstein, Sanford I. The dissertation author was the primary investigator and author of this chapter.

Chapter 4, in full, contains unpublished material coauthored by Trujillo, Adriana S.; Viswanathan, Meera; Cammarato, Anthony R.; Bernstein, Sanford I. The dissertation author was the primary investigator and author of this chapter.

Chapter 5, in full, contains unpublished material coauthored by Trujillo, Adriana S.; Hsu, Karen; Viswanathan, Meera; Cammarato, Anthony R.; Bernstein, Sanford I. The dissertation author was the primary investigator and author of this chapter.

Curriculum vitae

Education:

- Ph.D., Joint Doctoral Program in Cell and Molecular Biology, San Diego State University and UC San Diego, 2013-2020
- M.S., Cell and Molecular Biology, San Diego State University, 2010-2013
- B.S., Cell and Developmental Biology, California State University, Fullerton, 2006-2010

Research positions:

- Graduate Researcher- PI: Dr. Sanford I. Bernstein, San Diego State University, 2010-present
- Graduate Assistant- PI: Dr. Steven Barlow, SDSU EM Facility, San Diego State University, 2010-2011
- Undergraduate Researcher- PI: Robert A. Koch, CSU Fullerton, 2008-2010

Honors and Awards:

- University Graduate Fellowship from SDSU, 2018-2020
- Rees-Stealy Research Foundation Phillips Gausewitz, M.D., Scholars of the SDSU Heart Institute Research Fellowship, 2014-present
- NIH NRSA F31 Diversity Pre-doctoral Fellowship, 2015-2019
- SDSU Achievement Rewards for College Scientists (ARCS) Scholarship, 2017-present
- SDSU Cell and Molecular Biology Graduate Student Symposium Awards for Best Presentation and People's Choice, 2019
- SDSU Cell and Molecular Biology Graduate Student Symposium Best Poster "Golden Pipette" Award, 2014
- NIH Research Supplement to Promote Diversity in Health Related Research, 2011-2013
- SDSU Cell and Molecular Biology Graduate Student Symposium Most Collaborative Poster Award, 2016
- San Diego State University (SDSU) Student Research Symposium (SRS) Provost's Award, 2013
- Biophysical Society Minority Affairs Committee Travel Award recipient to present a poster for the 2013 Annual Meeting
- CSU Program for Education and Research in Biotechnology (CSUPERB) Student Travel Award recipient to present a poster at the 2013 Biophysical Society Annual Meeting
- Graduated Cum Laude, California State University, Fullerton, 2010
- CSUF Dean's list recipient: Fall 2007, Spring 2008, Spring 2009, and Fall 2009

Professional Memberships:

- Founder of the SDSU Initiative to Support Graduate Student Health and Wellness, 2019/2020
- SDSU Graduate Council, Doctoral Student Representative, 2017/2018 and 2018/2019
- SDSU MInDSET (Maximizing INclusion and Diversity in Science, Engineering, and Technology) member, 2017

Publications and Manuscripts:

1. **Trujillo, A. S.**, Hsu, K., Puthawala, J., Loya, A., Viswanathan, M., Cammarato, A., Swank, D. M. and Bernstein, S. I. Myosin dilated cardiomyopathy mutation S532P disrupts actomyosin interactions and reduces muscle function in Drosophila. Manuscript in preparation.
2. Villanueva, J.*, Livelo, C.*, **Trujillo, A. S.**, Chandran, S., Woodworth, B., Andrade, L., Le, H., Manor, U., Panda, S. and Melkani, G.C. Time-restricted feeding restores muscle function in Drosophila models of obesity and circadian-rhythm disruption. *Nature Communications* **10**, 2700 (2019). ***co-first authors**
3. Kronert, W. A., Bell, K., Viswanathan, M. C., Melkani, G. C., **Trujillo, A. S.**, Huang, A., Melkani, A., Cammarato, A., Swank, D. M., Bernstein, S. I. Prolonged cross-bridge binding triggers muscle dysfunction in a Drosophila model of myosin-based hypertrophic cardiomyopathy. *eLife* 7:e38064, (2018).
4. Bhide, S., **Trujillo, A. S.**, O'Connor, M. T., Young, G. H., Cryderman, D. E., Chandran, S., Nikravesh, M., Wallrath, L. L., Melkani, G. C. Increasing autophagy and blocking Nrf2 suppresses laminopathy-induced age-dependent cardiac dysfunction and shortened lifespan. *Aging Cell*, e12747, (2018).
5. Viswanathan, M. C., Tham, R. C., Kronert, W. A., Sarsoza, F., **Trujillo, A. S.**, Cammarato, A., Bernstein, S. I. Myosin storage myopathy rod mutations yield defective thick filament assembly *in vitro* and disrupted myofibrillar structure and function *in vivo. Human Molecular Genetics* 26(24): 4799-4813 (2017).
6. Achal, M.*, **Trujillo, A. S.***, Melkani, G. C., Farman, G. P., Ocorr, K., Viswanathan, M. C., Kaushik, G., Newhard, C. S., Glasheen, B. M., Melkani, A., Suggs, J. A., Moore, J. R., Swank, D. M., Bodmer, R., Cammarato, A., Bernstein, S. I. A restrictive cardiomyopathy mutation in an invariant proline at the myosin head/rod junction enhances head flexibility and function, yielding muscle defects in Drosophila. *Journal of Molecular Biology* 428(11), 2446-2461 (2016). ***co-first authors**
7. Kaushik, G., Spenlehauer, A., Sessions, A. O., **Trujillo, A. S.**, Fuhrmann, A., Fu, Z., Venkatraman, V., Pohl, D., Tuler, J., Wang, M., Lakatta, E. G., Ocorr, K., Bodmer, R., Bernstein, S. I., Van Eyk., J. E., Cammarato, A., and Engler, A. J. Vinculin network-mediated cytoskeletal remodeling regulates contractile function in the aging heart. *Science Translational Medicine* 7, 292ra99 (2015).
8. **Trujillo, A. S.**, Ramos, R., Bodmer, R., Bernstein, S. I., Ocorr, K., and Melkani, G. C. Drosophila as a potential model to ameliorate mutant Huntington-mediated cardiac amyloidosis. *Rare Diseases* 2:1 (2014).
9. Melkani, G. C., **Trujillo, A. S.**, Ramos, R., Bodmer, R., Bernstein, S. I., and Ocorr, K. Huntington's disease induced cardiac amyloidosis is reversed by modulating protein folding and oxidative stress pathways in the Drosophila heart. *PLoS Genetics* 9, e1004024, (2013).

Professional Presentations:

1. **SDSU Graduate Student Seminar-** February 2019- Oral presentation- "Structural and biochemical mechanisms of myosin-induced dilated cardiomyopathy"
2. **American Society for Cell Biology Annual Meeting, San Diego, CA**- December 2018- Poster- "Myosin dilated cardiomyopathy mutations S532P and R369Q weaken actin affinity and reduce muscle function in Drosophila models"
3. **San Diego Achievement Rewards for College Scientists (ARCS) Annual Dinner and Symposium**- October 2018- Poster- "Time-restricted Feeding Ameliorates Skeletal Muscle Dysfunction in a Fruit Fly Model for Human Obesity"

4. **SDSU Graduate Student Seminar-** February 2018- Oral presentation- "Drosophila as a model for myosin-induced dilated cardiomyopathy"
5. **SDSU/UCSD** Institutional Research and Academic Career Development Award (**IRACDA) Research Symposium**- April 2017- Poster- “Hypertrophic and dilated cardiomyopathy myosin mutations cause severe striated muscle defects in a Drosophila model”
6. **2017 Annual Drosophila Research Conference, San Diego, CA** - March 2017- Poster- “Hypertrophic and dilated cardiomyopathy myosin mutations cause severe striated muscle defects in a Drosophila model”
7. **SDSU Graduate Student Seminar-** March 2017- Oral presentation- "Structural mechanisms of myosin-induced dilated cardiomyopathy"
8. **Biophysical Society Annual Meeting, New Orleans, LA** - February 2017- Poster- A R146N hypertrophic cardiomyopathy myosin mutation disrupts myosin function, myofibrillar structure, and cardiac contraction in Drosophila”
9. **SDSU/UCSD CMB Joint Doctoral Proposal-** August 2016- Oral presentation- "Drosophila as a model for myosin-induced dilated cardiomyopathy"
10. **SDSU CMB Graduate Student Symposium**- April 2016- Poster- “Modeling the human K146N myosin hypertrophic cardiomyopathy mutation in Drosophila disrupts myosin function, myofibrillar structure, and cardiac contraction”
11. **American Society for Cell Biology Annual Meeting, San Diego, CA**- December 2015- Poster- “Modeling the human K146N myosin hypertrophic cardiomyopathy mutation in Drosophila disrupts myosin function, myofibrillar structure, and cardiac contraction”
12. **SDSU Graduate Student Seminar-** February 2016- Oral presentation- "Structural bases of myosin-induced dilated cardiomyopathy"
13. **SDSU Graduate Student Seminar-** March 2015- Oral presentation- "Drosophila as a model for myosin-induced dilated cardiomyopathy"
14. **UCSD Fly Club Meeting**- December 2014**-** Oral presentation- “Characterization and suppression of Huntingtin-mediated cardiac amyloidosis”
15. **SDSU Graduate Student Seminar**- April 2014- Oral presentation- “Oxidative stress in the Drosophila heart”
16. **SDSU CMB Graduate Student Symposium**- April 2014- Poster- "Modulation of oxidative stress and protein folding pathways suppress Huntington's Disease induced cardiac defects in Drosophila*"*
17. **2014 Annual Drosophila Research Conference, San Diego, CA**- April 2014- Poster- "Tau-induced mitochondrial dysfunction mediates cardiomyopathy in a Drosophila model"
18. **SDSU CMB Master’s Thesis Defense**- May 2013- Oral presentation- “Exploration and suppression of tau-induced cardiomyopathy in a Drosophila model”
19. **SDSU Student Research Symposium**- March 2013- Poster- "Exploration and suppression of tau-induced cardiac and skeletal muscle defects in a Drosophila model"
20. **Biophysical Society Annual Meeting, Philadelphia, PA**- February 2013- Poster- "Exploration and suppression of tau-induced cardiac and skeletal muscle defects in a Drosophila model"
21. **25th Annual CSU Biotechnology Symposium, Anaheim, CA**- January 2013- Poster- "Exploration and suppression of tau-induced cardiac and skeletal muscle defects in a Drosophila model"
22. **SDSU CMB Master’s Thesis Proposal-** April 2012- Oral presentation- "Ultrastructural properties of Drosophila striated muscle as a model for cardiac disease"
23. **SDSU Student Research Symposium**- March 2012- Poster- "Ultrastructural properties of Drosophila striated muscle as a model for cardiac disease"

Abstract of the Dissertation

Drosophila as a Model for Myosin-Induced Dilated Cardiomyopathy

by

Adriana Sara Trujillo

Doctor of Philosophy in Biology

University of California San Diego, 2020

San Diego State University, 2020

Professor Sanford I. Bernstein, Chair

Dilated cardiomyopathy (DCM) leads to cardiac contractile deficits and pathological dilation of the left ventricle, which may result in heart failure. Inherited DCM can be caused by mutations in contractile proteins (e.g. myosin). Though myosin DCM mutations are generally thought to reduce myosin function, the structural and molecular origins leading to cardiac dilation are not well understood. Here, we took advantage of the powerful genetic tools available in Drosophila to generate the first fly models of myosin-induced DCM and determine the mechanistic basis of disease. The S532P and R369H mutations, located within the actin-binding region at residues mutated in DCM patients, were introduced into Drosophila myosin heavy

chain. We implemented an integrative approach to determine how these mutations disrupt intramolecular interactions and cause biochemical, structural and physiological defects in muscles. Given the location of these mutations within known actin binding sites, we hypothesized that they cause DCM by disrupting actomyosin interactions, leading to reduced myosin motor function and hypo-contractility of muscles.

To define the exact intramolecular interactions disrupted by the S532P DCM mutation, we are using cryo-electron microscopy to solve the structure of the mutant motor domain bound to F-actin. Preliminary analyses of negatively stained samples suggest that the S532P mutation disrupts the transition from weak to strong actin binding. Biochemical and muscle mechanics experiments revealed that the S532P mutation leads to depressed power output by increasing the rate of actin detachment and reducing and the rates of actin binding and actin-dependent enzymatic activity. Additionally, the R369H mutation reduces maximal actin binding *in vitro*. Both mutations reduce skeletal muscle function, suggesting that these myosin forms are underfunctional. *S532P* mutant hearts exhibit a dilated phenotype, which may compensate for reduced myosin function by preserving cardiac output.

Overall, and in support of our hypothesis, the S532P and R369H mutations impair actomyosin interactions and thereby decrease muscle function. These studies provide insight into the molecular basis by which contractile deficits induced by mutations of these residues in humans lead to compensatory enlargement of the left ventricle. Future work will exploit our fly models for drug screening to provide insight into potential therapeutic treatments for human patients.

Chapter 1: General introduction

1.1. Myosin-induced dilated cardiomyopathy

Dilated cardiomyopathy (DCM) is a heart disease involving weakening of the heart, leading to pathological ventricular dilation and wall thinning.[1] DCM can be caused by environmental and lifestyle factors, as well as genetic factors. Hereditary DCM commonly involves point mutations in genes essential for heart function, including myosin.[2]

Myosin II molecules serve as the molecular motor of striated (cardiac and skeletal) muscles.[3] Striated muscles contain hundreds to thousands of cylindrical myofibrils, each composed of numerous repeating sarcomeres as their functional contractile units. The structure of the sarcomere contains thick filaments mainly composed of myosin (Fig. 1.1A- blue) and thin filaments mainly composed of actin (Fig. 1.1A- red). Fig. 1.1A' shows an electron micrograph of a Drosophila indirect flight muscle sarcomere. The electron-dense boundaries of the sarcomeres are called Z-disks. Alpha-actinin crosslinks the barbed (+) ends of the thin filaments to the Z-disks. Myosin rods are packed in an antiparallel fashion relative to the center of the sarcomere (M-line). The area containing thick filaments is the A-band. The I-bands adjacent to the Z-disks contain thin filaments and are devoid of thick filaments. During muscle contraction, the thick filaments interact with thin filaments to allow filament sliding and sarcomere shortening, causing the I-bands to shorten and the Z-disks to come closer together. This process is dependent on ATP hydrolysis by myosin.

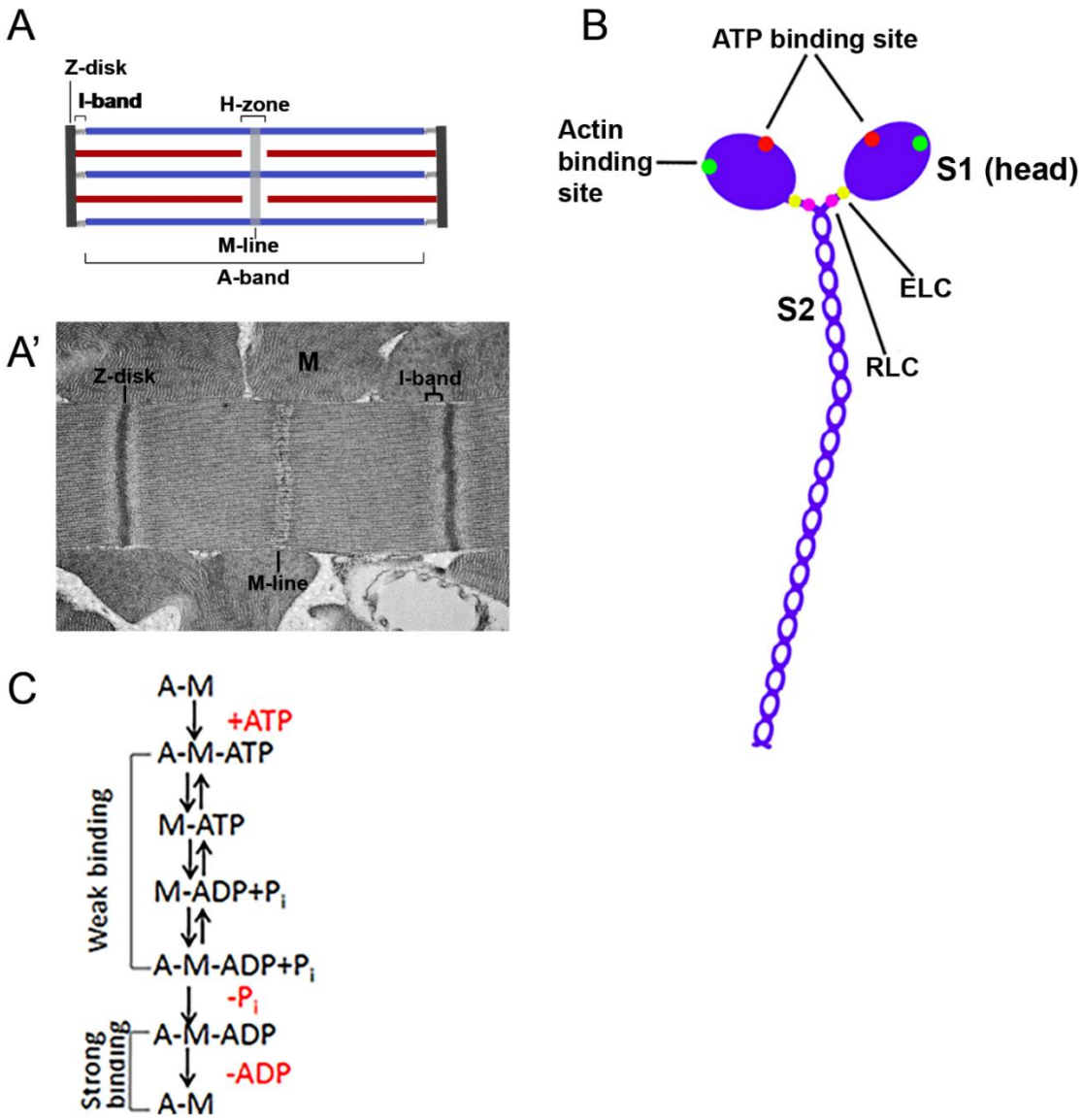

Figure 1.1- Introduction of sarcomere structure, myosin structure, and the actomyosin crossbridge cycle

A) Illustration of a sarcomere **(A)** and corresponding transmission electron microscopy (TEM) micrograph **(A')** in longitudinal orientation in Drosophila indirect flight muscle (IFM) in 2 day-old flies. Blue- thick myosin filaments; red- thin actin filaments, M-mitochondrion. **B)** Illustration of a myosin II molecule. The S1 (head) domain contains both the actin binding site and ATP binding pockets. The S2 domain contains a coil-coiled rod. RLC- Regulatory light chain. ELC- Essential light chain. **C)** Steps of the myosin ATPase cycle. Strong binding of myosin (M) to actin (A) occurs during the ADP bound state following Pi release, and in the nucleotide-free rigor state.

The structure of the myosin II molecule is shown in Fig. 1.1B. Each myosin II molecule contains two myosin heavy chains (MHCs), each with a globular head and an α-helical coiled-coil rod [reviewed by Geeves and Holmes[4]]. An assembly of α-helical coiled rods form the backbone of the myosin thick filament. The globular portion of the head is the motor domain (also known as subfragment-1, S1), which can bind actin and exhibits ATPase activity. The actin-binding cleft separates the upper and lower 50 kDa subdomains and is thought to close during the transition from weak to strong binding. Mutations causing disruptions in the structure of the head domain, including those that interfere with actin binding, can produce severe contractile defects.[5] Each heavy chain associates with an essential light chain and a regulatory light chain at the neck region. The lever arm, which extends from the neck to the base of the head, regulates the position of the myosin motor domain as it interacts with the actin filament.

The interactions between myosin and actin are coupled to the nucleotide state of the myosin motor.[6,7] In a model depicting the actomyosin crossbridge cycle (Fig. 1.1C), weak binding to actin occurs when ATP or the products of ATP hydrolysis (ADP+P_i) are bound, whereas strong binding occurs when ADP is bound or in the rigor state (A-M) after ADP dissociates. Thus, myosin is strongly attached to actin during the nucleotide-free rigor state until ATP binding results in detachment. Subsequent hydrolysis of ATP causes the myosin head to reorient, allowing binding to a different actin subunit. The release of P_i and ADP results in a rotation of the myosin head relative to the thin filament, causing the lever arm to drag forward and actin filaments to slide past myosin filaments towards the middle of the sarcomere.

DCM mutations in the *MYH7* gene encoding human β-cardiac myosin heavy chain (β-MyHC) often disrupt intramolecular interactions essential for proper protein function and decrease contractility.[5,8] Myosin functional deficits often result in decreased force generation due to altered actomyosin interactions or impaired ATP binding.[9,10] Distinct step(s) of the ATPase cycle can be altered by different myosin DCM mutations, depending on the mutation

location within the motor domain and the nature of the amino acid change.[2,8] Initial cardiac dilation is thought to compensate for contractile deficits and reduced cardiac output by increasing the amount of blood pumped through the heart. However, further dilation can cause pathological cardiac remodeling in which the heart walls become thin and weak. This pathological dilation can reduce cardiac output and lead to heart failure. In contrast, myosin-induced hypertrophic cardiomyopathy (HCM), a disease which causes the heart walls to become thickened, generally involves increases in myosin function and contractility. Myosin-induced restrictive cardiomyopathy (RCM), which causes impaired ventricular relaxation, is thought to share a common mechanism with HCM, resulting in increased contractility [reviewed by Lu et al.[11]]. Overall, differing effects on cardiac myosin performance can cause distinct cardiac remodeling events. We previously explored the mechanistic basis of myosin-induced HCM[12] and RCM[13] using the Drosophila (common fruit fly) model system. Here, we aim to generate the first Drosophila models for myosin-induced DCM to better understand how these mutations cause the disease.

1.2. Drosophila as a model for heart disease

Drosophila is a useful model because organisms are easy to culture, have a short generation time, a well-defined life cycle, and are amenable for transgenic manipulation.[14] Furthermore, the availability of balancer chromosomes facilitates the generation of stable lines by preventing homologous recombination and allowing for the identification of mutant alleles using phenotypic markers. Drosophila are useful as a model for human disease, since there are known Drosophila orthologs for 77% of human disease genes.[15] Drosophila have proven useful for exploring cellular pathways involved in disease and for drug target discovery via high throughput screening.[16]

Drosophila is an attractive model to determine the mechanistic basis of myosin-induced DCM. In contrast to vertebrates, which contain complex multigene myosin families, Drosophila

contain a single-copy myosin (*Mhc*) gene, making it a simple model to study myosin muscle diseases (myopathies).[17] Drosophila *Mhc* contains 19 exons, 5 of which are alternatively spliced to produce multiple protein isoforms.[18] Drosophila serves as an excellent model for expression and isolation of myosin from indirect flight muscles (IFMs) of the thorax for biochemical and structural studies.[19] Additionally, IFMs contain a highly ordered array of myofibrils similar to human skeletal muscles and their functional impairment can be readily assessed *in vivo* by flight testing.[20] Thus, we exploited the IFM system to define the structural, biochemical, cell biological, and functional defects caused by DCM-associated myosin mutations predicted to perturb actin binding (see Chapters 2, 3, and 5). Drosophila is further useful for studying heart disease since many genes controlling heart differentiation and function (e.g., the differentiation factor Tinman/Nkx 2.5, the contractile protein myosin) in Drosophila are evolutionarily conserved [reviewed by Bier and Bodmer[21]]. The dorsal vessel in Drosophila includes the heart, which is composed of a simple tube-like structure located in the abdomen.[21] Drosophila heart function can be severely perturbed without compromising viability, since flies also utilize a tracheal respiration system to deliver oxygen directly to tissues. We further exploited our fly models to investigate the cardiac physiological and ultrastructural defects associated with the expression of myosin DCM mutations (see Chapters 4 and 5).

1.3 Significance

Dilated cardiomyopathy (DCM) affects approximately 36 of 100,000 persons in the US.[10] Point mutations in sarcomeric proteins (e.g. myosin) have been suggested to cause familial DCM in approximately 10% of cases and are typically inherited in an autosomal dominant fashion.[5] The molecular mechanisms by which myosin mutations lead to contractile defects and pathological remodeling (e.g. cardiac dilation) are not well known. Here, we exploited the efficiency of germline transformation in Drosophila and a plethora of techniques implemented by our lab and our collaborators to better understand disease mechanisms. We determined how

interruptions in interactions important for actin-binding correlate to myosin defects at the biochemical level and to overall structural and functional changes in muscles. We also assessed whether defects in the Drosophila heart correlate with disease severity observed in humans. The development of successful Drosophila models for myosin-based DCM will be useful for high-throughput screening to determine if the Drosophila heart dilates in response to other myosin mutations found in patients with DCM. Since DCM patients with myosin mutations may harbor mutations in other proteins important for muscle function [reviewed by Mestroni and Taylor[22]], an efficient screening system will be highly useful to predict which mutations are causative of disease. Overall, our integrative models provide a broad-based understanding of the molecular origins and physiological basis of myosin-induced DCM.

Chapter 1, in full, contains unpublished material coauthored by Trujillo, Adriana S.; Bernstein, Sanford I. The dissertation author was the primary investigator and author of this chapter.

Chapter 2: Determine whether myosin DCM mutation S532P interrupts interactions important for actin binding

2.1. Introduction

2.1.1. S532P *MYH7* mutation

There were several criteria for choosing an *MYH7* human DCM mutation to model in Drosophila. To generate a relevant disease model, we ensured that the residue of interest is conserved between *MYH7* and Drosophila *Mhc.* Mutation of a constitutive exon was chosen to study the effects of the mutations on different myosin isoforms. We chose a mutation located in subfragment-1 (S1) to explore the structural basis of disease via X-ray crystallography or electron microscopy. The X-ray crystal structure of the globular S1 domain (PDB ID#: 5W1A) has been solved in our lab in collaboration with Dr. Tom Huxford (SDSU), and by other groups ([23-25]). Additionally, the structure of the complex of S1 bound to F-actin has been solved by negative staining[26] and cryo-electron microscopy.[27-29] We were particularly interested in a mutation that localizes to an actin binding site, since it is a well-characterized functional region of the motor that is essential for contractility. To determine whether findings from our fly models correlate to mouse models and the human condition, we sought to model a mutation that was previously modeled in mice and well-characterized phenotypically in humans. For these reasons, we chose to model the β-MyHC S532P DCM mutation in Drosophila.

Several DCM patients harboring the S532P mutation have been described.[5,9] In a mouse model of DCM, animals expressing S532P in α-cardiac MyHC (the major cardiac isoform in adult mice) exhibited progressive left ventricular (LV) dilation in heterozygotes and early onset cardiac dilation along with contractile deficits in homozygotes, suggesting a DCM-causative and gene dose-dependent role of the mutation.[30] Genetic testing in patients revealed that the mutation is caused by a T→C transition at nucleotide position 1680 of *MYH7.*[5] The location of the conserved S532P residue (Fig. 2.1- green residue, boxed inset) is modeled on the crystal structure of chicken skeletal muscle myosin II in the post-rigor configuration.[25] This structure was chosen for modeling due to well-documented binding sites for actin.[25,31-33] However, we

verified the presence of structurally-conserved regions containing the residue of interest in the human β-cardiac myosin heavy chain isoform (β-MyHC, PDB ID#: 4DB1) and Drosophila embryonic MHC isoform (PDB ID#: 5W1A) crystal structures. The β-MyHC S532 residue (*D. melanogaster* MHC S531) is located within an actin binding site (red) in an α-helix in the lower 50-kd conserved subdomain.[25] Kamisago et al. predicted that the S532P mutation interrupts the α-helical structure and disrupts actin binding.[5] Since the S532P mutation is located in a structurally conserved actin binding region, we predict that changes in the structure of the Drosophila indirect flight muscle isoform (IFI) would result in biochemical alterations in myosin function that are relevant to the changes that occur in cardiac tissues.

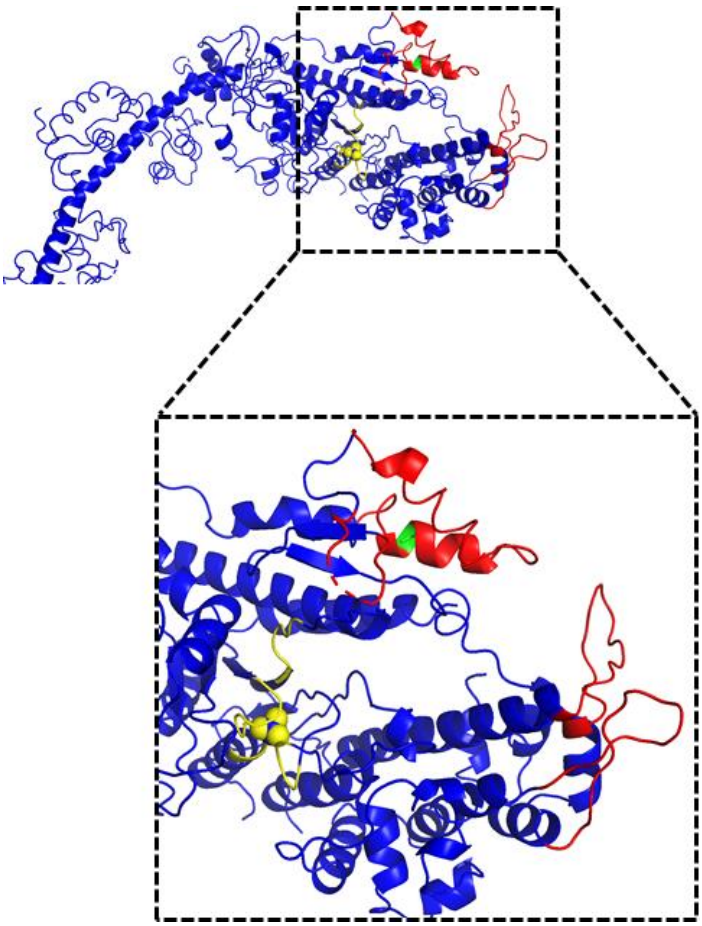

Figure 2.1- The location of the S532P myosin residue within an actin binding region of the motor domain.
The β-MyHC S532 residue (green) was modeled on the crystal structure of chicken skeletal muscle myosin II in the post-rigor configuration (PDB ID: 2MYS). Red- actin binding sites. Yellow- ATP binding pocket.

2.1.2. Hypothesis and goal

Given the location of the S532 residue within an actin binding region of the motor domain, we hypothesized that the S532P mutation interrupts interactions important for actin binding. To test this hypothesis, we sought to examine specific structural changes induced by this mutation using X-ray crystallography and electron microscopy.

2.1.3. Introduction to X-ray crystallography and transmission electron microscopy

We initially sought to determine structural changes induced by the mutation using X-ray crystallography. This method involves the formation of protein crystals, which contain a highly ordered array of protein molecules in a periodic lattice.[34] Upon treatment with an X-ray beam, diffraction is observed when radiation is scattered by the atoms in the lattice to form a series of spots, called reflections. Each reflection represents a wave of electromagnetic radiation, each with an associated amplitude and phase. The intensities of the reflections are related to the amplitudes of the waves. However, the phase information is lost during data collection, and must be calculated experimentally. In molecular replacement, a previously solved structure that is predicted to be highly similar to the unknown structure is repositioned to obtain the best agreement with the data set. After solving the phase problem, an electron density map is generated. Atoms are fit individually into the electron density map to obtain an atomic model. Through a series of refinements, the preliminary model is refined against the experimental data until there is a high degree of agreement between the data and the model. The generation of a protein crystal with good diffraction is often the major hurdle in crystal structure determination.[35] Crystal formation involves the association of protein molecules in three dimensions to form a nucleus, followed by the addition of protein molecules in a highly ordered fashion. Crystallography involves screening for reservoir solutions that promote crystal nucleation and

growth. Precipitants are added to these solutions to draw water away from the protein molecules and increase the supersaturation of the system, allowing the protein molecules to associate. Salts are often added to enhance protein solubility. Too much supersaturation can cause precipitation of the protein and impede nucleation and crystal growth. Alternatively, it can cause excessive nucleation and lead to the formation of small microcrystals that are not amenable for data collection. If crystal drops remain undersaturated after extensive incubation, nucleation may not occur. Under ideal conditions following nucleation, the free protein concentration in the drop is lowered, allowing crystal growth but not permitting further nucleation events. Thus, finding a condition that promotes growth of a single large crystal is challenging, and can require extensive screening.

Transmission electron microscopy (TEM) involves placing a sample under a high vacuum, and running a focused electron beam through the sample, so that the electrons interact with it.[36] The transmitted signal is focused, magnified, and the signal is converted to photons. The resulting image shows the electron density of the sample. Single particle analysis is a common TEM-based approach for structure determination.[37] It involves collecting large data sets, selecting particles of interest, and performing 2-dimensional and 3-dimensional alignments to reconstruct a model. The maximum resolution achieved by this approach is variable, and depends on the method employed for sample preparation, data collection, and model building. In negative staining TEM, an electron dense stain is used to coat the surface and surroundings of the sample. Negative staining structures generally have a maximum resolution of 20 Å, which is limited by the grain size of the staining reagent.[38] Cryo-electron microscopy, which involves freezing samples under their native state to protect against damage from the electron beam, can typically achieve resolutions of 6-10 Å, with some structures reaching near atomic resolution.[39,40]

Though the resolution can be limited compared to the atomic-level resolution obtained via X-ray crystallography, TEM is an attractive option for myosin structure determination. TEM

can be used to determine the structure of the actomyosin complex, as attempts to crystallize the complex have not been successful.[41] This is particularly advantageous for the S532P mutation, which resides in the actin-binding interface of myosin. Unlike TEM, X-ray crystallography requires the extensive screening for crystals with high resolution diffraction. Each protein form can crystallize under distinct conditions, making it challenging to make structural comparisons between the mutants and controls. To form crystals, protein samples are often treated with precipitants, harsh detergents, or additives that are not normal components of the myofibril, making it unknown whether the proteins crystallize in a conformation that is biologically relevant.[35] In contrast, TEM involves fixing proteins in solutions that have been optimized for protein stability and activity. For these reasons, and because adequately diffracting crystals were not obtained upon screening, we sought to use a TEM-based approach to form the actomyosin complex and determine the structural basis of disease.

2.2. Materials and Methods

2.2.1. Generation of a mutant His-tagged myosin line

Myosin quantities sufficient for biochemical studies have been isolated from microdissected IFMs due to high expression levels of myosin and large size relative to other Drosophila muscles.[42,43] However, milligram quantities of protein are essential for effective crystallization screening, which is difficult to achieve by primary dissection. To bypass the need for dissection, our lab expressed, isolated and purified His-tagged embryonic myosin from IFMs of >20000 homogenized flies per preparation using a series of salt-based extractions and Ni-column chromatography.[19] In conjunction with Dr. Tom Huxford (SDSU), our group used the purified embryonic myosin protein to solve the first X-ray crystal structure of an insect muscle myosin (PDB ID#:5W1A). The IFM-specific myosin isoform (IFI) has also been crystallized and had its structure determined (manuscript in preparation). For the current study, we generated a fly line expressing a His-tagged mutant version of IFI for structural studies.

To generate a mutant construct, we utilized a pAttB 6HisIFI plasmid previously produced by our lab, which contains the IFM-specific Actin-88F promoter, an amino-terminal His-tag, a tobacco etch virus (TEV) protease recognition site (for removal of the His-tag), cDNA encoding the IFI motor domain, as well as genomic DNA encoding MHC exons 12-19 along with their affiliated introns and polyadenylation sites. The cloning strategy for the S532P construct is shown in Fig. 2.2. For the first two steps, subclones containing *Mhc* exon 10 were generated from the larger plasmid. Oligonucleotide-directed mutagenesis was performed (QuikChange kit, Stratagene) to change the codon in Drosophila *Mhc* that corresponds to the *MYH7 S532P* nucleotide transition. The following forward (+) and the reverse (-) primers were used:

S532P (+): 5'-TCTTCCTCCAGGATGGGCAAGATACCCATGGTG-3'

S532P (-): 5'-CACCATGGGTATCTTGCCCATCCTGGAGGAAGA-3'

The mutated exon was sequenced for confirmation and inserted into a larger cloning intermediate. The entire construct was removed and ligated into a pAttB vector containing a *miniwhite* (w^+) selectable eye color marker that restores eye color in a white-eyed genetic background, as well as PhiC31 integrase AttB recognition sites. The final clone was purified using the QIAfilter Plasmid Maxi Kit (Qiagen Inc.) and sequenced for verification by Eton Bioscience. Targeted insertion was performed by Bestgene Inc. using the PhiC31-mediated transgenesis system.[44] One transgenic line containing a third chromosome targeted insert was produced.

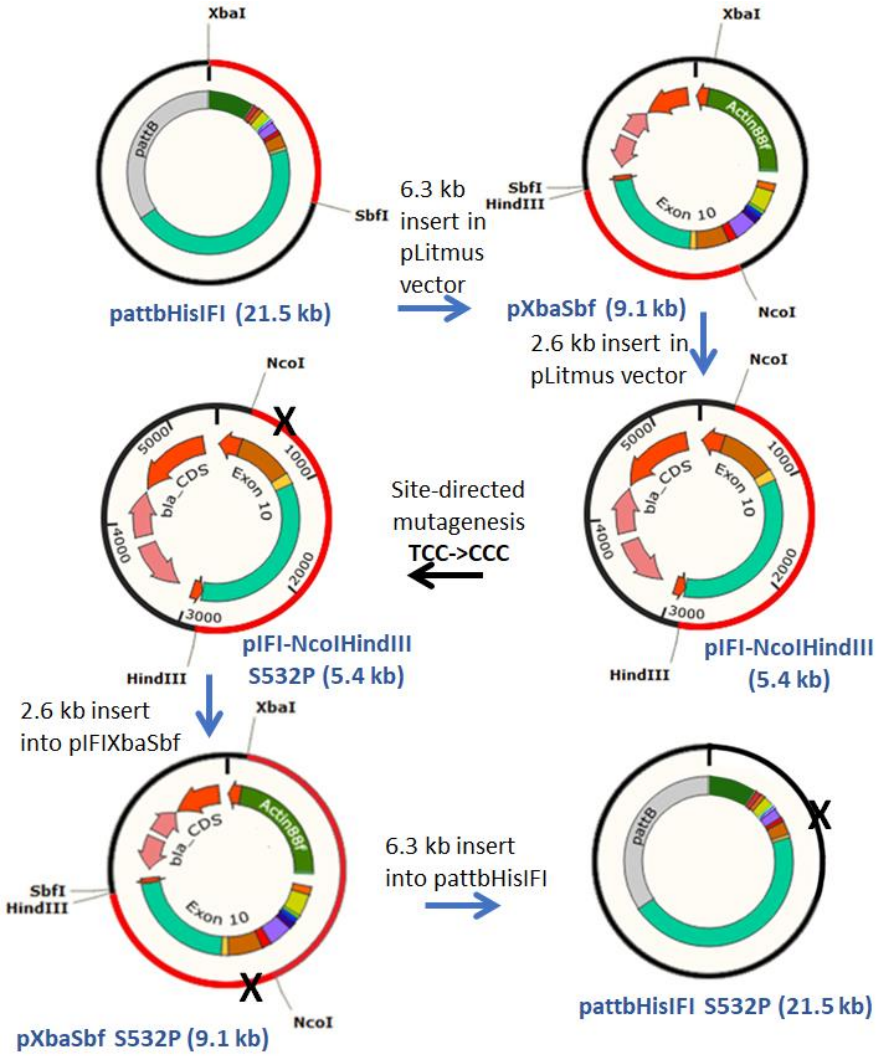

Figure 2.2- Cloning scheme for the 6HisIFI S532P construct
The sequential steps of restriction enzyme (RE) digestion and ligation are shown by the blue arrows. Each insert generated by *RE* digestion of the parent vector is shown in red, along with RE cut sites. Site-directed mutagenesis (black arrow) was performed to change the encoded serine residue to a proline residue at the 531st amino acid coding position of Drosophila *Mhc* (corresponding to position 532 in human *MYH7*). The mutant construct was ligated into a pAttB vector for targeted insertion by Bestgene, Inc using the PhiC31 transgenesis system.

Transgenic flies were crossed into a *Mhc*^{10} background that is null for endogenous myosin in IFMs.[45] Myosin protein levels are expressed at ~78% relative to wild-type *yw* flies in upper thoraces, as determined by SDS-PAGE and densitometry analysis.[46] RT-PCR was employed to verify that the Mhc transcripts produced by this line contain the appropriate nucleotide transition. For this, RNA was isolated from 2 day-old upper thoraces using the RNeasy kit by Qiagen, Inc. The Protoscript cDNA synthesis kit was employed to generate cDNAs, using 500 ng RNA and 100 ng of the specific reverse (-) primer shown below. The following primers were used for PCR amplification:

(+) 5'-TCTGGATACCCAGCAGAAGCGT-3'

(-) 5'-CAGCTGGTGCATGACCAAGTGGGC-3'

PCR was performed using 3 µL cDNA and 200 ng of each forward and reverse primer, under the following conditions: 120 sec at 98° C, then 30 cycles of: 20 sec at 98° C, 30 sec at 55° C and 2 min at 68° C. RT-PCR products were sequenced by Eton Bioscience.

2.2.2. Protein purification

Bulk S1 was purified from His-tagged flies using a procedure modified from Caldwell et al[19]:

1) Clarifying the supernatant and myosin extraction: Adults (<1 day-old) were collected daily, flash frozen using liquid nitrogen, and stored at -80°C. A total of 36 grams of flies was divided between two tubes and homogenized (OMNI International Homogenizer and 10 mm stainless probe) in a low salt homogenization buffer [HB, 0.5 % Triton X-100, Roche complete protease inhibitor cocktail tablets (1 tablet / 50 mL solution), 12.5% sucrose, 40 mM NaCl, 10 mM imidazole-Cl, 2 mM $MgCl_2$, 0.2 mM EGTA, and 1 mM DTT, at pH 7.2]. The charged amino acid residues of the myosin rod allow precipitation or solubilization of myosin in solutions of low or high ionic strength, respectively.[47] Prior to solubilization of myosin, a series of centrifugation steps (Beckman Ti-45 rotor, 40,000 RPM, 1.5 hours each, 4°C) were performed to clarify the soluble portion of the

homogenate. The supernatants were discarded following each centrifugation. Following the first two centrifugations, the pellets containing the insoluble myosin were homogenized in HB. After the third centrifugation step, the pellets were homogenized in high-salt myosin extraction buffer (MEB, 500 mM NaCl, 20 mM sodium phosphate buffer, 20 mM imidazole-Cl, pH 7.2), sonicated with 50 brief pulses at setting 5, 50% duty cycle (Fisher Scientific Sonic Dismembrator Model 100, micro tip), and incubated for 30 minutes on ice. Following centrifugation (Beckman Ti-45 rotor, 40,000 RPM, 40 minutes, 4°C), the pellets containing the exoskeleton and cellular debris were discarded. The soluble portions were diluted with a no salt solution to 75 mM NaCl, incubated for 4 hours on ice to precipitate myosin, and centrifuged (Beckman Ti-45 rotor, 40,000 RPM, 40 minutes, 4°C). The pellets were resuspended in 60 mL MEB (OMNI International Homogenizer with plastic tip) and the extracted myosin was filtered and further diluted with 390 mL MEB.

2) Ni column chromatography: His-tagged myosin was purified using Ni-affinity chromatography (HisTrap HP 5 mL column and ÄKTA pure system by GE Life Sciences). Following sample binding, the Ni column was washed with 30 mL MEB, and the sample was eluted in 30 mL elution buffer (500 mM NaCl, 20 mM sodium phosphate buffer, 250 mM imidazole-Cl, pH 7.4). His-tagged myosin was collected in 2 x 2 mL peak fractions, and myosin was precipitated by diluting with a no salt solution to 94 mM NaCl.
3) Purification of myosin motor domain (S1): Precipitated myosin was centrifuged (Beckman TLA-100.3 rotor, 68,000 RPM, 50 minutes, 4°C), and pellets were resuspended in digestion buffer (120 mM NaCl, 20 mM NaPi, 1 mM EDTA, 4 mM DTT, pH 7.0). The S1 fragment was clipped using α-chymotrypsin (Worthington Biochemical Corp., 0.18 mg/mL per 67.8 activity units, 6 minutes, 20°C), which was previously shown to also remove the His-tag at the TEV cut site.[19] To quench the reaction, phenylmethylsulfonyl fluoride was added to a final concentration of 1.50 mM. Samples

were centrifuged (Beckman TLA-100.3 rotor, 68,000 RPM, 50 minutes, 4°C) to remove insoluble rod fragments and uncut myosin from the soluble S1 fraction. To further purify S1, size exclusion chromatography was performed using the ÄKTA Pure system with a 16/600 column packed with Superdex 200. A centrifugal filter (Amicon Ultra-4 mL 10,000 MWCO) was used to concentrate peak S1 fractions to 2-6 mg/mL.

2.2.3. X-ray crystallography screening

A TTP Labtech Mosquito robot was employed to facilitate accurate and precise pipetting of small 100 nL sample volumes in a high-throughput fashion. Crystallization trials were initiated using reservoir conditions similar to those employed by our lab to crystallize non-mutant S1 in the presence of ADP. This did not result in successful crystal formation. Commercially available screens were then used to screen numerous (>5000) broad conditions with different nucleotides (ADP, the non-hydrolyzable ATP analog AMP-PNP, apo). For this, the Mosquito was employed to generate 200 nL sitting drops using 1:1 drop ratios of protein to reservoir solutions from Hampton Research crystal screens (Cat. No. HR2-130, HR2-139, HR2-134) or Microlytic Crystallization Screens (Cat. No. MCSG-1, MCSG-2, MCSG-3, MGSG-4). Trays were sealed and incubated at 4°C or 20°C, then monitored over several months for crystal growth using a Formulatrix Rock Imager. Several of the successful crystallization solutions were optimized to generate additional crystals amenable in size (>30 micron) and shape (3-dimensional) for data collection. Protein and precipitant concentrations were adjusted to promote fewer nucleation events in the drops, leading to the formation of fewer larger crystals as opposed to numerous smaller crystals. Further optimization trials involved altering the pH, incubation temperature, precipitant type and concentration, buffers, additives (i.e. salts, amino acids, reducing agents), and the physical method of setting up the crystal drop. A total of 137 3-dimensional (3D) crystals were treated with a cryoprotectant solution (containing the crystallization solution along with 10% glycerol or ethylene glycol) and frozen in liquid nitrogen. Crystals were tested for diffraction

remotely at the Stanford Synchrotron Radiation Lightsource (SSRL) or the Advanced Light Source (ALS) at Berkeley.

2.2.4. Negative staining of actomyosin

To determine if the S532P mutation disrupts interactions important for strong binding to actin, we sought to examine the actomyosin complex under rigor conditions (without ATP). In preparation for negative staining, over 80 experimental trials were performed to optimize complex formation and sample staining. A variety of parameters were adjusted, including protein sample preparation, protein concentrations and ratios, pH buffer, salt concentration, staining conditions, and the physical methods of sample attachment to TEM grids.

The following procedure was used ultimately for sample preparation and data collection: F-actin (30 μM) was polymerized from frozen G-actin stocks by adding one volume of 10x actin polymerization buffer (50 mM Tris-Cl, pH 8, 0.5 M KCl, 20 mM $MgCl_2$, 10 mM ATP) to nine volumes of G-actin. To remove ATP and soluble G-actin, a total of 25 μL of 30 μM F-actin was centrifuged (Beckman TLA-100 rotor, 78,000 RPM, 12 minutes, 4°C), and the pellet was resuspended in 24 μL of a low salt experimental buffer (75 mM KCl, 5 mM HEPES, 1 mM $MgCl_2$, 10 mM DTT, pH 7.0). To catalyze the hydrolysis of residual ATP, a total of 1 μL of apyrase (New England Biolabs, 500 U/mL) was added for a final concentration of 20 U/mL. F-actin was incubated at 30°C for 5 minutes, then placed on ice. S1 was diluted to 8 μM for control S1 or 10 μM for S532P S1 in the 75 mM KCl buffer. Lower concentrations of control S1 relative to S532P S1 were used for complex formation to reduce the over-decoration and extreme bundling of decorated filaments observed in control samples. Re-purified F-actin and S1 were mixed in the 75 mM KCl buffer at a final concentration of 3 μM F-actin and 1.9 μM control S1 or 2.4 μM S532P S1. A salt concentration of 75 mM KCl was chosen for complex formation, since lower salt concentrations had a detrimental effect on S1 solubility, while high salt concentrations disrupted complex formation. HEPES was chosen as a pH buffer, since it

was observed to be less reactive than phosphate buffer or MOPS in precipitating the uranyl acetate (UA) staining reagent. Samples were incubated on ice for 10 minutes and centrifuged (Beckman TLA-100 rotor, 78,000 RPM, 12 minutes, 4°C). Pellets were resuspended in 2.5 µL of a 10 mM KCl buffer (10 mM KCl, 5 mM HEPES, 1 mM $MgCl_2$, 10 mM DTT, pH 7.0). The entire 2.5 µL sample was attached to a carbon-coated, plasma treated grid for 1 minute. Excess sample was blotted, and a thin layer of sample was left on the grid. For negative staining, the grid was stained with 10 µL 2% UA for 1 minute, washed in 30 µL HPLC H_2O, and immediately blotted to dry. For cryopreserved samples, unstained samples were attached to a Quantifoil® Holey Carbon Film grid, and excess sample was blotted. Grids were plunged in liquid ethane and then stored in liquid nitrogen for future use. Cryopreserved samples were imaged on a Titan Krios microscope (FEI) equipped with a Falcon II direct electron detector, and a Tecnai TEM equipped with a 4k x 4k pixel CCD camera (SBP MDI). Negatively stained samples were imaged using a 120 kV Tecnai 12 TEM equipped with a CCD camera (SDSU), which confirmed the successful formation of S1-bound decorated actin filaments. For structural determination of negatively stained samples, images were recaptured on Kodak film using a 120 kV Tecnai 12 TEM (Sanford Burnham Prebys MDI), at a magnification of 52,000, and defocus of 1.5 µm. Film negatives were scanned using a Photoscan scanner (Zeiss-Intergraph). A total of >2,900 particles were selected from negatives using Boxer from the Eman software package.[48] Individual 2D particle images were grouped into 69 2D class averages using the Sphire cryo-EM software suite.[49]

2.3. Results

2.3.1. Purification of bulk myosin S1

Flies expressing His-tagged mutant or wild-type myosin were homogenized, and the soluble portion of the homogenate was clarified via a series of centrifugation steps. Full-length myosin was extracted in a 500 mM NaCl solution (Fig. 2.3: Lane 2). Following Ni column

chromatography, the eluted fractions contained His-tagged myosin along with a 70 kD non-specific binding protein “NS” (Fig. 2.3: Lane 6). Purified myosin was precipitated in a 94 mM NaCl solution, and the insoluble fraction was resuspended in digestion buffer (Fig. 2.3: Lanes 7-9). Full length myosin was subjected to proteolysis by chymotrypsin to produce the S1 and rod fragments (Fig. 2.3: Lanes 10-12). S1 was further purified using size-exclusion chromatography (Fig. 2.3: Lane 14). Overall, our expression and purification system produced highly concentrated S1 (approximately 1 mg at 2-6 mg/mL) suitable for structural determination.

2.3.2. X-ray crystallography trials

Commercially available broad-based screens were employed to determine conditions that produce S1 protein crystals. Numerous conditions were attempted, including broad screening with different nucleotides (ADP, AMP-PNP, apo) and optimization based on previous hits. Several of the initial crystallization hits produced crystals unsuitable for data collection, generally due to their 2-dimensional (2D) shape or small size. Thus, the solutions that produced these crystals were optimized to generate additional crystals amenable for data collection. A total of 137 3-dimensional (3D) crystals were tested for diffraction remotely at the Stanford Synchrotron Radiation Lightsource (SSRL) and the Advanced Light Source (ALS) at Berkeley. Several crystals containing S532P S1 yielded diffraction (maximum resolution of 6.4 Å) (Table 2.1 and Fig. 2.4: A-B).

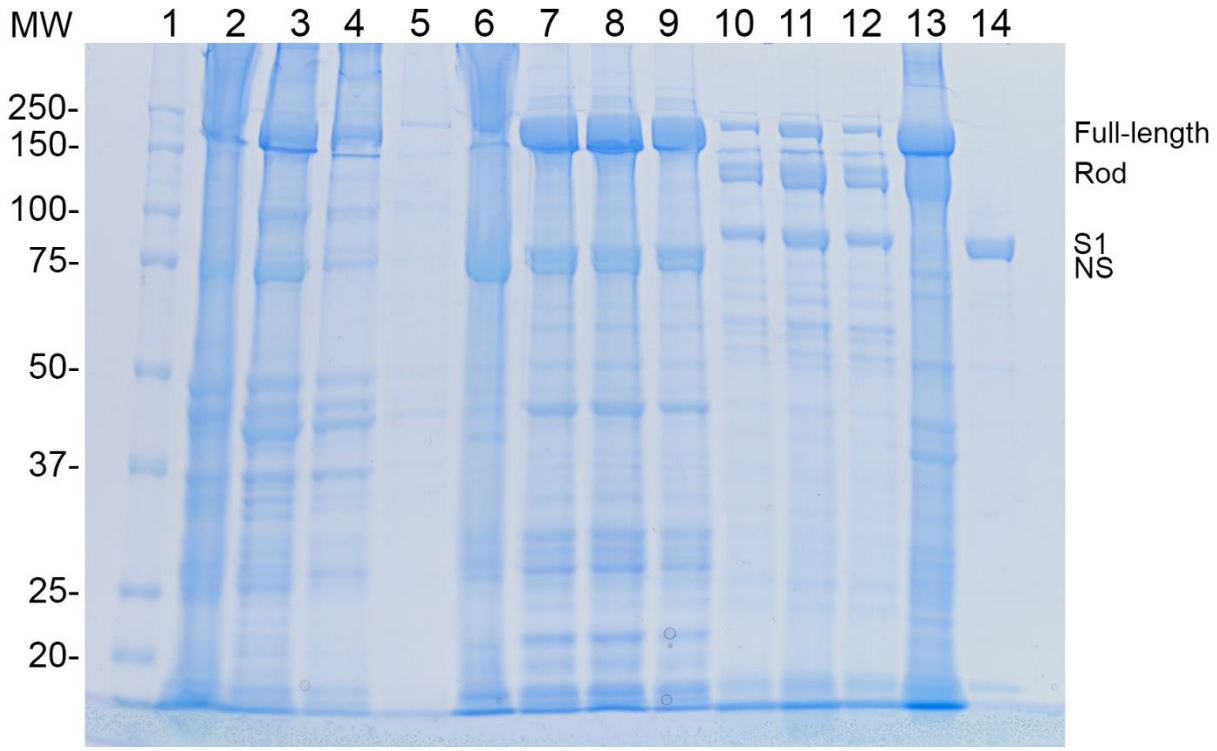

Figure 2.3- Bulk purification of myosin S1 from homogenized His-tagged flies
Protein samples were resolved using 10% SDS-PAGE. Sample lanes: 1) Bio-Rad Precision Plus ladder Cat #161-0375, 2) High-salt extraction after sonication contains full-length myosin, 3) High-salt extraction buffer after removal of exoskeleton and cellular debris contains full-length myosin, 4) Ni column flow-through, 5) Ni column wash, 6) Ni column eluate contains full-length myosin and non-specific Ni-binding protein (NS), 7-9) Low-salt precipitate containing myosin solubilized in digestion buffer, 10-12) Post-proteolysis containing rod, S1 and uncut myosin, 13) Insoluble fraction containing rod and uncut myosin, 14) Purified concentrated S1.

Table 2.1- X-ray diffraction of S532P S1 crystals
A total of 137 protein crystals containing S532P S1 were remotely tested for diffraction at the Stanford Synchrotron Radiation Lightsource (SSRL) at Stanford and the Advanced Light Source (ALS) at Berkeley. The crystallization solutions and protein concentrations that yielded diffraction-quality crystals are shown. Corresponding cryoprotectant solutions and resolutions of diffraction are listed. For all conditions, S532P S1 was mixed with 2 mM AMP-PNP or 2 mM ADP and 2 mM $MgCl_2$ in a sitting well plate using a drop volume of 200 nL and a drop ratio of 1:1 (protein : crystallization solution), and incubated at 20°C.

Crystallization solution	Protein concentration	Cryoprotectant solution	Nucleotide	Resolution of diffraction
Hampton Research Peg Ion, well D4 (0.2 M sodium phosphate dibasic dihydrate, 20% w/v polyethylene glycol 3,350)	5 mg/mL	0.2 M sodium phosphate dibasic dihydrate, 20% w/v polyethylene glycol 3,350, 10% ethylene glycol	ADP	6.4 Å
Hampton Research Index, well G9 (0.2 M ammonium acetate, 0.1 M tris pH 8.5, 25% polyethylene glycol 3,350)	6 mg/mL	0.2 M ammonium acetate, 0.1 M tris pH 8.5, 25% polyethylene glycol 3,350, 10% ethylene glycol	ADP	7.5 Å
Hampton Research Peg Ion, well F10 (0.2 M ammonium citrate tribasic, pH 7.0, 20% w/v polyethylene glycol 3,350)	6 mg/mL	0.16 M ammonium citrate tribasic, pH 7.0, 16% w/v polyethylene glycol 3,350, 10% ethylene glycol	ADP	8.0 Å
Hampton Research Index, well H8 (0.1M magnesium formate dihydrate, 15% w/v polyethylene glycol 3,350) x 3 crystals tested	3 mg/mL	0.1M magnesium formate dihydrate, 20% w/v polyethylene glycol 3,350, 10% ethylene glycol	AMP-PNP	16-20 Å

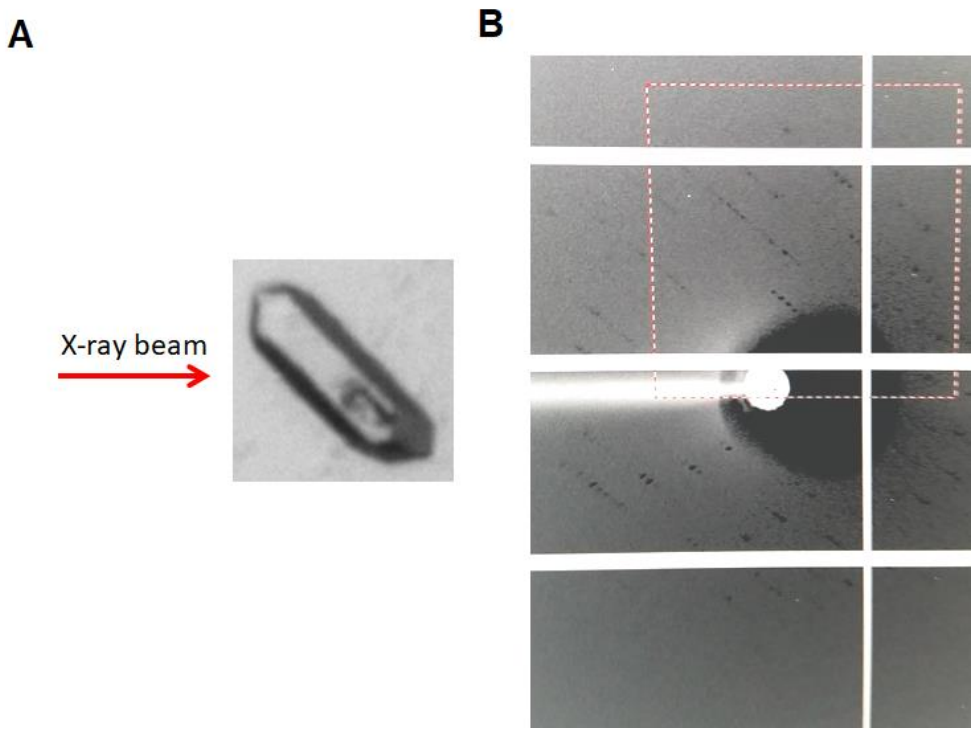

Figure 2.4- X-ray diffraction of a 3-dimensional crystal containing S532P S1
A) A 75 µm crystal was obtained using the following crystallization solution: Hampton Research Peg Ion, well D4 (0.2 M sodium phosphate dibasic dihydrate, 20% w/v polyethylene glycol 3,350) mixed with 5 mg/mL S1, 2 mM ADP, and 2 mM $MgCl_2$ in a sitting well plate using a drop volume of 200 nL and a drop ratio of 1:1 (protein : crystallization solution). **B)** Diffraction of 6.4 Å was observed remotely at the Advanced Light Source (ALS) at Berkeley.

2.3.3. Transmission electron microscopy of S532P actomyosin

Due to limited success in obtaining crystals adequate for structural determination, we initiated a collaboration with Drs. Dorit Hanein and Niels Volkmann (Sanford Burnham Prebys Medical Research Institute) to study the structural basis of S532P dysfunction using transmission electron microscopy (TEM). We successfully formed protein complexes containing wild-type or S532P S1-decorated F-actin, and assessed complex formation using negative staining (NS) and TEM (Fig. 2.5). The binding of S1 to F-actin is unidirectional due to the polarity of the actin filaments, which produces a characteristic arrowhead pattern. Each side of the arrowhead is composed of an individual S1 monomer. Overall, our methods produce grids suitable for structural determination in areas where bound S1 monomers can be clearly resolved (Fig. 2.5). However, the majority of grid surfaces contain areas inadequate for data collection. Decorated filaments were frequently observed in bundles (Fig. 2.6A and 2.6F). The degree of decoration was also variable, with some filaments over-decorated and some under-decorated (Fig. 2.6A). The staining patterns were inconsistent throughout the grids, with some areas overstained (Fig. 2.6B and 2.6E) and some areas understained (Fig. 2.6C). Additionally, the mixture of excess sample buffer with the UA stain formed crystalline deposits on the grid (Fig. 2.6D-E). Thus, a blotting step was performed to remove excess buffer from the grid prior to staining. This step was performed with caution, leaving a thin wet layer of sample on the grid to prevent it from drying out.

As a preliminary structural assessment, we compared the actomyosin structures of samples containing S532P or control S1. Fig. 2.7A is a schematic representation of the structural changes associated with the transition from weak to strong actomyosin binding. In the rigor conformation, the myosin lever arm is rotated to a position closer to the actin filament (Fig. 2.7A: red).[50] Given that the protein complex was formed under rigor conditions in the absence of nucleotide, the myosin heads were expected to adopt the rigor conformation in control samples.

The structures of control (Fig. 2.7B: blue) and S532P (Fig. 2.7B: red) actomyosin were superimposed for comparison. For control S1 bound to F-actin, the myosin lever arm appears to adopt a rigor position more closely aligned with F-actin. The lever arm sticks out further in the S532P mutant relative to the actin filament, resembling a weak actin binding state. Overall, the S532P mutation appears to disrupt the transition from weak to strong actin binding. However, it is possible that effects of the angular orientation of the particles contribute to the differences observed in the mutant structure.

We are currently performing cryo-EM with single particle analysis to solve the mutant and control structures in a quantitative manner that incorporates images of the particles from various angular orientations. For this, we sought to solve low-resolution structures obtained from negatively stained samples as initial models for cryo-electron microscopy structural determination. Images from negatively stained samples of control or mutant myosin bound to F-actin were captured on film and digitized with a high-resolution scanner. Thousands of single bound S1 monomers were manually selected using the Boxer of Eman software package[48] to generate input images for software reconstruction. Each input image is a 2D rotational view of the 3D structure. Individual 2D images were grouped into 69 2D class averages for S532P S1 bound to F-actin (Fig. 2.8A) using the Sphire cryo-EM software suite.[49] Eventually, we will employ the Relion software package[51] to perform a 2D Fourier transform of the 2D classes and generate a 3D model in Fourier space. A Fourier inversion will subsequently be performed by the software to obtain a 3D low-resolution map of the structure. Recently, we collected ~4000 images of cryopreserved S532P S1-decorated F-actin for high-resolution structural determination. A representative micrograph is shown in Fig. 2.8B. Though some decorated filaments appear bundled (arrows) or underdecorated (asterisk), single bound particles can be resolved in a majority of grid surfaces. Overall, we expect these efforts to produce high-resolution cryo-EM structures.

Figure 2.5- Transmission electron microscopy micrograph of negatively stained myosin S1-decorated F-actin
Scale bar, 100 nm.

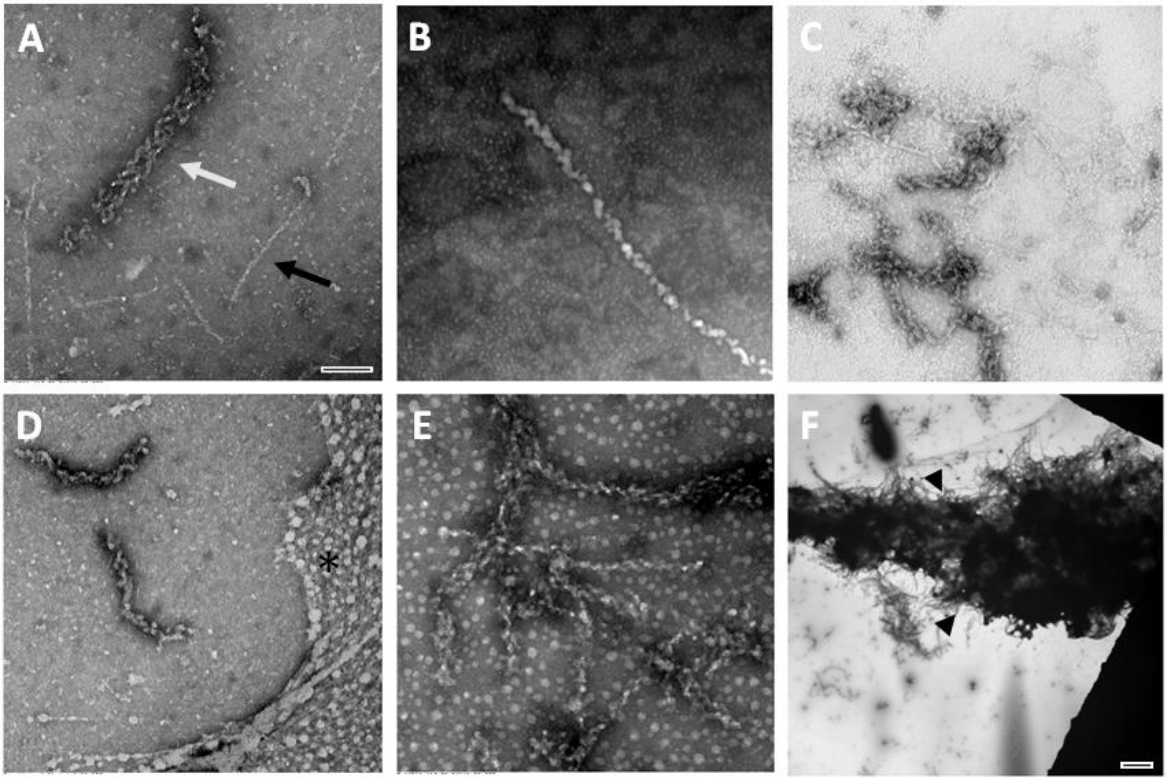

Figure 2.6- Transmission electron microscopy micrographs showing representative images of negatively stained actomyosin grids

Various challenges were encountered during sample preparation and data collection: **A)** Bundling and overdecoration of filaments (white arrow) as well as undecorated filaments (black arrow), **B)** Overstained background, **C)** Understained background, **D)** Thick layer of uranyl acetate crystalline deposit (asterisk), **E)** Uranyl layer crystalline deposit and heavy background staining, and **F)** Excessive bundling of decorated filaments (arrowheads). Scale bars, 0.1 µm for panels A-E, 2 µm for panel F.

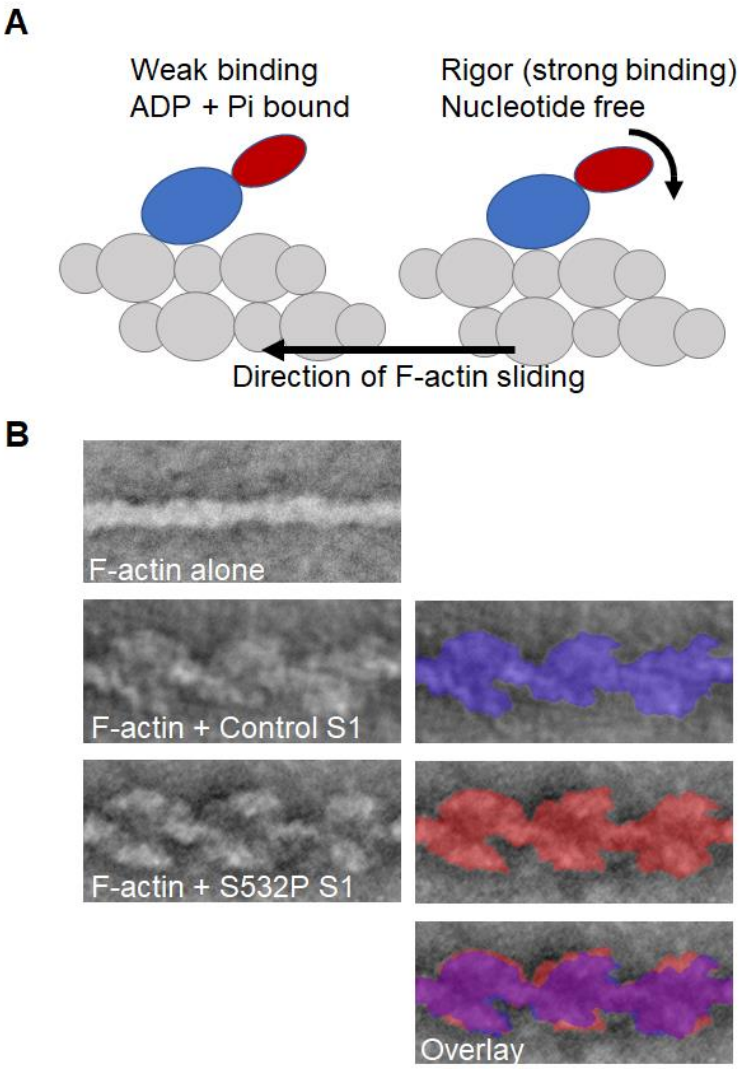

Figure 2.7- Preliminary structural analysis of negatively stained S532P S1-decorated F-actin

A) Schematic representation of the transition of weak to strong actomyosin binding. Left- The myosin motor domain (blue) is weakly bound to F-actin (grey) in a non-force generating state with ADP and inorganic phosphate (P_i) attached. Right- Following the release of P_i and ADP, the motor domain (blue) is strongly bound to F-actin (grey) in the rigor conformation. In this conformation, the lever arm (red), which extends to the myosin neck region, is rotated to a position closer to the actin filament. **B)** TEM micrographs of negatively stained S532P and control myosin S1 bound to F-actin. Actomyosin structures were digitally colorized and overlaid for comparison. F-actin imaged in the absence of S1 is shown as a control.

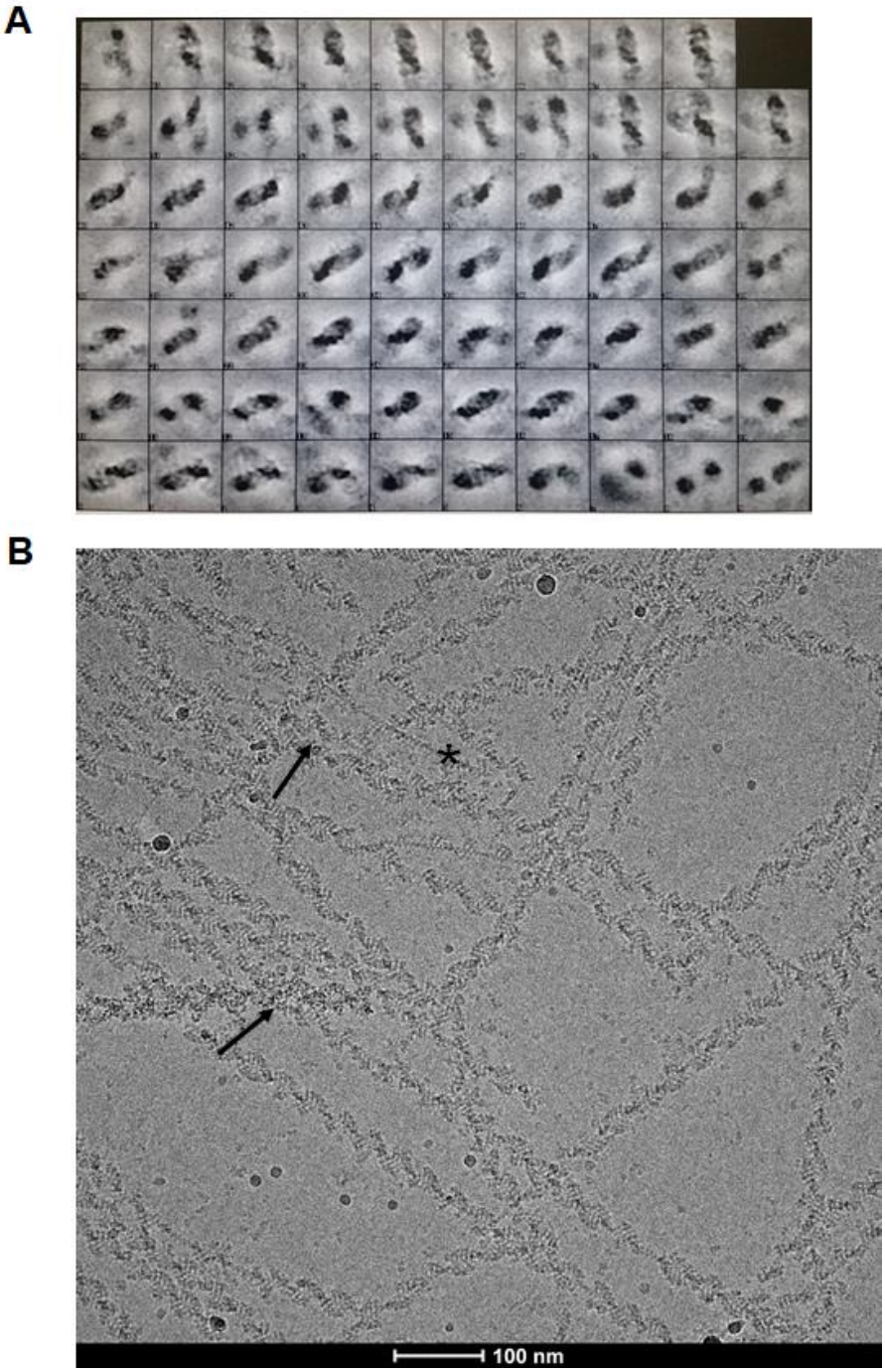

Figure 2.8- Structure determination of S532P S1 bound to F-actin
A) TEM samples of negatively stained S532P or control S1 bound to F-actin were used for initial structural modeling. Images were captured on film and digitized. Single bound particles were manually selected and subjected to 2D class averaging using Sphire.[49] Images of the 69 2D-class averages obtained for S532P S1 bound to F-actin are shown. **B)** A representative TEM micrograph of a cryopreserved sample of S532P myosin S1 bound to F-actin. Arrows- Bundled decorated filaments. Asterisk- Undecorated filament.

2.4. Discussion

We performed X-ray crystallography and cryo-electron microscopy (cryo-EM) experiments to probe the structural effects of the S532P myosin dilated cardiomyopathy (DCM) mutation, which is located in an α-helix within an actin-binding helix-loop-helix motif of the L50 subdomain.[30] We hypothesized that a proline substitution at the S532 residue disrupts intramolecular interactions at the L50 subdomain that are important for actin binding, rendering the S532P myosin form underfunctional at the biochemical and whole tissue levels. This is in concordance with the results reported in chapters 3 and 4, where we found that the S532P mutation impairs actomyosin interactions and reduces actin-stimulated ATPase activity, resulting in reduced skeletal muscle function and cardiac dilation.

To understand the potential function of the mutant S532 residue, it is important to focus on the known role of the L50 subdomain in which it is located and its interaction with actin. During the myosin ATPase cycle, actin binding promotes the release of the products of ATP hydrolysis, which is coupled to the lever arm movements referred to as the powerstroke steps.[7,52,53] Previous cryo-EM reports suggest that the L50 subdomain is involved in the initial weak binding to actin. Structural assessment of the state in which myosin-ADP-P_i is weakly bound to actin is challenging due to its instability and short lifetime.[50] Thus, Fujii et al.[50] compared the cryo-EM structure of mammalian skeletal muscle myosin S1 bound to F-actin in rigor with the crystal structure of skeletal muscle myosin II in post-rigor.[25] In the post-rigor state, myosin is weakly bound to actin when actin is present. The helix-loop-helix structural element of L50 subdomain forms hydrophobic interactions with two adjacent actin subunits in post-rigor. Loop 2, located between the U50 and L50 subdomains, forms electrostatic interactions with actin during the weakly bound ADP+P_i state, and is predicted to act as a tether to allow a rotation of the U50 subdomain during the transition from the weak to strong actin binding states. The crystal structure of chicken skeletal muscle myosin S1 in post-rigor[25] was incorporated into

the cryo-EM structure of S1-decorated F-actin in rigor by Holmes et al.[52] The L50 subdomain interacts with F-actin when myosin is weakly bound to actin. In that state, the binding cleft is open.

In contrast to the L50 subdomain, the U50 subdomain does not interact with actin during initial weak actin binding. Following the rotation of the U50 subdomain, additional contacts are formed between the U50 subdomain and actin to stabilize the rigor conformation. Behrmann et al. compared the cryo-EM structure of actin-tropomyosin-myosin in rigor with the X-ray crystal structure of myoE with ADP-VO4 bound in the pre-powerstroke state[54] and revealed that the L50 subdomain shows little structural difference between weakly-bound and strongly-bound states.[55] The authors suppose that that myosin initially binds actin at the L50 subdomain, and that its contacts with actin are mainly hydrophobic in nature. Since proline is characterized as a potent α-helix breaking residue[56], we predict that the S532P mutation interrupts hydrophobic interactions between the helix-loop-helix motif and actin, which may destabilize the weakly bound ADP+P_i state.

The cryo-EM structures of actomyosin in rigor reported by Holmes et al.[52], Behrmann et al.[55], and Fujii et al.[50] suggest that the U50 rotates 15-20 degrees clockwise in response to weak actin binding to form additional contacts between the U50 and actin, which closes the actin binding cleft and stabilizes the rigor conformation. These contacts are mainly electrostatic in nature, and include the binding of the loop 4, the CM loop, and helix W of myosin to the SD1 and SD3 subunits of one of the actin monomers.[55] Loop 3 is bound to the SD1 of the next lower pitch helix actin.[55] The hydrophobic interactions between the helix-loop-helix motif of L50 and actin are thought to serve as a hinge for rotation.[52] Overall, these data suggest that the L50 subdomain plays a role in the structural transition from the weakly bound state to rigor by stabilizing interactions with actin to close the binding cleft. Since the S532P mutation is located within the helix-loop-helix motif, we predict that it destabilizes interactions that are important for the transition to the rigor state.

In order to understand how structural changes at the actin binding subdomain induced by the S532P mutation reduce myosin function, the communication pathway from the L50 subdomain to the nucleotide binding pocket must be taken into consideration. The enhancement of ATPase activity in response to actin binding has been documented in biochemical and kinetics studies.[7,57,58] Conformational changes at the actomyosin interface are communicated to the nucleotide binding pocket via the transducer subdomain, which includes the last 4 strands of a central β-sheet and associated surface loops.[59] In response to actin binding, the central β-sheet becomes distorted.[52,55,60] This results in compression of the N-terminal subdomain, which is relaxed upon dissociation of P_i.[55] In the rigor structures, closure of the binding cleft is associated with the opening of the nucleotide binding pocket, suggesting that actin binding promotes the release of the products of ATP hydrolysis (P_i and ADP).[50,52,55] The X-ray crystal structure of chicken skeletal muscle myosin S1 showed that the nucleotide binding pocket contains a P-loop with switch 1 and switch 2 elements that gate ATP and the products of hydrolysis.[25] During the transition from weak binding to rigor, movement of switch 1 and switch 2 into an open position promotes the release of P_i and ADP from the nucleotide binding pocket.[50,52,55] Subsequent rotation of the N-terminal and converter subdomains are coupled to the lever arm swing which is the powerstroke that yields force generation.

Our results suggest that the communication pathway that enhances ATPase activity in response to actin binding is disrupted by the S532P myosin mutation. In chapter 3, we report that actin-stimulated Mg-ATPase activity is reduced in S532P myosin compared to controls, while basal Mg-ATPase activity (enzymatic activity in the absence of actin) is unaffected by the mutation. Moreover, muscle mechanics of isolated indirect flight muscles and skeletal muscle functional tests revealed diminished contractile performance, suggesting that the S532P myosin form is under-functional. Our structural work explores whether reductions in actin-activated ATPase activity and contractile function of S532P myosin are linked to impaired actomyosin interactions.

Successful structural studies using crystallization screening and cryo-EM experiments are dependent upon milligram quantities of protein, which is difficult to obtain by primary dissection. To obviate this difficulty, we developed His-tagged lines expressing the S532P DCM myosin mutation in IFMs and obtained bulk quantities of protein from homogenized flash-frozen whole flies. Following Ni column chromatography, full length myosin was subjected to proteolysis by chymotrypsin, and the subfragment-1 (S1) was purified using size exclusion chromatography.[19] This yielded approximately 1 mg of purified S1 per preparation, making Drosophila a good source of purified myosin for structural analyses.

Protein molecules must arrange in a highly ordered array to produce a diffraction quality crystal.[34] The resolution of diffraction from S532P S1 crystals was not adequate for structure determination. Thus, it is possible that the mutation affects the ordered packing of protein molecules by disrupting intramolecular interactions within the helix-loop-helix motif of the actin binding cleft. As an alternative approach for solving the mutant structure, we performed cryo-EM of S532P S1 bound to F-actin. The cryo-EM approach is advantageous, since the structure of mutant S1 can be assessed in the presence of F-actin to determine intermolecular interactions disrupted by the mutation.

We formed the complex of S532P S1 bound to F-actin under rigor conditions (in the absence of ATP) to determine if the S532P mutation disrupts actomyosin interactions. Transmission electron microscopy (TEM) micrographs of negatively stained S1-decorated F-actin revealed that the position of the lever arm of the mutant more closely resembles the state in which myosin-ADP-P_i is weakly bound to actin. In contrast, the lever arm of the control structure appears to adopt the rigor conformation. Thus, it is possible that the S532P mutation disrupts the transition from weak to strong actin binding. However, the data must be interpreted with caution, since the differences observed may result from the effects of the angular orientation of the particles. Future approaches will combine cryo-EM and single particle analyses to produce 3-dimensional (3D) structural data. For this, we successfully obtained high-

resolution data of cryo-preserved S532P S1 bound to F-actin. Images of single bound particles will be selected to generate 2-dimensional (2D) class averages representing different angular orientations of the sample using specialized software. Fourier transforms of 2D class averages will be fit with preliminary structural information to generate a model in 3D Fourier space. Finally, a mathematical Fourier inversion will be performed by the software to obtain a 3D map of the structure. We anticipate that these efforts will produce a high-resolution structure and yield a better understanding of the structural basis of myosin-induced DCM.

Chapter 2, in full, contains unpublished material coauthored by Trujillo, Adriana S.; Volkmann, Niels; Hanein, Dorit; Bernstein, Sanford I. The dissertation author was the primary investigator and author of this chapter.

Chapter 3: Determine whether the myosin DCM mutation S532P causes deficits in myosin enzymatic activity and functional output of fibers

3.1. Introduction

3.1.1. Drosophila indirect flight muscle system

We exploited the Drosophila indirect flight muscle (IFM) system to determine the mechanistic basis of contractile dysfunction induced by the dilated cardiomyopathy (DCM) myosin S532P mutation. Drosophila IFMs constitute the bulk of the thorax and are readily accessible via microdissection. Thus, myosin can be purified from isolated IFMs in sufficient quantities for biochemical assays, making them an excellent system to determine the molecular basis of myosin-induced DCM. Additionally, IFM ultrastructure is highly organized, similarly to human skeletal muscles, and our lab has observed severe ultrastructural defects in IFMs of flies expressing myosin mutations associated with skeletal muscle myopathies[61-63] and cardiomyopathy[12,13,64] in humans. Furthermore, functional tests are relatively straightforward in IFMs compared to other muscles. Flight testing is a simple and low cost strategy to determine muscle function.[65] Muscle mechanics analyses on isolated skinned fibers can be used to determine mechanical properties and cross-bridge rate constants of IFMs in the context of an intact myofilament lattice.[66]

3.1.2. Biochemical defects associated with the S532P mutation

Some previous reports suggest that the S532P mutation reduces myosin function and muscle functional output. A mouse model expressing the S532P mutation in α-cardiac MHC caused a DCM phenotype in which reduced cardiac contractility was associated with decreases in actin-activated ATPase activity, reduced ability of myosin to translocate F-actin *in vitro,* reduced myosin step size, and altered kinetics.[30] However, in skinned ventricular muscles, *S532P/+* fibers exhibited a higher rate of force development at saturating Mg-ATP and higher Mg-ATP binding rates[67], which was not consistent with molecular-level studies using isolated myosin.[30] Palmer et al. hypothesized that a higher Mg-ATP binding rate may result in a

shortened myosin crossbridge lifetime.[67] Recent kinetic analyses using recombinant mutant human β-cardiac myosin showed that myosin S532P exhibits a reduction in duty ratio (the fraction of the ATPase cycle where myosin is bound to actin), due to a reduced occupancy of the force holding ADP-bound actomyosin state (A-M-ADP).[8] Ujfalusi et al. noted that these altered kinetic properties are predicted to reduce contractile function by lowering the load-bearing capacity of the mutant forms (i.e. more cross-bridges need to be active to sustain load relative to wild-type).

3.1.3. Hypothesis and goals

The goal of this aim was to determine the molecular and cell biological defects induced by the DCM myosin S532P mutation in the Drosophila model. We exploited the IFM system to test the hypothesis that a DCM myosin mutation localized to an actin binding site will weaken actin affinity, reduce enzymatic activity of myosin, and cause structural and functional defects in muscles.

3.2. Materials and methods

3.2.1. Actin co-sedimentation

The binding affinity of S1 to F-actin was determined by actin co-sedimentation as described previously[68,69], with slight modifications. F-actin was polymerized from frozen chicken G-actin stocks and stabilized with a 1:1 molar ratio of phalloidin. S1 was purified using the bulk His-tagged myosin purification procedure described in Section 2.2.2. Protein purification. Subsequently, S1 was centrifuged (Beckman TLA-100.3 rotor, 70,000 RPM, 60 minutes, 4°C) to remove insoluble aggregates. The protein concentration in the soluble portion was determined by spectrophotometry, and it was diluted to 25 μM. S1 (1.5 μM) was incubated with increasing concentrations of phalloidin-stabilized F-actin (0, 0.4, 0.6. 0.8, 1, 1.2, 1.4, 1.6, 1.8, 2, 3, and 4 μM) in a low salt buffer (100 mM NaCl, 200 mM sodium phosphate, 5 mM $MgCl_2$, 4 mM DTT,

pH 7.0) in a total volume of 25 µL. Samples were incubated for 15 minutes on ice and centrifuged (Beckman TLA-100.3 rotor, 70,000 RPM, 60 minutes, 4°C). Soluble fractions were separated from pellet fractions, and pellets were resuspended in 25 µL of the low salt buffer. Samples were applied to a 10% SDS-polyacrylamide gel. Gels were stained with the GelCode® Blue Stain Reagent, destained, scanned on an Epson Perfection 1640SU scanner using VueScan software (Hamrick), and analyzed using the Un-Scan-It (Silk Scientific) software package as reported previously.[70] To calculate the bound fraction in actomyosin pellet samples, the density of S1 in the pellet fraction relative to total protein content was determined, and the fraction of pelleted S1 in S1-only controls was subtracted from this value. Bound fractions were plotted over increasing F-actin concentrations, and fit to a hyperbolic function, were K_d was defined as the F-actin concentration required to reach half maximal binding (B_{max}).

3.2.2. Generation of mutant (non His-tagged) genomic DNA lines

We generated transgenic flies expressing the S532P myosin mutation in the germline. Transgenic myosin without the His-tag was expressed to avoid potential detrimental effects due to disruption of a few N-terminal amino acid residues added during the His-tag cloning procedure.[19] Transgenic lines were crossed into the *Mhc*^{10} background that is null for endogenous myosin in indirect fight muscles (IFMs) and jump muscles.[45] Myosin was purified from microdissected IFMs from homozygous individuals for biochemical assays. Skinned fiber mechanics were performed to determine whether this mutation alters IFM fiber force output and cross-bridge rate constants (collaboration with Dr. Douglas Swank, Rensselaer PI). We also performed functional analyses of IFMs and jump muscles in intact organisms, as well as ultrastructural analyses of IFMs to determine whether biochemical changes lead to tissue-level defects in our fly model.

The cloning strategy for the S532P construct is shown in Fig. 3.1.

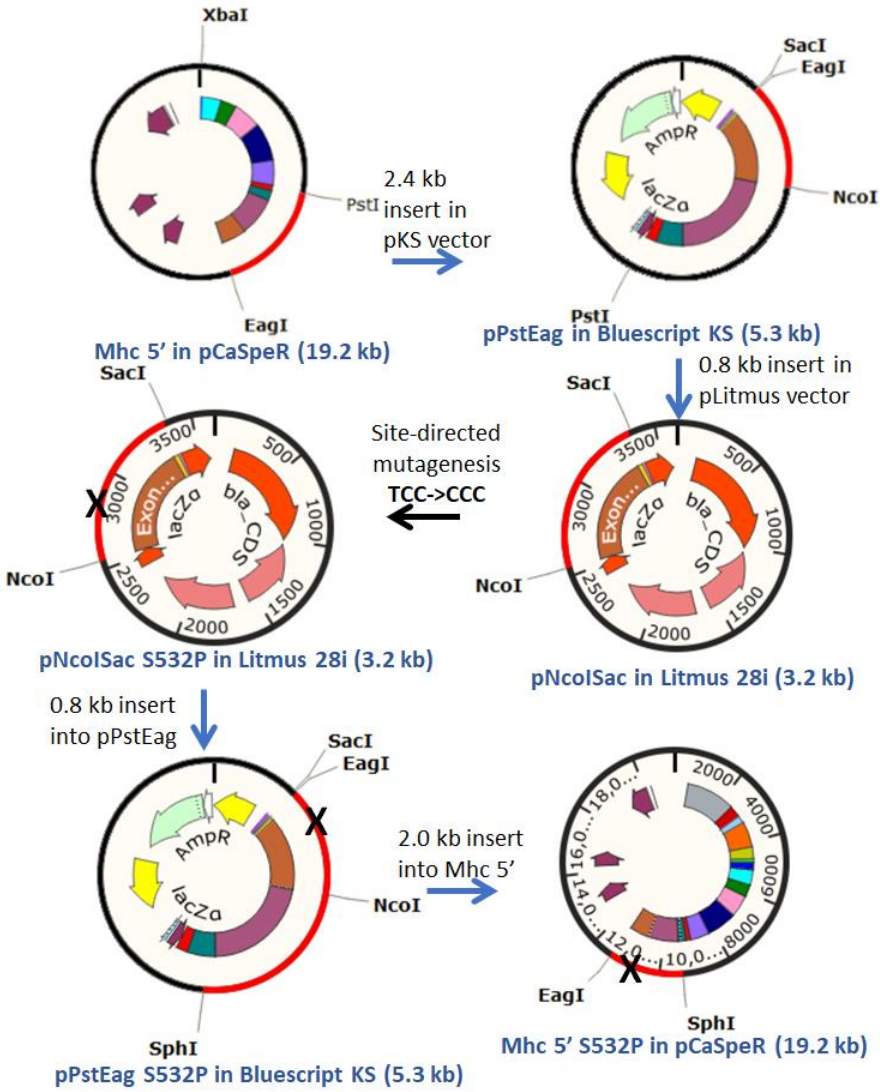

Figure 3.1- Cloning scheme for the Mhc S532P construct, Part I
The sequential steps of restriction enzyme (RE) digestion and ligation are shown by the blue arrows. Each insert generated by RE digestion of the parent vector is shown in red, along with RE cut sites. Site-directed mutagenesis (black arrow) was performed to change the serine codon to a proline codon at the 531st amino acid coding position of Drosophila *Mhc* (corresponding to position 532 in human *MYH7*).

Subclones containing *Mhc* exon 10 were generated from a larger plasmid containing a 19.2 kb *Mhc* 5' fragment. Oligonucleotide-directed mutagenesis was performed (QuikChange kit, Stratagene) to change the codon in Drosophila *Mhc* that corresponds to the *MYH7 S532P* nucleotide transition. The following forward (+) and the reverse (-) primers were used for mutagenesis:

S532P (+): 5'-CCCATGGGTATCTTGCCCATCCTGGAGGAAG-3'

S532P (-): 5'-CTTCCTCCAGGATGGGCAAGATACCCATGGG-3'

The mutated exon was sequenced for confirmation and subclones containing the mutant fragment were inserted into larger cloning intermediates to produce the mutant 5' *Mhc* fragment. For the final cloning step, a 19.2 kb 5' *Mhc* fragment carrying the S532P mutation was removed from its vector by EagI digestion, and ligated to a 3' *Mhc* fragment in a pCaSpeR *P* element vector containing the *miniwhite* (w^+) selectable eye color marker (Fig. 3.2). The final plasmid was purified using the QIAfilter Plasmid Maxi Kit (Qiagen Inc.) and the entire *Mhc* coding region was sequenced for verification by Eton Bioscience.

Embryonic injection was performed by Bestgene, Inc. to incorporate the transgenic insert randomly into the germline via *P* element transformation.[44] A total of 39 transgenic lines were obtained. Several lines mapping to the 3rd chromosome were crossed into the Mhc^{10} myosin null background. Lines that mapped to the second chromosome were not used since it contains the endogenous *Mhc* gene.

Polyacrylamide gel electrophoresis was performed to determine MHC protein levels in these lines, by comparing the ratio of myosin to actin between transgenic flies and *yw* (wild-type) controls, as described previously.[46] Each lysate consisted of six upper thoraces of 0-2 day-old flies. Only lines with wild-type MHC protein levels were chosen for further experiments.

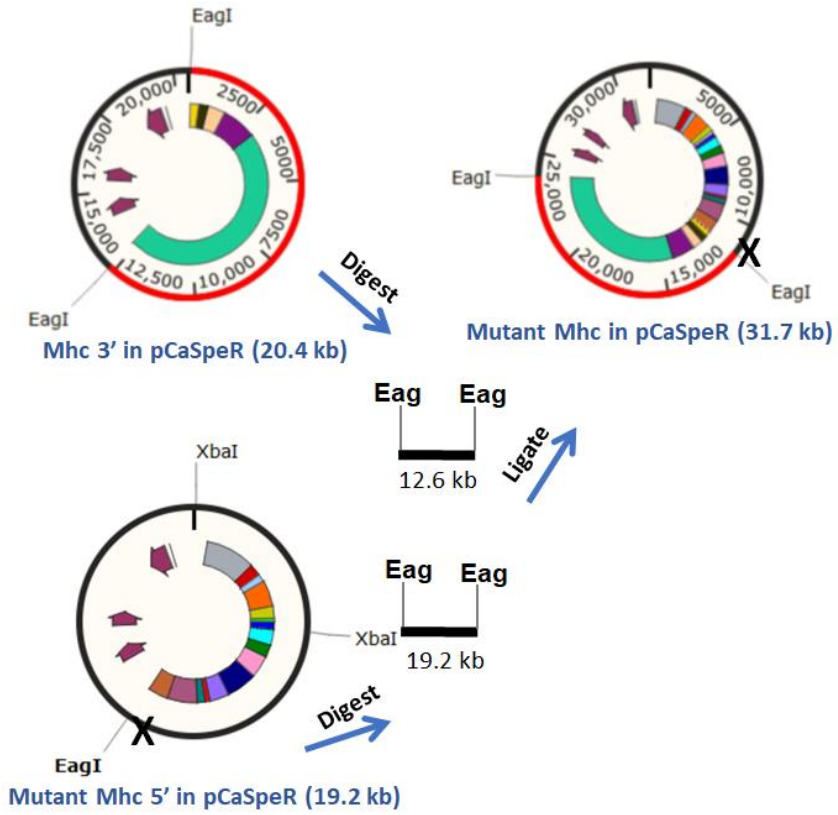

Figure 3.2- Cloning scheme for the Mhc S532P construct, Part II
A 19.2 kb 5' Mhc fragment carrying the S532P mutation was removed from its vector by EagI digestion, and ligated to a Mhc 3' fragment in a pCaSpeR *P* element vector.

RT-PCR confirmed expression of RNA encoding the mutant protein and the absence of endogenous myosin expression in IFMs. Additionally, cDNA was amplified using *Mhc* specific primers to confirm the absence of alternative splicing defects in these lines. RNA isolation, cDNA synthesis, and PCR amplification were performed as described in Section 2.2.1. for the His-tagged line, using the following primer pairs:

Exons 2-8:

(+) 5'-TGGATCCCCGACGAGAAGGA-3'

(-) 5'-GTTCGTCACCCAGGGCCGTA-3'

Exons 8-10:

(+) 5'-CGATACCGCCGAGCTGTACAG-3'

(-) 5'-CAGCTGGTGCATGACCAAGTGGGC-3'

Exons 8-12:

(+) 5'-TCTGGATACCCAGCAGAAGCGT-3'

(-) 5'-GAGCTTCTTGAAGCCCTTACGG-3'

Exon 15:

(+) 5'-CTCAAGCTCACCCAGGAGGCT-3'

(-) 5'-GGGTGACAGACGCTGCTTGGT-3'

For simplicity, lines *S532P-9*, *S532P-23*, and *S532P-34* were respectively renamed as *S532P-L1*, *S532P-L2*. and *S532P-L3*.

3.2.3. Myosin purification and ATPase assay

Myosin purification: Myosin was purified from IFMs as described previously[43] with minor modifications. Dorsal longitudinal IFMs were dissected from 80-120 transgenic flies in 1 mL York Modified Glycerol [YMG: 20 mM potassium phosphate buffer pH 7.0, 1 mM EGTA, 2 mM $MgCl_2$, 50% glycerol, 20 mM DTT, and Roche complete mini protease inhibitor (1 tablet per 10 mL solution)] on ice. The sample was centrifuged at 15,000 x *g*, 5 minutes, 4°C, and the pellet

was resuspended in YMG containing 2% Triton-X. The sample was incubated for 30 minutes on ice to permeabilize cell membranes, then centrifuged at 15,000 x *g*, 5 minutes, 4°C. Triton-X was removed by resuspending the pellet in 1 mL YM buffer (same as YMG but without glycerol). The sample was centrifuged at 15,000 x *g*, 5 minutes, 4°C. The pellet was resuspended in 82.5 µL of myosin extraction buffer (1.0 M KCl, 50 mM potassium phosphate buffer pH 6.8, 10 mM sodium pyrophosphate, 5 mM $MgCl_2$, 0.5 mM EGTA, and 20 mM DTT) for 15 minutes and centrifuged at 15,000 x *g*, 5 minutes, 4°C. The supernatant was removed, and the pellet discarded. Extracted myosin in the soluble portion was precipitated by decreasing [KCl] to 40 mM and incubating for 16 hours at 4°C. The sample was centrifuged (Beckman TLA-100.3, 100,000 x *g*, 20 minutes, 4°C) and the pellet was dissolved in 13.5 µL buffer (2.4 M KCl, 100 mM histidine, 0.5 mM EGTA, 20 mM DTT, pH 6.8). The [KCl] was slowly diluted to 300 mM to precipitate actomyosin, and the sample was centrifuged (Beckman TLA-100.3, 60,000 x *g*, 25 minutes, 4°C). The supernatant was separated, and [KCl] was diluted to 30 mM to precipitate myosin. Following centrifugation (Beckman TLA-100.3, 60,000 x *g*, 25 minutes, 4°C), the pellet was resuspended in 33 µL myosin storage buffer (0.5 M KCl, 20 mM MOPS, pH 7.0, 2 mM $MgCl_2$, and 20 mM DTT) and the purified myosin was diluted to a concentration of 2 mg/mL.

ATPase assay: ATPase activity of full-length myosin was measured using [γ-^{32}P]-ATP as described previously.[43] For Ca-ATPase activity, a total of 2 µg of myosin was incubated in 10 mM imidazole, pH 6.0, 100 mM KCl, 10 mM $CaCl_2$, and 1 mM [γ-^{32}P]-ATP at room temperature for 15 minutes. To determine Mg^{2+} basal and actin-stimulated Mg-ATPase activities, 2 µg of myosin was incubated in 10 mM imidazole, pH 6.0, 20 mM KCl, 0.1 mM $CaCl_2$, 1 mM $MgCl_2$, 1 mM [γ-^{32}P]-ATP in the absence or presence of increasing concentrations of F-actin (0.1-2 µM). Following centrifugation, the organic phase containing [γ-^{32}P]-ATP was extracted by adding aliquots of the soluble portion to 0.5 ml of 5% ammonium molybdate, 2 ml of 1.25 N $HClO_4$, and 2.5 ml of isobutanol-benzene (1:1). A total of 1 mL of the organic phase containing [γ-^{32}P]-ATP was assayed for radioactivity with a scintillation counter. Mg^{2+} basal ATPase activities were

subtracted from actin-activated ATPase values, which were fit with the Michaelis Menten equation to determine actin-stimulated ATPase activity (V_{max}) and actin affinity relative to ATPase (K_m).

3.2.4. Muscle mechanics

Detailed procedures for mechanics experiments are described in Swank et al. [66]

IFM fiber preparation: Dorsal longitudinal IFM fibers were dissected from 3 day-old females in skinning solution (pCa 8.0, 5 mM MgATP, 1 mM free Mg^{2+}, 0.25 mM phosphate, 5 mM EGTA, 20 mM N,N-bis(2-hydroxyethyl)-2-aminoethanesulfonic acid [BES, pH 7.0], 175 mM ionic strength [adjusted with Na methane sulfonate], 1 mM DTT, 50% glycerol and 0.5% Triton X-100). Fiber bundles were demembranated for 1 hour at 6°C, then transferred to storage solution (same as skinning solution but without Triton X-100). Individual fibers were separated from the IFM bundle and split in half longitudinally with tungsten wire probes. Both ends of the fiber were fastened with aluminum foil t-clips. The fiber was transferred to a mechanics rig and submerged in relaxing solution (pCa 8.0, 12 mM MgATP, 30 mM creatine phosphate, 600 U/mL creatine phosphokinase, 1 mM free Mg^{2+}, 5 mM EGTA, 20 mM BES at pH 7.0, 1 mM DTT; 200 mM ionic strength 200 mM [adjusted with sodium methanesulfonate]), where it was hooked onto a force transducer and servo motor.

All measurements were obtained at a temperature of 15°C. The fiber was stretched until slack was removed. The fiber length between the t-clips was measured, and the fiber was stretched by 5% of its initial length. The width and height of the fiber were subsequently measured, and the cross-sectional area was calculated assuming an ellipsoid shape. Passive tension (P_o) was recorded in relaxing solution (pCa 8.0), and a small amplitude, sinusoidal length perturbation was applied at various frequencies of oscillations to measure passive stiffness (see details below). The fiber was activated by partially exchanging the bathing solution with activating buffer (same as relaxing solution, with pCa adjusted to 4.0) to bring the pCa to

5.0. The fiber was stretched in 2% increments (relative to the fiber length between the t-clips) until maximum power was obtained (Fig. 3- eq 5), in order to determine the optimal sarcomere length. Following the power optimization, active tension was recorded (A_o) to derive net tension ($F_o = A_o - P_o$) and sinusoidal analysis was performed at decreasing ATP concentrations.

Sinusoidal analysis and mechanical rate constants: Sinusoidal analysis was performed to determine muscle stiffness and mechanical rate constants of the fibers. The muscle was oscillated with a small amplitude sine wave (0.125% muscle length, peak to peak) at frequencies ranging from 0.5 to 650 Hz. For each frequency, the amplitude and phase differences associated with the sinusoidal tension response were calculated to determine the complex modulus (Fig. 3.3- eq 1 to eq 3). The complex modulus can be further separated into the viscous and elastic moduli. The viscous modulus is the out-of-phase component in the Nyquist plot, and is related to the work and power produced by the fiber (Fig. 3.3- eq 4-5). The elastic modulus represents an in-phase component of the complex modulus and is influenced by the spring-like properties of the molecular machinery. The complex modulus was fit to a 3-term equation (Fig. 3.3- eq 6) to determine exponential rate processes (A, B, and C). This equation was originally determined by Kawai and Brant[71] and has been modified by Swank et al.[72] to better fit the IFM system. Process A is influenced by the viscoelastic properties of the fiber structure, and is not dependent on enzymatic steps of the cross-bridge cycle.[73] Process B reflects a work producing step related to actin binding. Process C reflects a work absorbing step prior to and during detachment from actin. In the Nyquist plot, Processes B and C appear as lower and upper hemispheres, respectively, with associated frequencies b and c. Frequencies b and c were multiplied by 2π to convert from frequency to time (s^{-1}), to determine rate constants associated with work producing ($2\pi b$) and work absorbing ($2\pi c$) steps of the cross-bridge cycle.

(eq 1) $P_k(f) = f/n\int_0^{n/f} P(t,f)\exp(-2\pi ikft)\,dt$, where f is the frequency of oscillation, $P(t,f)$ represents periodic force, and k represents linear and harmonic components

Equation for complex stiffness [$Y(f)$]:

(eq 2) $Y(f) = P_1(f)/L_1(f)$, where $P_1(f)$ and $L_1(f)$ represent periodic force and length changes, respectively

Equation for complex modulus [$Y_M(f)$]:

(eq 3) $Y_M(f) = Y(f) * L_0/A_o$, where L_0 and A_o represent the length and cross-sectional area of the muscle preparation, respectively

Equations for work and power:

(eq 4) $\text{Work} = \pi E_v(\Delta L/L)^2$,

(eq 5) $\text{Power} = \pi E_v(\Delta L/L)^2$,

where E_v is the viscous modulus, and $\Delta L/L$ is the length change relative to the muscle length

The complex modulus is fit to the following equation:

(eq 6) $Y_M(f) = A\,(2\pi\, if/\alpha)k - B\,if/(b + if) + C\,if/(c + if)$,

where f is the oscillation frequency, i is the square root of -1, α is 1 Hz, k refers to a unit-less exponent, and A, B, C reflect exponential rate processes

Figure 3.3- Equations used for muscle mechanics experiments via sinusoidal analysis
Equations (eq 1-eq 6) were developed by Kawai et al.[71] Eq 6 was modified by Swank et al. to better fit the IFM system.[72]

ATP response experiments: To elucidate cross-bridge kinetics related to ATP-induced dissociation of myosin from actin, the concentration of ATP in the fiber bathing solution was varied from 20 mM to 0.5 mM while performing sinusoidal analysis. Values for f_{max} were plotted over changing [ATP], and fit with the Michaelis Menten equation to determine actin-stimulated ATPase activity (V_{max}) and actin affinity relative to ATPase (K_m).

3.2.5. Flight and jump tests

Transgenic mutant and control females were reared at 25°C, acclimated to room temperature for 1 hour, and tested at room temperature. For flight testing, a Plexiglas box (43 cm x 27.5 cm x 43 cm) with a light source at the top was used as a test chamber.[65] At least 100 flies from each genetic line/age were tested. Each fly was scored for its ability to fly in an upward (U=6), horizontal (H=4), or downward (D=2) fashion towards a light source, and flies with no flight ability received a score of zero (N=0). To calculate the flight index, an equation representative of average flight ability was used: Flight Index (FI)= 6*U/T+4*H/T+2*D/T+0*N/T, where U, H, D, and N represent each fly trajectory listed above, and T=total # of flies. For jump tests, the wings were clipped, and each fly was placed on an inverted fly food vial with concentric rings drawn 0.5 cm apart to measure jump distance. Each fly was tactilely stimulated to jump, and the jump distance was recorded for 10 trials per fly. The top 3 of 10 jump distances were reported, and a total of N=40 flies were tested per line/age.

3.2.6. Transmission electron microscopy of skeletal muscles

Hemi-thoraces were dissected and treated with a relaxing solution containing 10 mM EGTA prior to fixation. The following steps were performed on ice: After incubation in 2 mL primary fixative (3% formaldehyde, 3% glutaraldehyde in 0.1 M sodium cacodylate, pH 7.4), samples were washed 6 X in 2 mL wash buffer (0.1 M sodium cacodylate, pH 7.4). Samples were incubated in 2 mL secondary fixative (1% OsO_4, 0.1 M sodium cacodylate buffer, and 10

mM $MgCl_2$, pH 7.4) for 2 hours, then washed 3 X in HPLC-H_2O. All subsequent steps were performed at room temperature. An acetone dehydration series was performed at 30 minutes each: 25%, 50%, 75%, 95%, and 3X 100% anhydrous acetone. Samples were infiltrated in fresh Epon mix [16.2 mL EM bed-812, 10.0 mL Dodecenyl Succinic Anhydride, 8.9 mL NMA (Nadic Methyl Anhydride), 0.6 mL *2,4,6*-Tris(dimethylaminomethyl)phenol (DMP-30)] for 2 hours each using increasing ratios of Epon:dry acetone (1:3, 1:1, 3:1). Following infiltration in 100% Epon for 16 hours, samples were oriented in Epon filled BEEM capsules, and polymerized at 60°C for 1 day under vacuum. Thin sections (50 nm) were cut using a Diatome diamond knife on a Leica Ultramicrotome, and collected on formvar-coated grids. Grids were stained with 2% uranyl acetate for 20 minutes. Images were obtained at 120kV on a FEI Tecnai 12 transmission electron microscope.

Measurements of average distances between adjacent thick filaments were performed with a custom-written Python script. A representative image of the original micrograph (220,000x magnification) is shown in Fig. 3.4A. For this procedure, the image was inverted using the cv2.threshold function, and grain noise was minimized using the cv2.adaptiveThreshold, cv2.morphologyEx, and cv2.blur functions. Thick filament centers were detected using the cv2.HoughCircles function and the following parameters: HOUGH_GRADIENT, 1, 100, param1=100, param2=18, minRadius=9, maxRadius =15. Detections were overlayed onto the original micrograph to confirm that detections align with thick filament centers (Fig. 3.4B). The positions of thick filament centers that were missing from detections were manually added, and erroneous detections were removed. The pixel coordinates of the six closest lattice neighbors from each thick filament center were determined automatically using the Nearest Neighbor Search algorithm. The maximum pixel distance between neighbor detections was set to a value that excludes non-neighbors; A topographical map of neighbor assignments was generated for confirmation (Fig. 3.4C). Average neighbor pixel distances were determined for thick filament centers containing six true lattice neighbors,

which excluded measurements for thick filament centers located on the edges of micrographs. For each biological sample, average pixel distances between adjacent thick filaments were determined for ≥ 700 thick filament centers. Values were converted to nanometers using the scale bar, and thick filament distances were averaged for each biological replicate.

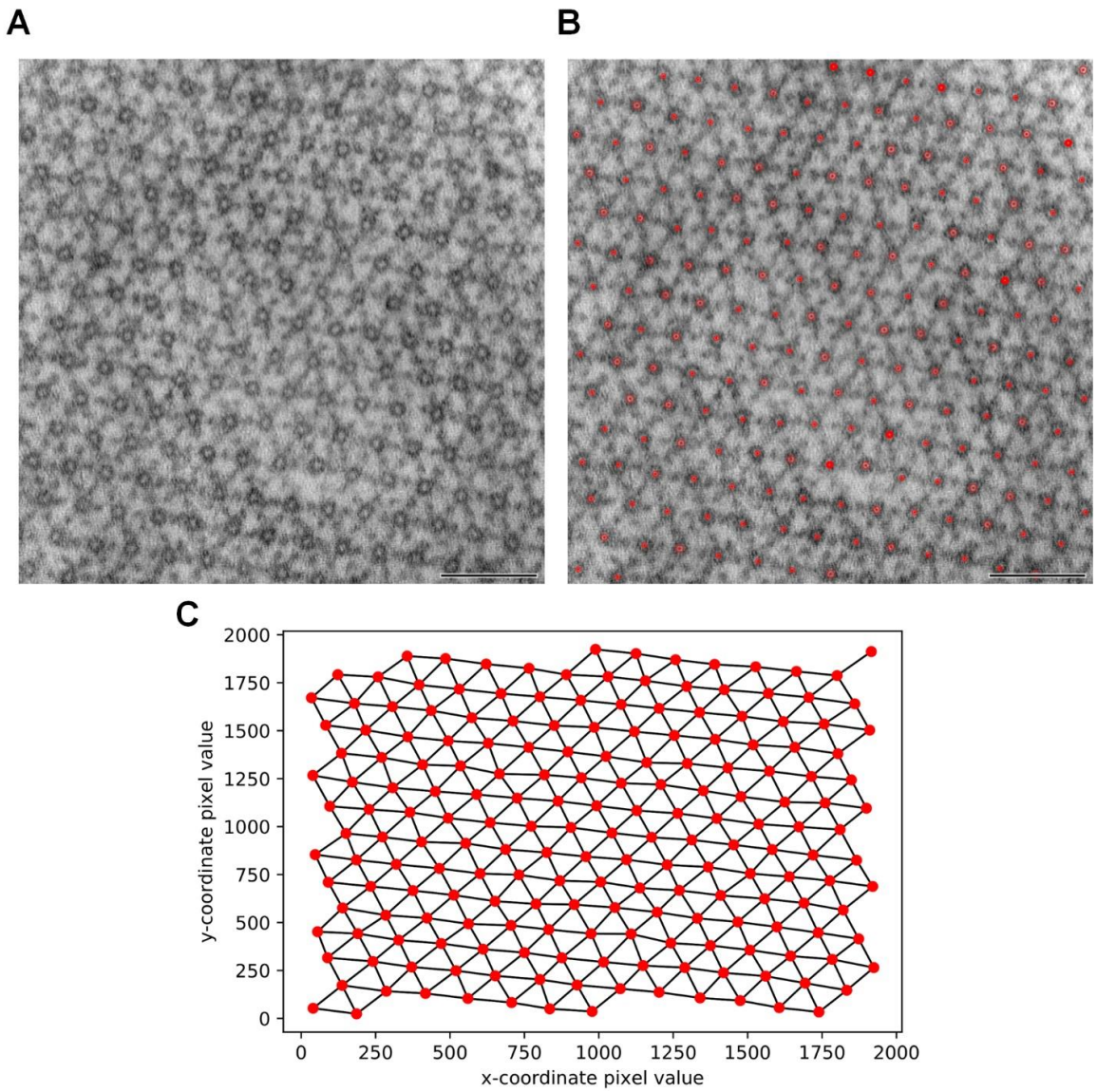

Figure 3.4- Analysis of inter-thick filament spacing of IFMs
A) Transmission electron microscopy image of IFMs in transverse orientation from 3 week-old transgenic wild-type *PwMhc2* controls. **B)** Thick filament centers were detected in a semi-automated fashion, and overlayed onto the original micrograph to confirm accuracy of detections. **C)** The x,y coordinates of centers were determined using a specialized Python-based software. Scale bars, 0.1 µm.

3.3. Results

3.3.1. Actin co-sedimentation

Co-sedimentation assays were performed to estimate the binding affinity of S532P S1 for F-actin. Binding curves were generated by incubating increasing amounts of F-actin with fixed amounts of control or mutant myosin S1 isolated from His-tagged lines (Chapter 2). Following centrifugation, a majority of S1 remained soluble in actin-free S1 controls, while F-actin was insoluble in S1-free actin controls (Fig. 3.5A). Electrophoretic gels of centrifuged samples were scanned and densities of S1 bound fractions were fit to a hyperbolic function to determine binding affinity (K_d) for F-actin (Fig. 3.5B). Both recombinant mutant and control S1 exhibited tight binding affinity for F-actin (K_d= 2003 ± 1040 nM for S532P; 1260 ± 963 nM for control), and K_d values did not significantly differ (P= 0.42). However, the average K_d value for the S532P mutant S1 was ~1.6 fold higher relative to control S1, indicating a trend towards lower actin affinity in this mutant. Though the co-sedimentation method is a standard approach for measuring actin binding affinity, it is challenging to obtain accurate K_d measurements using this method due to the irreversible binding of actomyosin during sedimentation. Thus, we also utilized other methods to determine whether the S532P mutation affects actin binding, including structural-based approaches (Chapter 2), biochemical analysis of actin-stimulated ATPase activity (Chapter 3), and muscle mechanics (Chapter 3).

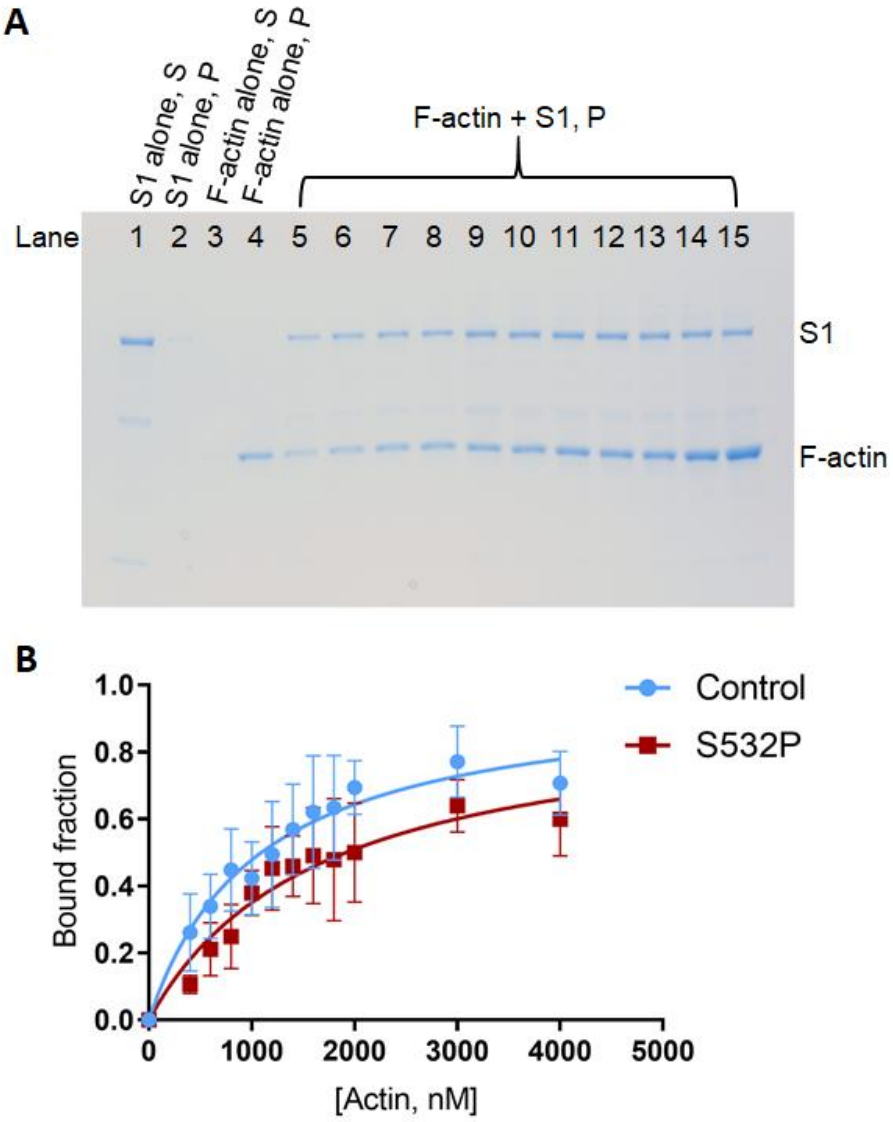

Figure 3.5- Co-sedimentation of S532P IFI S1 and control IFI S1 for F-actin
A) A representative SDS-polyacrylamide gel showing insoluble pellet (P) fractions of F-actin and IFI S1-containing samples over increasing F-actin concentrations (Lanes 5-15: 0.4, 0.6. 0.8, 1, 1.2, 1.4, 1.6, 1.8, 2, 3, and 4 μM). Supernatant (S) and pellet (P) fractions of samples containing S1 or F-actin alone are shown as controls (Lanes 1-4). **B)** The bound fractions in actomyosin-containing samples were determined via densitometry and plotted vs. F-actin concentration. To determine bound fractions, the density of S1 in the pellet fraction relative to total protein content was calculated, and the fraction of pelleted S1 in a S1-only control was subtracted from this value. Data are reported as mean ± SD. To determine actin binding affinity, the dissociation constant of S1 for F-actin (K_d) was defined as the F-actin concentration required to reach half maximal binding (B_{max}).

3.3.2. Fly line validation

To study the disease mechanisms induced by a myosin-induced DCM mutation, we used *P* element transformation to engineer fly lines harboring the S532P myosin mutation lacking a His-tag. Since lines produced by *P* element transformation can exhibit position effects due to the chromosomal site of insertion, we produced multiple transgenic lines to ensure reproducibility of *in vivo* functional analyses. A total of 39 transgenic lines were obtained. Lines mapping to the third chromosome were crossed into the Mhc^{10} genetic background that is null for endogenous myosin in IFMs and jump muscles.[45]

Table 3.1- Validation *S532P* fly lines
Protein expression levels in IFMs from *S532P* lines (*L1*, *L2*, and *L3*) relative to wild-type *yw* flies were determined using densitometry. Data are reported as mean ± SEM. RT-PCR of RNA isolated from IFMs was performed to verify that each line expresses mutant myosin in absence of endogenous myosin, and to verify that alternative exon splicing was not disrupted. ✓ represents verification of the mutation or normal IFI alternative exon.

Genotype	Protein expression	Mutation present	Exon 3b	Exon 7d	Exon 9a	Exon 11e	Exon 15a
S532P-L1	100.6 ± 3.8	✓	✓	✓	✓	✓	✓
S532P-L2	101.5 ± 1.3	✓	✓	✓	✓	✓	✓
S532P-L3	99.0 ± 2.2	✓	✓	✓	✓	✓	✓

We selected the fly lines with wild-type protein expression levels for further analyses. SDS-PAGE analysis of upper thoraces of young mutant flies confirmed that these lines express normalized ratios of myosin to actin at wild-type levels (Table 3.1). RT-PCR of IFM lysates confirmed expression of RNA encoding mutant myosin, the absence of endogenous myosin expression, and the absence of alternative splicing defects in these lines (Table 3.1).

3.3.3. ATPase assay

Steady-state ATPase parameters of myosin obtained from dissected IFMs were assessed to determine the impact of the S532P mutation on the enzymatic activity of myosin (Fig. 3.6). Both basal Mg-ATPase and Ca-ATPase did not significantly differ for S532P myosin compared to wild-type myosin (0.22 ± 0.08 sec^{-1} vs. 0.28 ± 0.11 sec^{-1}, P=0.32 for Mg-ATPase; 10.81 ± 6.38 sec^{-1} vs. 15.77 ± 3.33 sec^{-1}, P=0.16 for Ca-ATPase). Mg-ATPase activity in the presence of increasing concentrations of F-actin was measured to determine if the S532P mutation affects actin-dependent activity. The V_{max} (maximum ATPase rate) of actin-stimulation was reduced ~2-fold for S532P relative to wild-type myosin (0.59 ± 0.28 sec^{-1} vs. 1.86 ± 0.49 sec^{-1}, P=0.0011). The K_m of actin concentration required to reach 50% V_{max} did not differ relative to wild type (0.68 ± 0.33 uM vs. 0.80 ± 0.39 uM, P= 0.61).

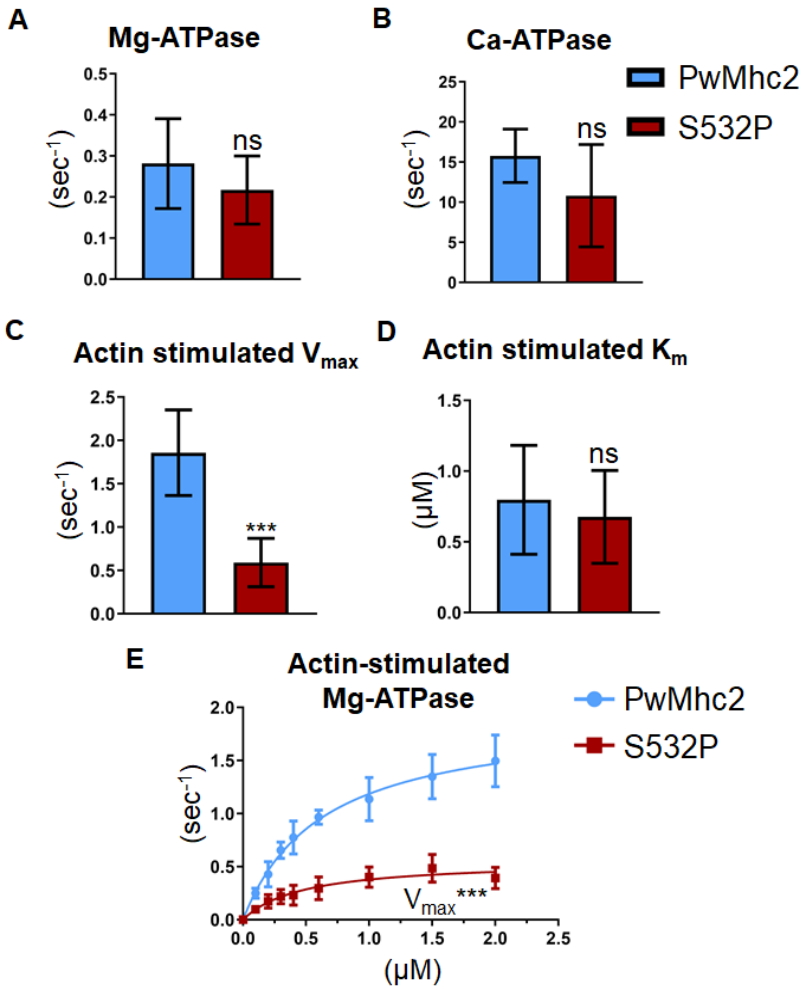

Figure 3.6- ATPase activity of S532P myosin
Full-length myosin isolated from IFMs of *S532P* lines and wild-type transgenic controls (*PwMhc2*) was assessed for the following ATPase activity parameters: **A)** Basal Mg-ATPase activity, **B)** Ca-ATPase activity, **C)** V_{max} of actin-activated Mg-ATPase, and **D)** actin affinity relative to ATPase (K_m). **E)** To determine actin-activated activity, Mg^{2+} basal ATPase activities were subtracted from measured basal ATPase values and over increasing concentrations of F-actin. Values were fit with the Michaelis-Menten equation to determine the V_{max} and K_m. Data are reported as mean ± SD. Statistical significance was determined using Student's t-tests (ns= not significant, ***p<0.001).

3.3.4. Muscle mechanics

A sinusoidal analysis was performed to determine muscle mechanical properties influenced by the S532P mutation. For this, individual fibers were isolated from IFMs of 2-3 day-old flies and subjected to small length changes in a mechanical rig. The amplitudes and phases of force and length traces were measured to elucidate mechanical properties such as power, force, and rate constants of the myosin cross-bridge cycle. Fibers isolated from multiple mutant fly lines (*L1*, *L2*, and *L3*) were independently assessed. The rate constant 2πb, which is influenced by the rates of attachment to actin and/or the powerstroke step, was significantly lower for fibers from all three mutant lines compared to controls (Table 3.2, $p<0.05$, One-Way ANOVA Dunn's Method). The rate constant 2πc, which is influenced by the rate of detachment from actin, was significantly higher for fibers from all three mutant lines compared to controls (Table 3.2, $p<0.001$, One-Way ANOVA Holm-Sidak method).

Table 3.2- Muscle apparent rate constants of *S532P* fibers
A sinusoidal analysis was performed on *PwMhc2* (N = 10), *S532P-L1* (N = 8), *S532P-L2* (N = 6), and *S532P-L3* (N = 8) IFM fibers isolated from homozygotes. Full genotypes are shown in parenthesis: *S532P* lines (Mhc^{10}/Mhc^{10}; *P[S532P]/P[S532P]*); *PwMhc2* transgenic controls (*P[PwMhc2]/P[PwMhc2]; Mhc^{10}/Mhc^{10}*). Mean ± SEM are reported. One-way ANOVAs were performed to determine statistical significance (***p<0.001, Holm-Sidak method; *p<0.05, Dunn's Method).

Genotype	A	B	2πb (s^{-1})	C	2πc (s^{-1})
PwMhc2	341.8 ± 33.4	2250.3 ± 237.1	1680.8 ± 74.4	2190 ± 218.9	2845.0 ± 122.6
S532P-L1	356.9 ± 70.6	624.3 ± 131.6*	945.6 ± 39.6*	550.4 ± 107.7*	6046 ± 506.0***
S532P-L2	309.8 ± 9.24	485.2 ± 40.9*	766.6 ± 25.7*	436.3 ± 25.3*	6660.2 ± 650.32***
S532P-L3	292.6 ± 19.3	575.9 ± 97.3*	878.9 ± 42.3*	552.4 ± 83.0*	6321.7 ± 582***

Fibers from all three mutant lines displayed depressed maximum power production ($p<0.05$, One-Way ANOVA Dunn's Method) (Fig. 3.7) and lower frequency of maximal power, f_{max} ($p<0.001$, One-Way ANOVA Holm-Sidak method) (Fig. 3.7). To determine actin-stimulated ATPase activity (V_{max}) and actin affinity relative to ATPase (K_m), we varied ATP concentration

from 20 mM to 0.5 mM while performing a sinusoidal analysis. Values for f_{max} were plotted over changing [ATP], and fit with the Michaelis-Menten equation (Fig. 3.8). V_{max} was significantly lower for *S532P* mutant fibers ($p<0.001$, One-Way ANOVA Holm-Sidak method), but there was no change in K_m. Overall, the transgenic myosin form produced by our models shows disrupted actomyosin interactions, causing reductions in actin-stimulated ATPase activity and power output.

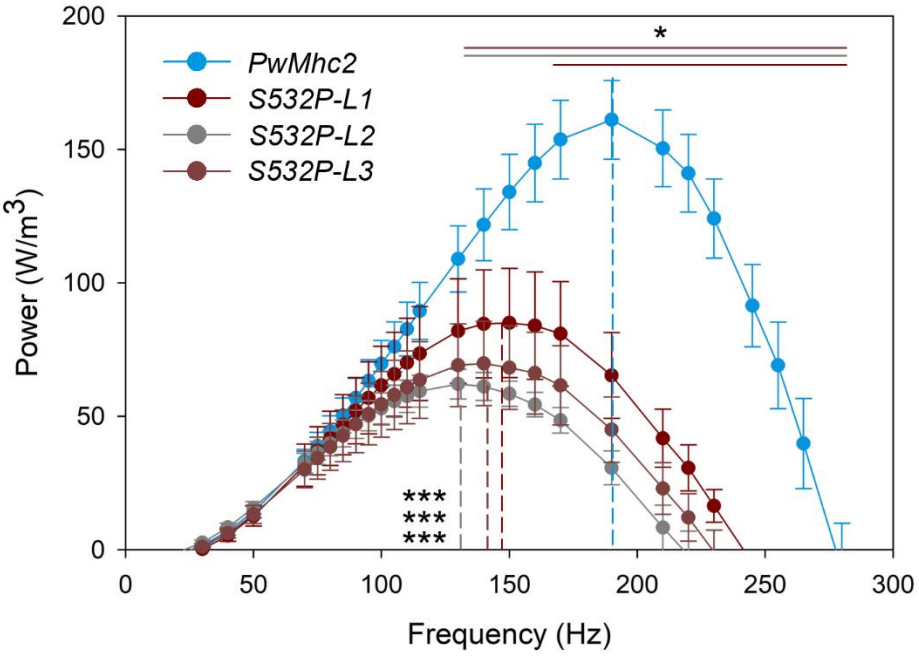

Genotype	Max Power (W/m^3)	f_{max} (Hz)
PwMhc2	164 ± 15	191 ± 5
S532P-L1	86 ± 20*	148 ± 4***
S532P-L2	63 ± 6*	131 ± 4***
S532P-L3	71 ± 16*	143 ± 4***

Figure 3.7- Skinned fiber power output of *S532P* fibers
Maximum power output and the frequency at which maximum power is generated (f_{max}) were measured by sinusoidal analysis of IFM fibers from homozygotes. Full genotypes are shown in parenthesis: *S532P* lines (Mhc^{10}/Mhc^{10}; *P[S532P]/P[S532P]*); *PwMhc2* transgenic controls (*P[PwMhc2]/P[PwMhc2]; *Mhc^{10}/Mhc^{10}). One-Way ANOVAs were employed to determine statistical significance, where *p<0.05, Dunn's method; ***p<0.001, Holm-Sidak method. f_{max} values are indicated by the vertical dashed lines. N=10 for *PwMhc2*, N=8 for *S532P-L1*, N=6 for *S532P-L2*, and N=8 for *S532P-L3*.

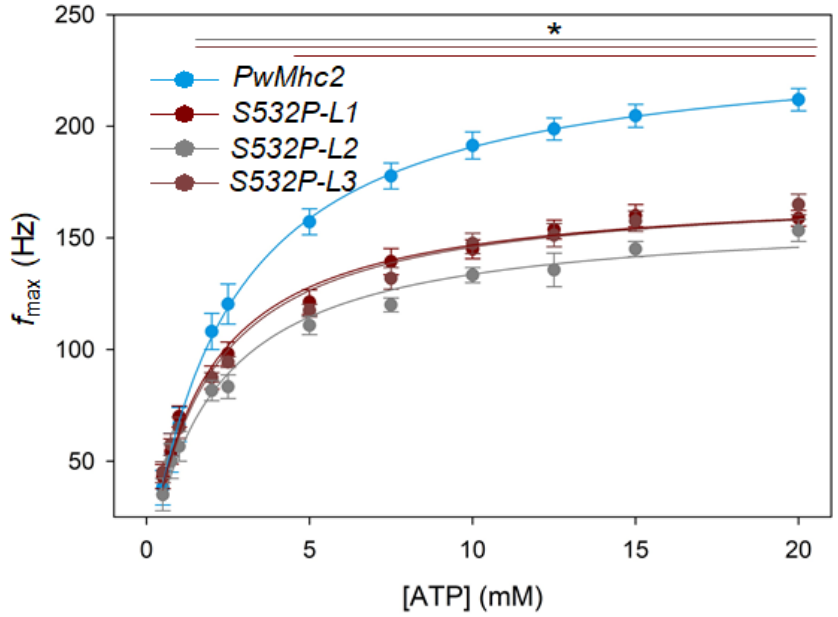

Genotype	V_{max}	K_m
PwMhc2	243.9 ± 7.5	3.0 ± 0.6
S532P-L1	173.6 ± 3.1***	1.7 ± 0.2
S532P-L2	162 ± 5.4***	2.2 ± 0.5
S532P-L3	172.5 ± 10.2***	1.8 ± 0.1

Figure 3.8- ATP response of *S532P* fibers
Sinusoidal analysis was performed with varied [ATP] to determine actin-stimulated ATPase activity (V_{max}) and actin affinity relative to ATPase (K_m), Values for f_{max} were plotted over changing [ATP], and fit with the Michaelis-Menten equation. Full genotypes of homozygotes are shown in parenthesis: *S532P* lines (*Mhc*^{10}/*Mhc*^{10}; *P[S532P]/P[S532P]*); *PwMhc2* transgenic controls (*P[PwMhc2]/P[PwMhc2]*; *Mhc*^{10}/*Mhc*^{10}). Statistical significance for V_{max} is represented by ***p<0.001, One-Way ANOVA Holm-Sidak method. Horizontal bars indicate statistical differences in f_{max} values (*, p<0.05, One-Way ANOVA Dunn's Method). N=10 for *PwMhc2*, N=8 for *S532P-L1*, N=6 for *S532P-L2*, and N=8 for *S532P-L3*.

3.3.5. Flight and jump tests

Mutant lines were tested for flight and jump muscle function compared to *PwMhc2* (*P* element-transformed wild-type) controls to determine if the S532P mutation causes tissue level muscle functional defects. At 2 days of age, homozygous S532P lines *L1* and *L3* showed no significant difference in flight ability relative to controls (Fig. 3.9A). Homozygous line *S532P-L2* showed reduced flight ability at this age compared to controls [arbitrary units (A.U.) ± S.E.M: 2.70 ± 0.16 vs. 3.70 ± 0.15]. All three lines (L1-L3) displayed reduced flight ability compared to controls by ages 1-week (1.94 ± 0.16, 1.75 ± 0.16, and 2.48 ± 0.12 vs. 3.52 ± 0.12 A.U.) and 3-weeks (1.42 ± 0.17, 1.76 ± 0.14, and 1.84 ± 0.12 vs. 3.32 ± 0.13 A.U.). Changes in flight ability within each line were compared between young 2 day-old flies and aged 3 week-old flies to determine if functional impairments are progressive, akin to the age-related disease progression observed in DCM patients. All three *S532P* lines exhibited a greater decline in flight ability from 2 days to 3 weeks of age compared to controls. Two-way ANOVAs determined that the effects of genotype ($p<0.0001$) and age ($p<0.0001$) as two independent factors, as well as the interaction between age and genotype ($p<0.0001$), contribute to statistically significant differences between groups. Overall, the S532P mutation causes defects in flight ability that are progressive with age. We also assessed heterozygotes to determine if the S532P mutation causes dominant defects in muscle function, akin to the human condition. Heterozygotes display no defects in flight ability compared to controls at 3 weeks of age (Fig. 3.9B), the same age that homozygotes display severe functional defects, suggesting that the detrimental effects of the mutation on muscle function are not dominant.

Mean jump distance was also reduced in all three homozygous mutant lines (*L1*, *L2*, and *L3*) compared to controls at ages 2-day (6.17 ± 0.16, 6.58 ± 0.15, and 4.86 ± 0.13 cm vs. 7.08 ± 0.16 cm) and 1-week (6.41 ± 0.14, 5.76 ± 0.17, and 5.32 ± 0.12 cm vs. 7.89 ± 0.14 cm) (Fig. 3.10). Two-way ANOVAs demonstrated significant differences between control and mutant lines

($p<0.0001$), while the effects of age as an independent factor were not statistically significant. Though there was a statistically significant interaction between age and genotype ($p<0.0001$), this could be explained by the increase in jump muscle function observed in controls with age, rather than a deterioration in muscle function with age in mutant lines. Jump muscle function did not worsen from 2-days to 1-week of age in two of the lines tested (*L1* and *L3*), contrary to the progressive and rapid decline in muscle function observed in IFMs.

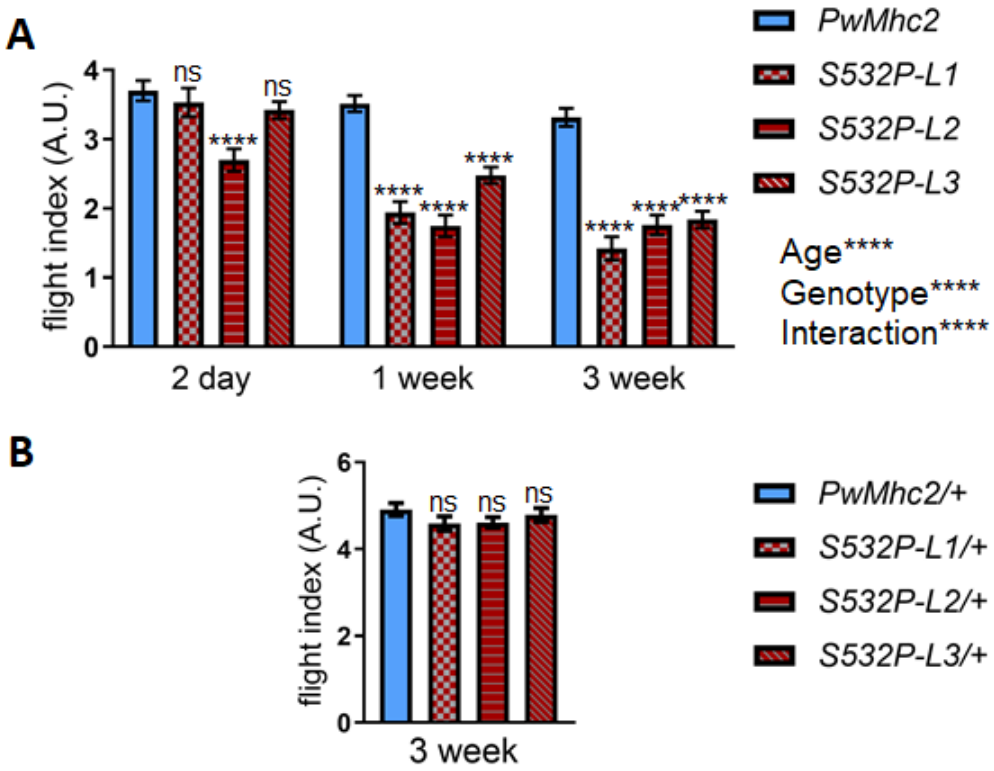

Figure 3.9- Flight abilities of *S532P* mutant lines

Homozygous (**A**) and heterozygous (**B**) *S532P* mutant lines (*L1*, *L2*, and *L3*) were crossed into a Mhc^{10} (myosin-null in IFMs and jump muscles) background. Flight index was calculated as 6*U/(# flies) +4*H/(# flies) +2*D/(# flies) +0*N/(# flies) where each fly was assigned a score for flight upward (U), horizontally (H), downward (D) or the inability to fly (N). Values represent mean ± SEM. A total of N≥100 flies were tested for each line/age. **A**) Full genotypes of homozygotes are shown in parenthesis: *S532P* lines (Mhc^{10}/Mhc^{10}; *P[S532P]/P[S532P]*); *PwMhc2* transgenic controls (*P[PwMhc2]/P[PwMhc2]*; Mhc^{10}/Mhc^{10}). A two-way ANOVA was employed to test if the effects of genotype and age were significant (****p<0.0001, ns= non-significant). Multiple comparisons between mutant lines and age-matched controls are also shown. **B)** Full genotypes of heterozygotes are shown in parenthesis, where "-" indicates there is no *P* element on the homologous chromosome: *S532P*/+ lines (Mhc^{10}/+; *P[S532P]/-*); *PwMhc2/+* transgenic controls (*P[PwMhc2]/-*; Mhc^{10}/+). A one-way ANOVA was employed to determine statistical significance between mutant lines and controls (ns= non-significant).

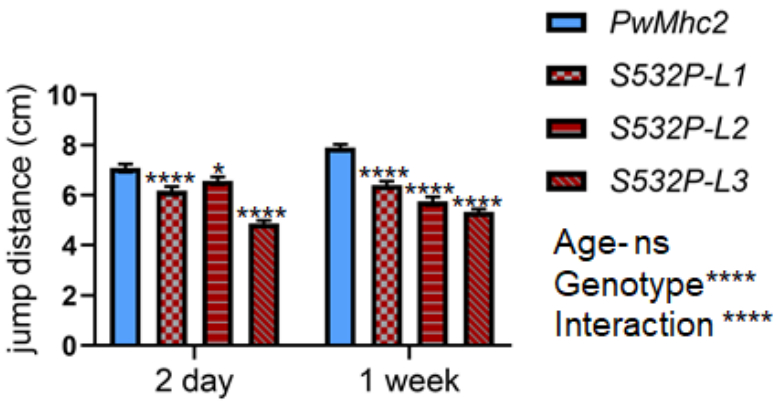

Figure 3.10- Jump abilities of *S532P* mutant lines
Homozygous *S532P* mutant lines (*L1*, *L2*, and *L3*) were crossed into a Mhc^{10} (myosin-null in IFMs and jump muscles) background. The top 3 of 10 jump distances were reported, and a total of N=40 flies were tested per line/age. Values represent mean ± SEM. Full genotypes are shown in parenthesis: *S532P* lines (Mhc^{10}/Mhc^{10}; *P[S532P]/P[S532P]*); *PwMhc2* transgenic controls (*P[PwMhc2]/P[PwMhc2]*; Mhc^{10}/Mhc^{10}). A two-way ANOVA was employed to test if the effects of genotype and age were significant (ns- non-significant, ****p<0.0001). Multiple comparisons between mutant lines and age-matched controls are also shown (*p<0.05 and ****p<0.0001).

3.3.6. Transmission electron microscopy of IFMs

Transmission electron microscopy was performed on IFMs from aged 3 week-old *S532P* homozygous mutants and controls to determine if expression of the S532P mutation causes defects in myofibrillar assembly or maintenance. Transverse sections of mutants and controls displayed myofibrils with normal, rounded morphology (Fig. 3.11: A-B), and a normal double hexagonal array of thick and thin filaments (Fig. 3.11: C-D). In longitudinal sections, myofibrils displayed normal parallel organization (Fig. 3.12: A-B), and sarcomeres displayed normal organization with intact myofilaments (Fig. 3.12: C-D). No differences in average inter-thick filament spacing distances (Fig. 3.11E) or sarcomere lengths (Fig. 3.12E) were detected between mutants and controls. Overall, no disruption in sarcomere ultrastructure was observed in *S532P* mutants, suggesting that flight impairment in these lines was not caused by myofibrillar assembly defects or degeneration.

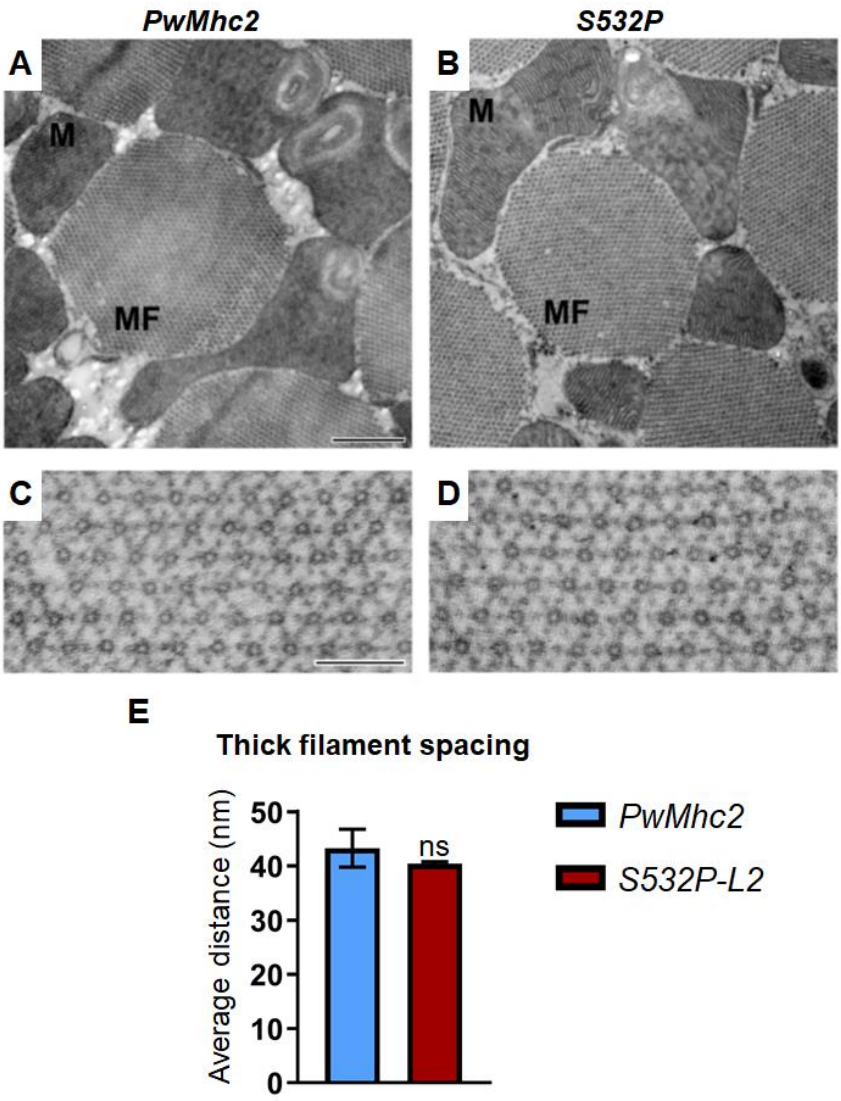

Figure 3.11- Ultrastructure of *S532P* IFMs in transverse orientation
Transmission electron micrographs of thin-sectioned IFMs in transverse orientation were obtained from 3 week-old homozygous *PwMhc2* control or *S532P* mutant lines (*L1* or *L2*) in a *Mhc*^{10} (myosin-null in IFMs and jump muscles) background. **A-B)** Low magnification images showing myofibrillar morphology. MF- myofibril, M- mitochondrion. Scale bar, 0.5 µm. **C-D)** High magnification images showing hexagonal array of thick and thin filaments Scale bar, 0.1 µm. **E)** Inter-thick filament spacing averages were determined from micrographs using a custom-written Python script. Values represent mean ± SD. Statistical significance was determined using Student's t-tests (ns= not significant).

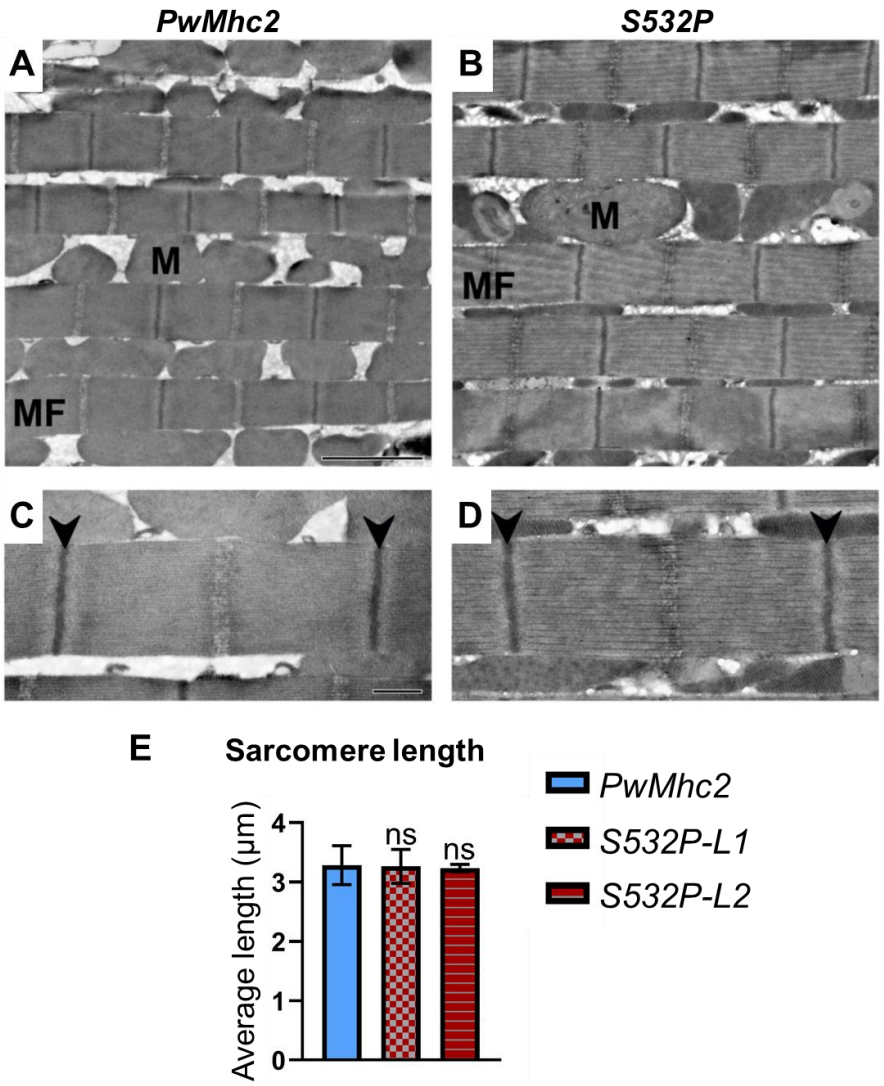

Figure 3.12- Ultrastructure of *S532P* IFMs in longitudinal orientation
Transmission electron micrographs of thin-sectioned indirect flight muscles (IFMs) in longitudinal orientation were obtained from 3 week-old homozygous *PwMhc2* control or *S532P* mutant flies in a Mhc^{10} (myosin-null in IFMs and jump muscles) background. **A-B)** Low magnification images showing myofibrillar organization. MF- myofibril, M- mitochondrion. Scale bar, 2 µm. **C-D)** High magnification images showing sarcomeres bordered by Z-disks (arrowheads). Scale bar, 0.5 µm. **E)** Average sarcomere lengths were measured using Image-J software. Values represent mean ± standard deviation. Statistical significance was determined using Student's t-tests, where NS= non-significant difference compared to controls.

3.4 Discussion

The S532P myosin DCM mutation, located within the actin-binding region of the motor domain, was introduced into Drosophila myosin heavy chain to determine the biochemical, cell biological, and physiological mechanisms of disease. Given that the S532 residue localizes to an α-helix within an actin binding site[74], we hypothesized that a proline substitution at that residue would bend or kink the helix and disrupt actin binding affinity.

Though we observed a trend of lower affinity (i.e. higher K_d) in the mutant compared to wild-type myosin using the co-sedimentation approach, the difference was not significant. However, it is challenging to determine an accurate dissociation constant using this method, since detachment of actin is limited in insoluble actomyosin fractions. Thus, we performed a sinusoidal analysis on skinned IFM fibers to determine rate constants associated with actin binding. The muscle apparent rate constant $2\pi b$ was lower in S532P homozygous fibers, suggesting that the mutation slows a work-generating step involved in actin attachment and/or the powerstroke step. The rate constant $2\pi c$ was higher in mutant fibers, suggesting that the mutation lowers the duration of one or more strong actin binding states (i.e. with ADP bound state after P_i release, or the nucleotide-free state), causing myosin to detach more quickly from actin. Overall, S532P myosin spends less time bound to actin during the cross-bridge cycle, which is expected to lower the duty ratio (fraction of myosin heads bound to actin) and decrease force output.[75] It remains unknown whether the mutation affects the cooperativity of myosin binding events. The precise actin binding step(s) of the chemomechanical cycle affected by the mutation are also unclear. Given the effects on both $2\pi b$ and $2\pi c$, it is possible that the mutation disrupts the transition from the weakly-bound to strongly-bound actomyosin states. Future studies will determine the exact intramolecular structural rearrangements associated with alterations in actin binding properties using cryo-electron microscopy (see Chapter 2).

Previous reports that modeled the S532P mutation in mouse α-MyHC support our hypothesis that this mutation interrupts actomyosin interactions. Schmitt et al. determined the actin binding properties of S532P myosin at the single molecule level using a laser trap assay.[30] The magnitude of displacement associated with the step size was significantly depressed in the mutant. Surprisingly, the duration of the time in which myosin remained bound to actin after the powerstroke (t_{on}) was longer. However, the authors acknowledged that individual kinetic steps affected by t_{on} could not be determined at the sub-saturating levels of ATP used in the assay, since t_{on} is limited by both the rates of MgATP binding and ADP release. Muscle mechanics revealed that the rate constant $2\pi b$ is higher in skinned *S532P*/+ mouse myocardial fibers[67], contrary to the depressed motor function observed in molecular level studies on myosin isolated from homozygous mutants hearts.[30] Palmer et al. attributed this discrepancy to potential effects of sample preparation, assay design, or differences between genotypes or post-translational modifications.[67] They also acknowledged that some of the data were slightly misrepresented by the model equation for complex modulus, which may also account for the inconsistency. Our data suggest that the rate constant $2\pi b$ is lower in S532P Drosophila IFMs. Differences in the backbone between mouse α-MyHC and Drosophila IFI MHC may have a disparate effect on their actin binding properties. Additionally, the exact ratio of mutant to non-mutant α-MyHC in mouse *S532P*/+ fibers is unknown.[67] Effects of genotype may account for some discrepancies, since there may be functional compensation by wild-type myosin in mouse *S532P*/+ fibers. Rate constant $2\pi c$ was significantly higher in mouse *S532P*/+ fibers at intermediate concentrations [0.4-0.8 mM] of Mg-ATP, consistent with our fly model. Despite minor differences in the actin binding properties, our data support a similar overarching conclusion that the S532P mutation affects actin binding.

The ability of myosin to hydrolyze ATP in response to actin binding is necessary for normal progression through the chemomechanical cycle. The actin-stimulated ATPase activity (V_{max}) of myosin isolated from Drosophila IFMs is consequently >6-fold higher in response to

actin binding relative to basal Mg-ATPase activity.[76] We show here that the S532P mutation reduces actin-stimulated ATPase activity (V_{max}) in absence of changes in basal Mg-ATPase activity, suggesting that impaired actomyosin interactions are responsible for the depressed motor function in the mutant. The actin binding affinity (K_m) relative to the V_{max} of ATPase was unaffected by the mutation. Skinned IFM fibers also exhibit reductions in actin-stimulated ATPase activity, suggesting similar effects of the mutation at the level of the muscle fiber. We postulate that the S532P mutation induces a conformational change that impairs closure of the actin binding cleft and slows P_i release. This is expected to lower the rate of transition from weak to strong actin binding[77,78], consistent with our finding that apparent rate constants $2\pi b$ and $2\pi c$ are respectively lower and higher in skinned IFM mutant fibers. Similarly, a W546A mutation of chicken gizzard heavy meromyosin located within a helix structurally analogous to β-MyHC S532 dramatically lowers the V_{max} of actin stimulated ATPase activity without altering K_m.[79] The authors suppose that the mutation interrupts actin cleft closure, slowing the rate of P_i release without affecting actin affinity. Consistent with our work, expression of the S532P mutation in human β-MyHC short subfragment-1 (sS1)[74] and mouse α-MyHC[30] lowered the V_{max} of actin-stimulation, though the difference was not significant for α-MyHC.[30] The K_m of actin stimulation was significantly higher for human β-MyHC sS1[74], suggesting lower actin binding affinity, while K_m was unchanged for α-MyHC.[30] Discrepancies in ATPase parameters of these S532P myosins may arise from differences in myosin backbone, sample preparation, or whether full length or a myosin sub-fragment is tested. However, all share a common mechanism of impaired actomyosin interactions resulting in reduced actin-stimulated ATPase activity.

Previous reports revealed that the S532P mutation reduces the loaded actin sliding velocity[74] and force generating capacity[8] of human β-MyHC sS1. Additionally, the maximum isometric force of S532P mouse α-myosin heavy chain was significantly reduced in a laser trap assay.[80] Thus, we hypothesized that S532P myosin is underfunctional and that its expression in Drosophila would yield muscle functional deficits. S532P IFM fibers exhibit depressed power

production, and a reduction in the frequency at which maximum power was produced, suggesting slower overall muscle speed. Flight testing revealed progressive declines in skeletal muscle function, consistent with the progressive nature of reduced cardiac function in human DCM patients. The causes of functional decline with age remain unknown. Age-related changes in gene expression[81-83], protein expression[84], as well as damage to lipids, proteins[85,86], and organelles[85] may play a role in exacerbating muscle functional deficits. Ultrastructural properties of IFMs are normal in 3-week-old *S532P*/*S532P* flies, suggesting that the severe reductions in muscle function at this age are not due to structural deterioration of myofibrils. Similarly, the hypoactive A261T myosin mutation which lowers actin affinity, reduces actin-activated ATPase activity, causes defects in flight ability and yields cardiac dilation in Drosophila does not lead to structural deterioration of IFMs.[59,87] Jump ability was also reduced in *S532P*/*S532P* flies but did not worsen with age. Though differences in protein backbone and muscle physiology are expected to influence the effects of the mutation, we expect that our data are relevant to disease mechanisms in cardiomyocytes since the mutation is located in a well-conserved actin-binding site. Overall, our data support the hypothesis that depressed motor activity in S532P MHC reduces muscle function in Drosophila.

We successfully produced the first Drosophila model of myosin-induced DCM and determined the mechanistic basis of disease. Drosophila is useful for classifying myosin cardiomyopathy mutations into those that either enhance or depress motor function.[12,13] Since the S532P myosin form is underfunctional, treatment with a myosin activating drug may restore motor function of DCM myosin and prevent disease onset or progression. The small molecule omecamtiv mercarbil (OM) specifically binds and activates cardiac myosin by increasing the rate of P_i release, promoting a more rapid transition to the strong actin binding state.[88,89] The duration of strong binding is also increased by OM, which enhances contractility in cardiomyocytes.[74,90] OM is currently in phase 3 clinical trials for the treatment of systolic heart failure and is a promising drug candidate for the treatment of myosin-induced DCM.[91,92] Future

work can exploit the Drosophila model as a platform for drug screening to provide insight into effective therapeutic interventions for human patients.

Chapter 3, in full, contains unpublished material coauthored by Trujillo, Adriana S.; Puthawala, Joy; Hsu, Karen; Loya, Amy; Swank, Douglas; Bernstein, Sanford I. The dissertation author was the primary investigator and author of this chapter.

Chapter 4: Determine whether myosin DCM mutation S532P causes DCM in Drosophila

4.1. Introduction and hypothesis

The goal of this aim is to determine if the Drosophila heart dilates in response to a mutation known to cause DCM in humans, to better understand the link between changes in myosin function and pathological cardiac remodeling. Drosophila contain an open circulatory system, with a simple tube-shaped heart that serves as a pressure pump. Hemolymph enters the heart through five sets of ostia cells. Active contraction of the heart in conjunction with the orchestrated opening and closing of ostia drives hemolymph flow anteriorly through a narrow aorta in the lower thorax.[93] Retrograde pulses also pump hemolymph towards the posterior end of the abdomen to aid in diffusion for tracheal respiration.

DCM patients exhibit enlargement of the cardiac chamber with frequent decreases in systolic function and thinning of cardiac walls.[5,10] Systolic dysfunction involves inadequate emptying of the left ventricle (LV) that is characterized by reductions in ejection fraction (EF, forward stroke volume divided by end-diastolic volume) and fractional shortening (FS, the fraction of diastolic dimension lost during systole). For hereditary DCM, systolic dysfunction can result from mutations that produce cardiac contractile force deficits, including those that reduce actomyosin interaction.[10] Cardiac dysfunction may be moderate to severe and histological findings are nonspecific but may include cardiomyocyte loss. Initially, LV enlargement is thought to involve a compensatory increase in blood volume pumped in the LV, which in turn increases ventricular stroke volume to preserve cardiac output via the Frank-Starling mechanism.[94] However, further LV dilation can cause pathogenic DCM, where the heart walls become thin and weak, causing force deficits and heart failure.[95]

Here, we sought to determine whether our Drosophila model recapitulates clinical features observed in human DCM patients and in a murine DCM model. The age of diagnosis (ages 2-57) and severity of symptoms varied in 19 *S532P/+* patients from a single family.[5] Nearly all patients exhibited clinically relevant enlargements in LV end-diastolic and systolic

diameters and some showed deficits in FS. In another family, 8 of 15 *S532P/+* patients exhibited enlarged LV end-diastolic diameters and deficits in EF indicative of overt DCM.[9] The effects of the S532P mutation are gene dose-dependent in mice, suggesting a disease causative role: heterozygous *S532P/+* mice showed slowly progressing LV dilation and negligible changes in FS, while homozygous *S532P/S532P* mice showed rapid DCM progression and reduced FS. Based on these clinical features, we tested the hypothesis that expression of S532P myosin in Drosophila will cause cardiac contractile defects, leading to pathological remodeling akin to the human condition (i.e., cardiac dilation) in a gene dose-dependent fashion. In support of our hypothesis, Cammarato *et al.*[59] showed that a point mutation (A261T/*D45*) in Drosophila *Mhc* that reduces its enzymatic activity[87] also causes cardiac dilation compared to wild-type (*yw*) hearts. Using a cardiac physiological analysis, these studies demonstrated that the Drosophila heart can dilate in response to a myosin mutation. However, it was previously unknown whether the Drosophila heart dilates in response to a human DCM myosin mutation. To test this, we determined the cardiac physiological and ultrastructural defects observed in *Mhc S532P* flies.

4.2. Materials and methods

4.2.1. Cardiac physiological analysis

Beating, intact hearts from female flies were surgically exposed in oxygenated artificial hemolymph and recorded for 30 seconds using a high-speed, high-resolution video camera (Hamatsu Orca Flash 2.8 CMOS or AOS Promon U750) on a light microscope with a 10x immersion lens. Functional parameters were determined using a Matlab-based semi-automatic heartbeat analysis software.[96,97] For each video, heart chamber dimensions were marked during peak diastole (relaxation) and peak systole (contraction). This was used to determine diastolic (DD) and systolic diameters (SD). Diastolic and systolic diameters were also utilized to calculate

fractional shortening (FS), to determine heart contractility, using the following equation: FS = (DD-SD)/(DD). M-mode diagrams were obtained to reflect contractile parameters from single pixel tracings of heart wall movements (Fig. 4.1). Parameters related to contractile dynamics included durations for diastolic interval, systolic interval, and heart period (diastolic + systolic interval). At least 30 hearts per genetic line were examined for these parameters and the mean values for each parameter were statistically compared to controls using a one-way or two-way ANOVA.

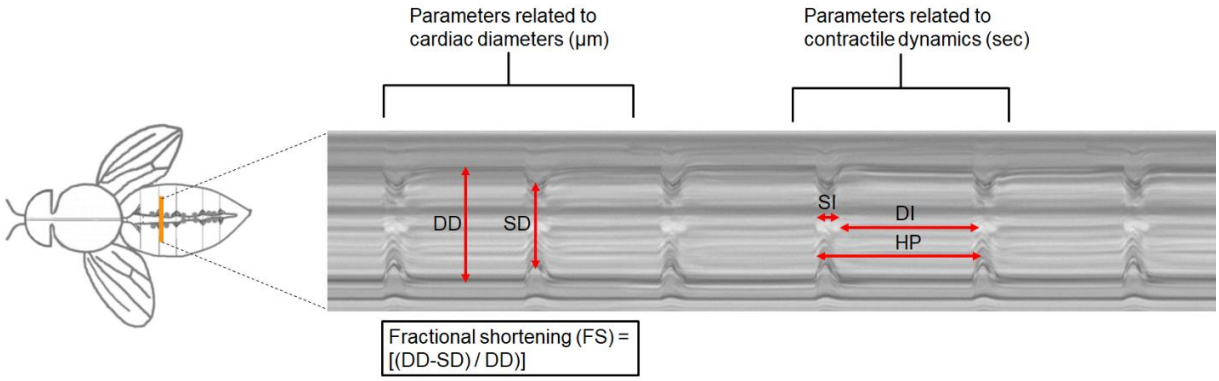

Figure 4.1- A schematic representation of the cardiac physiological analysis
Hearts were surgically exposed in oxygenated artificial hemolymph. High-speed videos of beating hearts were recorded for 30 seconds. For each video, heart chamber dimensions were marked during diastole (relaxation) and systole (contraction). This was used to determine diastolic (DD) and systolic diameters (SD). Diastolic and systolic diameters were also utilized to calculate fractional shortening (FS), to determine heart contractility. To generate M-modes, a 1 pixel-width slice of the video was displayed over time. A representative 5 second portion of an M-mode from a 3 week-old *PwMhc2* heterozygous control is shown. Full genotype is *PwMhc2/-*; Mhc^{1}/+, where "-" indicates there is no *P* element on the homologous chromosome. The orange line marks the region where M-modes were derived. M-modes were used to calculate parameters relating to contractile dynamics, including diastolic interval (DI), systolic interval (SI), and heart period (DI + SI).

4.2.2. Cardiac ultrastructural analysis

The dorsal vessel including the heart was dissected from 4-day old homozygotes. Normal, rhythmic beating was verified to avoid analysis of structurally perturbed hearts. Hearts were bathed with a relaxing solution containing 10 mM EGTA and prepared for TEM, as described in Section 3.2.6.

Transverse thin sections of heart tubes were obtained to determine average cardiac thickness, as previously described.[12] For each measurement, a rectangular area of the cardiomyocyte tissue of 10 µm in length and spanning the distance from the inner to outer cardiac cell wall was highlighted using Adobe Photoshop. The image was imported into NIH ImageJ to calculate the area of the highlighted region. The resulting area was divided by 10 µm to yield the average cardiomyocyte thickness for that highlighted region. Cardiomyocyte thickness measurements from dorsal-side or ventral-side images were averaged among biological replicates.

4.3. Results

4.3.1. Cardiac physiological analysis

To determine the effects of the S532P mutation on cardiac physiology, non His-tagged *Mhc S532P* transgenic flies (see Chapter 3) were crossed into the Mhc^1 background. The Mhc^1 allele is null for endogenous myosin in all muscles and must be maintained over a balancer chromosome to permit viability.[98] Two copies of the *Mhc S532P* transgene rescued lethality of the Mhc^1 homozygotes. Hence, we were able to examine the effects of the mutation in homozygotes, as well as in heterozygotes (akin to the human condition). Since a majority of homozygotes were not viable beyond the first 4 days of age, only young homozygotes were examined. Aged heterozygotes were viable, permitting the comparison of physiological parameters between young and aged heterozygotes.

Young 4 day-old *S532P/+* flies exhibited no differences in diastolic (DD) and systolic (SD) diameters (Fig. 4.2), as well as parameters related to contractile dynamics (Fig. 4.3) [e.g. heart period (HP), systolic interval (SI), and diastolic interval (DI)] relative to controls. Although 4 day-old *S532P-L1/+* flies displayed reduced fractional shortening (FS) compared to controls (% FS ± S.E.M, P value: 0.296 ± 0.010 vs. 0.341 ± 0.009, P= 0.0032), FS did not differ for the other two lines tested (Fig. 4.2). Thus, overall cardiac output was maintained in young *S532P/+* flies. Age-associated decreases in DD were observed in controls from ages 4 days (74.728 ± 1.315 μm) to 3 weeks (67.209 ± 1.262 μm). However, DD did not change with age in *S532P/+* lines. Consequently, aged 3 week-old *S532P/+* flies exhibited a dilated phenotype, characterized by significantly higher DD compared to controls (74.202 ± 1.327, 74.796 ± 1.479, and 74.934 ± 0.889 μm vs. 67.209 ± 1.262 μm). Two-way ANOVAs demonstrated significant differences between control and mutant lines ($p<0.01$), while the effects of age as an independent factor were not statistically significant. Though there was a statistically significant interaction between age and genotype ($p<0.01$), this could be explained by the decrease in diastolic diameters

observed in controls with age, rather than a progressive dilation with age in mutant lines. The mutational effect on DD in absence of changes in SD resulted in increased FS relative to controls at 3 weeks of age (0.390 ± 0.009, 0.383 ± 0.008, and 0.377 ± 0.007 vs. 0.334 ± 0.010). The effects of genotype ($p<0.05$) and age ($p<0.0001$) as two independent factors, as well as the interaction between age and genotype ($p<0.0001$), contribute to statistically significant differences between groups.

Contractile dynamics were also altered in *S532P/+* mutants (Fig. 4.3). Control flies displayed an age-associated increase in HP, which is the length of time required for the completion of a single diastolic and systolic event, from 4 days (0.542 ± 0.037 sec) to 3 weeks (1.392 ± 0.078 sec) of age. DI also increased in controls from 4 days (0.323 ± 0.033 sec) to 3 weeks (1.166 ± 0.075 sec) of age. *S532P/+* mutant lines *L1* and *L3* did not exhibit age-associated changes in HP and DI. The durations of HP (0.546 ± 0.044, 0.466 ± 0.033, and 0.495 ± 0.021 sec vs. 1.392 ± 0.078 sec) and DI (0.375 ± 0.042, 0.313 ± 0.030, and 0.297 ± 0.020 sec vs. 1.166 ± 0.075 sec) were significantly lower in 3 week-old *S532P/+* flies compared to controls, suggesting that heart rhythm is enhanced in mutants. *S532P/+* lines *L1* and *L2* displayed age-associated decreases in SI, while controls did not differ with age. Significant reductions in SI were observed in all three *S532P/+* lines compared to controls at 3 weeks of age (0.171 ± 0.008, 0.153 ± 0.004, and 0.199 ± 0.004 sec vs. 0.228 ± 0.007 sec). The effects of genotype ($p<0.0001$), age ($p<0.0001$), and an interaction effect ($p<0.0001$) contribute to differences in HP, DI, and SI between groups. A reduction in SI suggests that expression of the S532P mutation reduces the duration of the portion of the cardiac cycle in which active tension is produced, which is consistent with our hypothesis that this mutation reduces myosin function. However, given that aged *S532P/+* flies also display increases in contractility and heart rhythm, overall cardiac output is elevated compared to controls.

To determine if expression of two copies of the mutant transgene causes more severe cardiac physiological abnormalities, homozygous *S532P* mutants were crossed into a

Mhc^{1}/*Mhc*^{1} background. Both *S532P* homozygous lines tested (*L1* and L2) exhibited a dilated phenotype, characterized by increases in DD compared to controls (Fig. 4.4) (82.805 ± 1.095, $p<0.0001$ and 75.124 ± 1.675 μm, $p<0.05$ vs. 70.448 ± 1.965 μm). Line *L1* exhibited increased SD (60.624 ± 1.215 μm vs. 47.764 ± 2.038 μm, $p<0.0001$) and decreased FS (0.268 ± 0.011 vs. 0.328 ± 0.013, $p<0.001$), while line *L2* did not show differences in these parameters relative to controls. Line *L1* also showed a reduction in heart period compared to controls (0.466 ± 0.031 sec. vs. 0.593 ± 0.041 sec., $p<0.05$), while the other line tested (*L2*) did not. Diastolic and systolic intervals did not differ in both mutant lines compared to controls. Since young homozygotes displayed a dilated phenotype, while age-matched heterozygotes did not, the mutational effects on cardiac dilation were gene dose-dependent in our fly models.

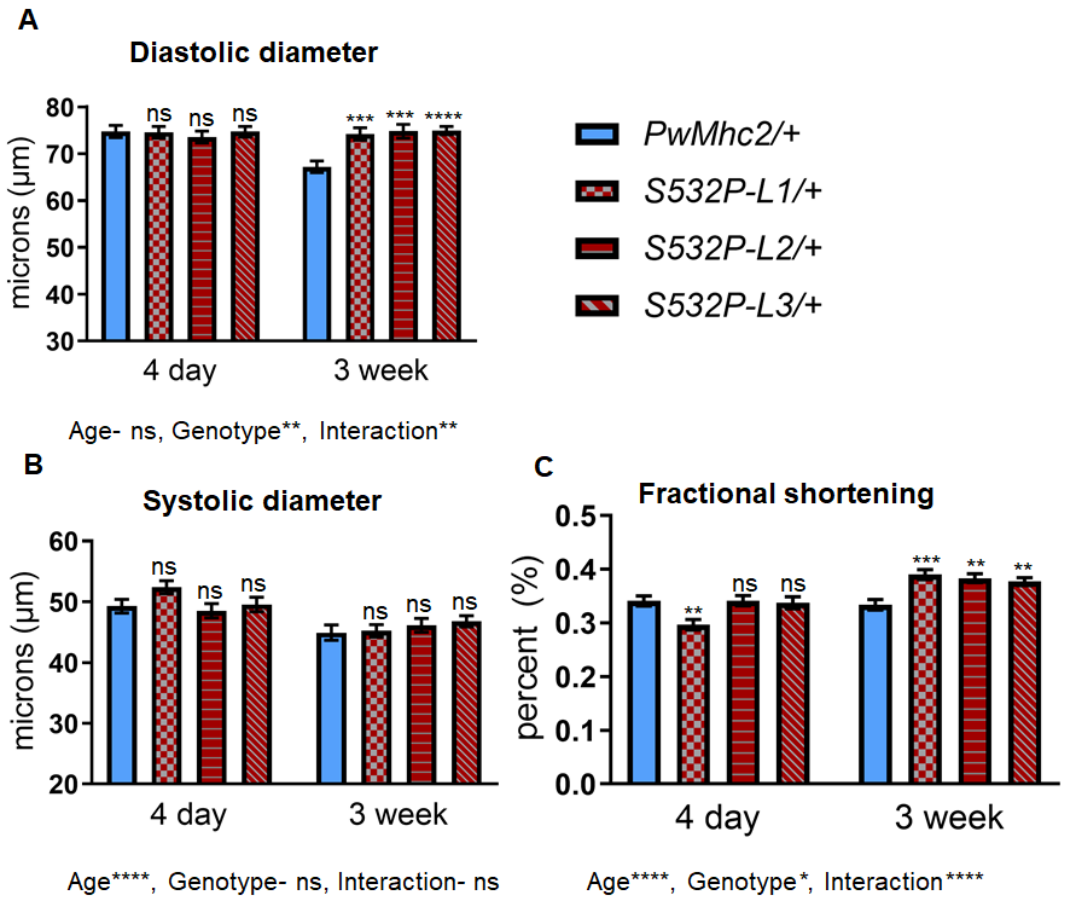

Figure 4.2- Cardiac physiological parameters of *S532P/+* lines, Part I
Cardiac diameters **(A-B)** and fractional shortening **(C)** values of 4 day-old or 3 week-old *PwMhc2* control or mutant *S532P* heterozygous lines (*L1* or *L2*) crossed into a heterozygous *Mhc^{1}-null* background. Full genotypes are shown in parenthesis, where "-" indicates there is no *P* element on the homologous chromosome: *S532P/+* lines (*Mhc^{1}/+*; *P[S532P]/-*); *PwMhc2/+* transgenic controls (*P[PwMhc2]/-*; *Mhc^{1}/+*). Values represent mean ± S.E.M. Two-way ANOVAs were employed to test if the effects of genotype and age were significant for each cardiac parameter investigated (*p<0.05, **p<0.01, ****p<0.0001, and ns= non-significant).

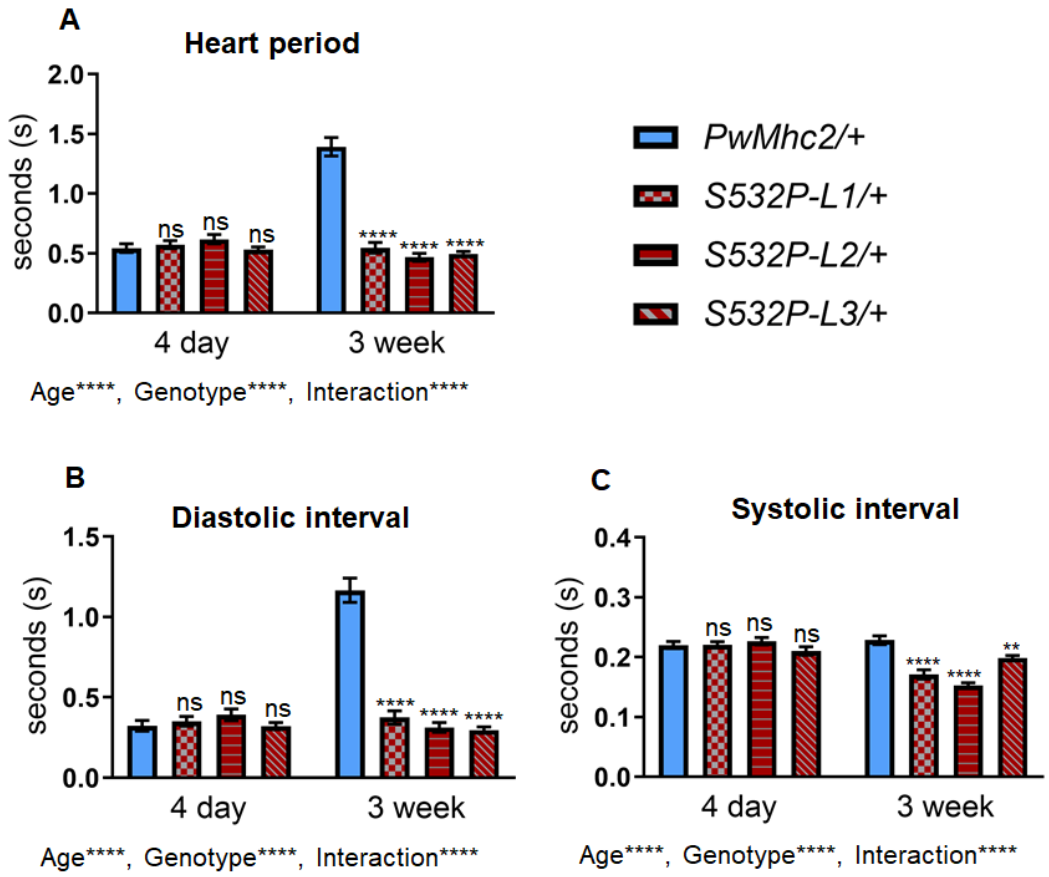

Figure 4.3- Cardiac physiological parameters of *S532P/+* lines, Part II
Heart period **(A)**, diastolic interval **(B)**, and systolic interval **(C)** of 4 day-old or 3 week-old *PwMhc2* control or mutant *S532P* heterozygous lines (*L1* or *L2*) crossed into a heterozygous *Mhc^{1}-null* background. Full genotypes are shown in parenthesis, where "-" indicates there is no *P* element on the homologous chromosome: *S532P/+* lines (*Mhc^{1}/+*; *P[S532P]/-*); *PwMhc2/+* transgenic controls (*P[PwMhc2]/-*; *Mhc^{1}/+*). Values represent mean ± S.E.M. Two-way ANOVAs were employed to test if the effects of genotype and age were significant for each cardiac parameter investigated (*p<0.05, **p<0.01, ****p<0.0001, and ns= non-significant).

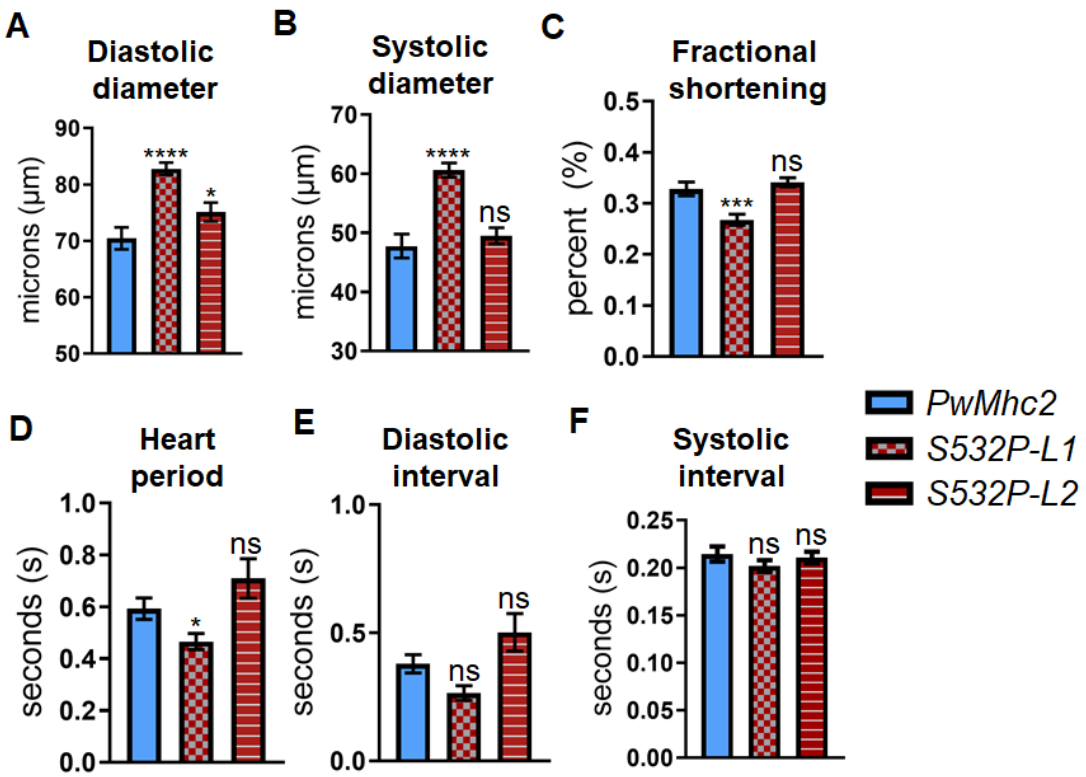

Figure 4.4- Cardiac physiological parameters of *S532P/S532P* lines
Cardiac dimensions **(A-B)**, fractional shortening **(C)**, and dynamics **(D-F)** of 4 day-old *PwMhc2* control or mutant *S532P* homozygous lines (*L1* or *L2*) crossed into a homozygous *Mhc^{1}-null* background. Full genotypes are shown in parenthesis: *S532P* lines (*Mhc^{1}/Mhc^{1}* ; *P[S532P]/P[S532P]*); *PwMhc2* transgenic controls (*P[PwMhc2]/P[PwMhc2]; Mhc^{1}/Mhc^{1}*). Values represent mean ± S.E.M. One-way ANOVAs determined statistical significance compared to controls, where *p<0.05, ***p<0.001, ****p<0.0001, and ns= non-significant.

4.3.2. Cardiac ultrastructural analysis

Transmission electron microscopy (TEM) was employed to determine if the S532P mutation affects cardiac ultrastructure. Micrographs of thin sections across the heart tube reveal a layer of cardiac myocytes as well as a layer of supportive ventral-longitudinal skeletal muscle cells (Fig. 4.5 A-B). Cardiac myofibrils (MF) are oriented mainly perpendicular to the anterior-posterior axis and contain discontinuous Z-disks (arrows), as standardly observed in this tissue.[12,13,99-101] The ultrastructure of 4 day-old *S532P* homozygous mutant hearts are similar to controls, with no obvious signs of myofibrillar disorganization, assembly defects, or degeneration. Dorsal-side and ventral-side cardiac thickness averages do not differ in 4 day-old homozygous mutants compared to controls (Fig. 4.5 C-D). Taken together with the cardiac physiology data, *S532P* hearts do not show obvious signs of progressive, pathological DCM remodeling, but do exhibit a dilated phenotype similar to human DCM hearts.

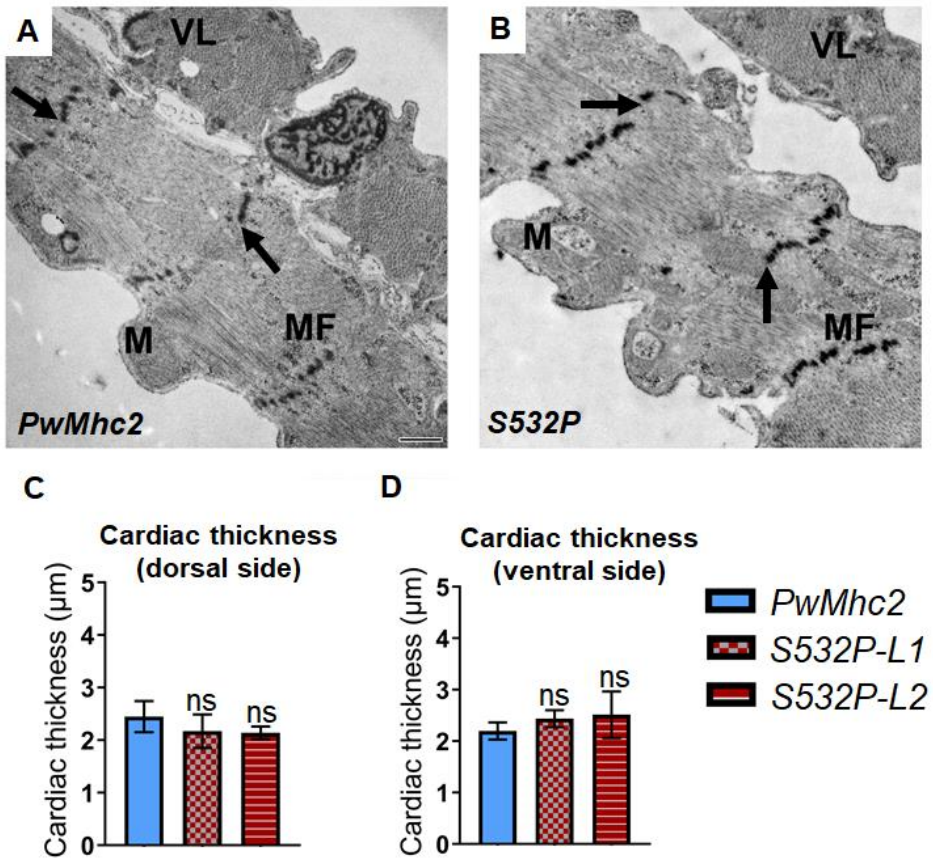

Figure 4.5- Cardiac ultrastructure of *S532P* lines

(A-B) Transmission electron micrographs of hearts of 4 day-old *PwMhc2* control or mutant line *S532P-L1* in a homozygous *Mhc^{1}-null* background. Full genotypes are shown in parenthesis: *S532P* lines (*Mhc^{1}*/*Mhc^{1}* ; *P[S532P]*/*P[S532P]*); *PwMhc2* transgenic controls (*P[PwMhc2]/P[PwMhc2]; Mhc^{1}*/*Mhc^{1}*). Micrographs show transverse sections of the heart tube between the third and fourth sets of ostia. MF-myofibril. M- mitochondrion. VL- supportive ventral-longitudinal fibers. Scale bar, 0.5 µm. **C-D)** Cardiac thickness of dorsal-side **(C)** and ventral-side **(D)** areas of the heart were measured using ImageJ. Values represent mean ± standard deviation. Student's t-tests determined statistical significance compared to controls, where ns= non-significant.

4.4. Discussion

To explore tissue-level alterations in cardiac function and structure induced by the S532P myosin mutation, we crossed non His-tagged genomic mutant lines into the *Mhc*^{1} myosin null background.[98] Cardiac physiological parameters were assessed in *S532P/+* and *S532P/S532P* flies to test the hypothesis that expression of a myosin DCM mutation would lead to cardiac dilation in Drosophila. We predicted that mutant flies would exhibit clinical features of DCM patients, including enlarged diastolic and systolic diameters as well as reduced fractional shortening.[5,10] We also predicted that DCM would arise from cardiac remodeling, similar to disease progression in humans.[102]

Though some physiological properties of S532P flies were unexpected (including elevated contractility and heart rhythm in aged *S532P/+* flies), young 4 day-old *S532P/S532P* and aged 3-week-old *S532P/+* flies did exhibit a dilated phenotype. However, cardiac dilation in *S532P/+* flies did not result from progressive enlargement of diastolic diameters (DD). Controls exhibited an age-associated reduction of DD, while *S532P/+* flies did not, which produced a statistically significant difference in DD between genotypes at 3 weeks of age. Similarly, age-associated reductions in heart chamber dimensions were previously reported in wild-type[100,103] and transgenic non-mutant experimental control flies[104]. Since older flies exhibit altered calcium dynamics[105] and ion channel function[106], we speculate that altered calcium handling plays a role in impaired relaxation with age in controls. Both mutants and controls exhibited progressive narrowing of systolic diameters with age, and no differences were observed between genotypes. The mutational effect on DD in absence of changes in SD resulted in enhanced FS in aged *S532P/+* flies. Young *S532P/+* flies did not exhibit differences in FS compared to controls, suggesting that cardiac dilation in older *S532P/+* flies does not compensate for contractile dysfunction in young flies. The cardiac dilation exhibited by our fly model is also gene dose-dependent, since young 4-day-old *S532P/S532P* flies exhibited larger diastolic diameters

relative to controls, while age-matched *S532P/+* flies did not. Similarly, *S532P/S532P* mice exhibited more severe cardiac dilation compared to *S532P/+* mice.[30] Contractile deficits were reported in isolated mouse α-MyHC S532P cardiomyocytes at an age prior to cardiac dilation, suggesting an association between cardiac dilation and systolic dysfunction in mice.[30] However, systolic dysfunction was absent in our fly model, since aged *S532P/+* or young *S532P/S532P* flies did not exhibit deficits in contractile performance. It is possible that the dilated phenotype allows aged *S532P/+* mutant flies to preserve contractility in response to cell death or other cell stressors induced by the S532P mutation. Since the *P* element transgene is expressed in all muscles, such stressors may affect the heart in a cell autonomous or cell non-autonomous fashion. This may result in overall changes in gene expression that alter calcium handling and heart relaxation in mutants, inhibiting the age-associated reduction in DD.

Contractile dynamics were also altered in aged *S532P/+* flies. An age-associated increase in heart period (i.e. decrease in heart rate) was observed in *PwMhc2/+* controls from ages 4 days to 3 weeks. Similarly, age-associated reductions in heart rate were previously reported in older flies and were linked to impaired relaxation caused by a longer Ca^{2+} decay time[105] or electrophysiological defects.[107] Additionally, altered expression of genes controlling cardiac ion channel function[106], metabolism[82,108], protein synthesis[83], and protein folding[83] may further influence heart rate decline with age. Heart period did not change with age in *S532P/+* flies. Thus, heart period was significantly lower in aged mutant hearts compared to controls, which was associated with reductions in both diastolic and systolic intervals. Since aged mutants exhibit elevated heart rhythmicity and contractility, overall cardiac output is higher in mutants. It is possible that *S532P/+* flies compensate for contractile deficits during development or cell stressors by altering one or more gene expression pathways that inhibit heart rate decline and preserve cardiac output. The systolic interval (i.e. contraction interval) was lower in aged *S532P/+* flies, suggesting that the mutation decreases the duration of the cardiac cycle in which active tension is generated. Since muscle rate apparent constants related to actin binding ($2\pi b$)

and dissociation ($2\pi c$) are respectively increased and decreased in IFMs, we suppose that impaired actomyosin interactions could result in shortened contractions in the heart as well.

We previously reported degeneration of myofibrils in IFMs and hearts of flies expressing hyperactive mutant myosins associated with human restrictive[13] and hypertrophic[12] cardiomyopathy. Excessive cross-bridge binding was proposed to cause hypercontractility and subsequent deterioration of cardiac myofibrils in the latter.[12] In contrast, cardiac ultrastructural is normal in 4-day-old *S532P*/*S532P* flies, suggesting that cardiac physiological abnormalities induced by the hypoactive S532P myosin form are not caused by defects in myofibrillar assembly or maintenance. This is consistent with our data that IFM ultrastructure is normal in *S532P/S532P* flies (chapter 3). Similarly, flies expressing the hypoactive A261T myosin mutation displayed normal IFM ultrastructure despite having reduced muscle function.[59] Cardiomyocyte disarray was also absent in a *S532P/+* patient[5] and in α-MyHC S532P mice.[30] Unlike human DCM, our fly model did not exhibit signs of pathological cardiac remodeling. Given that heart diameters did not get progressively larger with age in *S532P/+* flies, it is unlikely that expression of this mutation results in eccentric hypertrophy (addition of sarcomeres in series).[109] We note that it is not feasible to assess for eccentric hypertrophy in TEM micrographs due to the spiraling nature of the myocytes, which harbor discontinuous Z-disks.[110] In humans, a switch to pathological DCM involves myocyte cell loss and the progressive thinning of cardiac walls.[109] Cardiac thickness did not differ in *S532P/S532P* flies compared to controls, suggesting that cardiac dilation is not associated with a loss of cardiac myofibrils.

Though Drosophila is useful for modeling the effects of myosin mutations on cardiac structure and function, some limitations in our model do exist. Differences in the amino acid backbone between Drosophila MHC and human β-MyHC may influence the biochemical effects of the mutation. However, since the S532P mutation is located in a structurally conserved actin binding region of the motor domain[74,111], we expect some of its effects on cardiac structure and function in Drosophila to be relevant to human disease. Though the molecular mechanisms of

muscle contraction are similar between Drosophila and human hearts, phenotypic outcomes may vary between species due to differences in cardiac morphology and physiology.[97,112,113] In our fly model, non-cell autonomous stressors may affect the heart, since the *P* element transgene is expressed in all muscles. Since human β-MyHC is primarily expressed in the left ventricle, it is probable that the effects of myosin DCM mutations on left ventricular systolic dysfunction in humans are cell autonomous. Human patients exhibit changes in the proportions of α-MyHC and β-MyHC with heart failure[114], while it is not known whether MHC isoform switching occurs in Drosophila hearts. Furthermore, additional gene mutations are thought to influence the phenotypic variation of human DCM patients[10], while our Drosophila model is isogenic. Thus, we expect some differences in the etiology of DCM in humans compared to fly models.

Despite these limitations, Drosophila is useful for determining the mechanistic basis of myosin-induced DCM. There are several advantages of using Drosophila as a model over mice, including their low maintenance costs, short generation time, high fecundity, and the ability to generate a transgenic model more efficiently.[14] Additionally, Drosophila can sustain viability with limited heart function, contrary to mice.[113] Furthermore, the effects of the mutation on cardiac function in homozygous flies can be assessed independently without compensation by wild-type myosin, since the nucleotide change corresponding to the S532P mutation is in a constitutive exon that is expressed in all protein isoforms. Since mice express more than one cardiac isoform[115], it is possible that non-mutant myosin partially compensates for functional defects induced by the mutation in mice. The Drosophila system is also advantageous over *in vitro* cell models due to the ability to perform tissue-level assessments.[12,13] Our novel fly model provides a better understanding of the structural, biochemical, and biophysical properties of mutant DCM myosin (chapters 2 and 3), and its effects on muscle structure and function (chapters 3 and 4). Since DCM patients with myosin mutations can harbor mutations in other genes important for

muscle function[22], Drosophila may provide an efficient screening system to predict which mutation(s) are causative of disease.

The successful generation of models that recapitulate human disease phenotypes may provide insight into effective therapeutic treatments for human patients. In Drosophila, the cardiac physiological response to drug treatment can be readily assessed on semi-intact heart preparations.[12,116] Future directions will exploit our model to screen for pharmacological agents aimed at ameliorating cardiac defects induced by DCM myosin. Treatment with the cardiac specific myosin activating drug omecamtiv mercarbil (OM), which accelerates the P_i release[88,89] and increases the duration of strong actomyosin binding[90], is a promising drug candidate in this regard.

Chapter 4, in full, contains unpublished material coauthored by Trujillo, Adriana S.; Viswanathan, Meera; Cammarato, Anthony R.; Bernstein, Sanford I. The dissertation author was the primary investigator and author of this chapter.

Chapter 5: Determine the importance of a conserved R369 actin binding residue of myosin affiliated with DCM

5.1. Introduction and hypothesis

The goal of this aim is to elucidate the importance of conserved β-MyHC residue that has been mutated in a pediatric DCM patient. This patient exhibited lateral and posterior left ventricular (LV) noncompaction, LV dilation, and contractile deficits.[117] Genetic testing revealed a G→A transition at nucleotide position 1106 of *MYH7*, resulting in an arginine to glutamine substitution. The β-MyHC R369 residue (Fig. 5.1- green*; D. melanogaster* MHC R368) faces the outside of the molecule within a loop near known actin-binding residues (red). Based on the location of the residue, it may directly interact with actin during the contractile cycle or indirectly modulate actin binding by influencing the orientation of actin binding residues. A cryo-EM structure of the actin/tropomyosin/myosin complex incorporating the crystal structure of Dictyostelium myosin-IE[54] revealed that this residue directly interacts with the SD3 region of actin in the rigor state. Molecular dynamics simulations incorporating the actomyosin cryo-EM complex in conjunction with X-ray structures for F-actin and chicken skeletal muscle myosin II predicted that MHC S1 binds actin at the R371 residue, which is homologous to β-MyHC R369.[31] Furthermore, in Dictyostelium myosin II, mutation of the entire loop containing this residue to glycine residues led to weakened actin binding.[118]

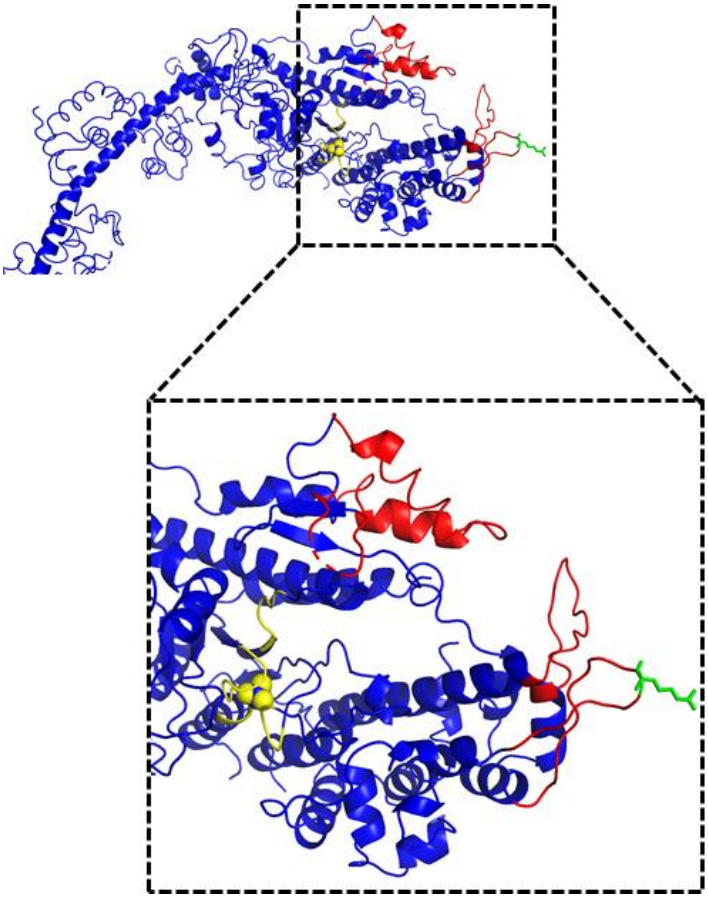

Figure 5.1- The location of the R369 myosin residue within an actin binding region of the motor domain

The β-MyHC R369 residue (green) was modeled on the crystal structure of chicken skeletal muscle myosin II in the post-rigor configuration (PDB ID: 2MYS). Red- actin binding sites. Yellow- ATP binding pocket.

Given that the R369 residue resides within the actin binding region of the motor domain and is predicted to interact directly with actin, we assessed the effects of mutating this residue in the Drosophila system by substituting a histidine residue. This mutation retains the positive charge of the wild-type residue, but introduces a bulky imidazole ring that may sterically hinder an electrostatic interaction with the SD3 region of actin. Thus, we hypothesized that the R369H mutation would disrupt a direct interaction with actin, weaken actin affinity, and reduce myosin function. To test this hypothesis, we generated fly models to determine the importance of the R369 residue interaction with actin.

5.2. Materials and methods

5.2.1. Generation of a mutant His-tagged myosin line and protein purification

We generated a His-tagged line for bulk myosin isolation from IFMs, as described in Section 2.2.1. For this, we utilized a non-mutant pAttB 6HisIFI plasmid previously produced by our lab, which contains the IFM-specific Actin-88F promoter, an amino-terminal His-tag, a tobacco etch virus (TEV) protease recognition site (for removal of the His-tag), cDNA encoding the IFI motor domain, as well as genomic DNA encoding MHC exons 12-19 along with their affiliated introns and polyadenylation sites. The cloning strategy is shown in Fig. 5.2. For the first two steps, subclones containing *Mhc* exon 8 were generated from the larger plasmid. Oligonucleotide-directed mutagenesis was performed (QuikChange kit, Stratagene) to change the codon in Drosophila *Mhc* that corresponds to the *R369H* mutation. The following forward (+) and the reverse (-) primers were used:

(+): 5'-CAAGCAACGTGGTCACGAGGAGCAGGCTG-3'

(-): 5'-CAGCCTGCTCCTCGTGACCACGTTGCTTG-3'

The mutated exon was sequenced for confirmation and inserted into a larger cloning intermediate. The entire construct was removed and ligated into a pAttB vector containing a *miniwhite* (*w*+) selectable eye color marker that restores eye color in a white-eyed genetic background, as well as PhiC31 integrase AttB recognition sites. The final clone was purified using the QIAfilter Plasmid Maxi Kit (Qiagen Inc.) and sequenced for verification by Eton Bioscience. Targeted insertion was performed by Bestgene Inc. using the PhiC31-mediated transgenesis system.[44] One transgenic line containing a third chromosome targeted insert was produced.

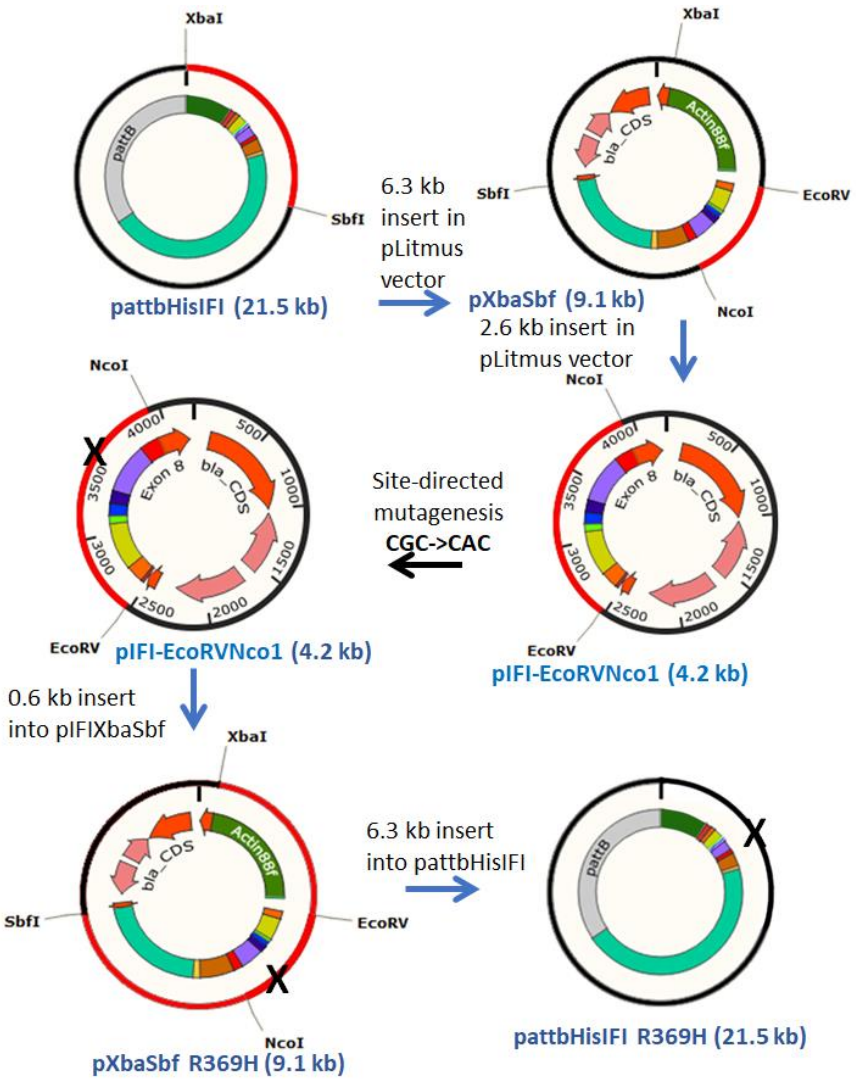

Figure 5.2- Cloning scheme for the 6HisIFI R369H construct
The sequential steps of restriction enzyme (RE) digestion and ligation are shown by the blue arrows. Each insert generated by RE digestion of the parent vector is shown in red, along with RE cut sites. Site-directed mutagenesis (black arrow) was performed to change the encoded arginine residue to a histidine residue at the 368th amino acid coding position of Drosophila *Mhc* (corresponding to position 369 in human *MYH7*). The mutant construct was ligated into a pAttB vector for targeted insertion by Bestgene, Inc using the PhiC31 transgenesis system.

Transgenic flies were crossed into a *Mhc*^{10} background that is null for endogenous myosin in IFMs.[45] Myosin protein levels are expressed at ~80% relative to wild-type *yw* flies in upper thoraces, as determined by SDS-PAGE and densitometry analysis.[46] RT-PCR was performed to verify that the Mhc transcripts produced by this line contain the appropriate nucleotide transition. For this, RNA was isolated from 2 day-old upper thoraces using the RNeasy kit by Qiagen, Inc. The Protoscript cDNA synthesis kit was employed to generate cDNAs, using 500 ng RNA and 100 ng of the specific reverse (-) primer shown below. The following primers were used for PCR amplification:

(+) 5'-TGGATCCCCGACGAGAAGGA-3'

(-) 5'-GTTCGTCACCCAGGGCCGTA-3'

The (-) end directed primer was used to generate cDNAs.

Bulk isolation of His-tagged mutant IFI and subsequent purification of the mutant motor domain was performed as described in Section 2.2.2.

5.2.2. Generation of mutant (non His-tagged) genomic DNA lines

Subclones containing *Mhc* exon 8 were generated from a larger plasmid containing a 19.2 kb *Mhc* 5' fragment (Fig. 5.3). Oligonucleotide-directed mutagenesis was performed (QuikChange kit, Stratagene) to change the codon in Drosophila *Mhc* that corresponds to the *R369H* mutation. The following forward (+) and reverse (-) primers were used for mutagenesis:

(+): 5'-CAAGCAACGTGGTCACGAGGAGCAGGCTG-3'

(-): 5'-CAGCCTGCTCCTCGTGACCACGTTGCTTG-3'

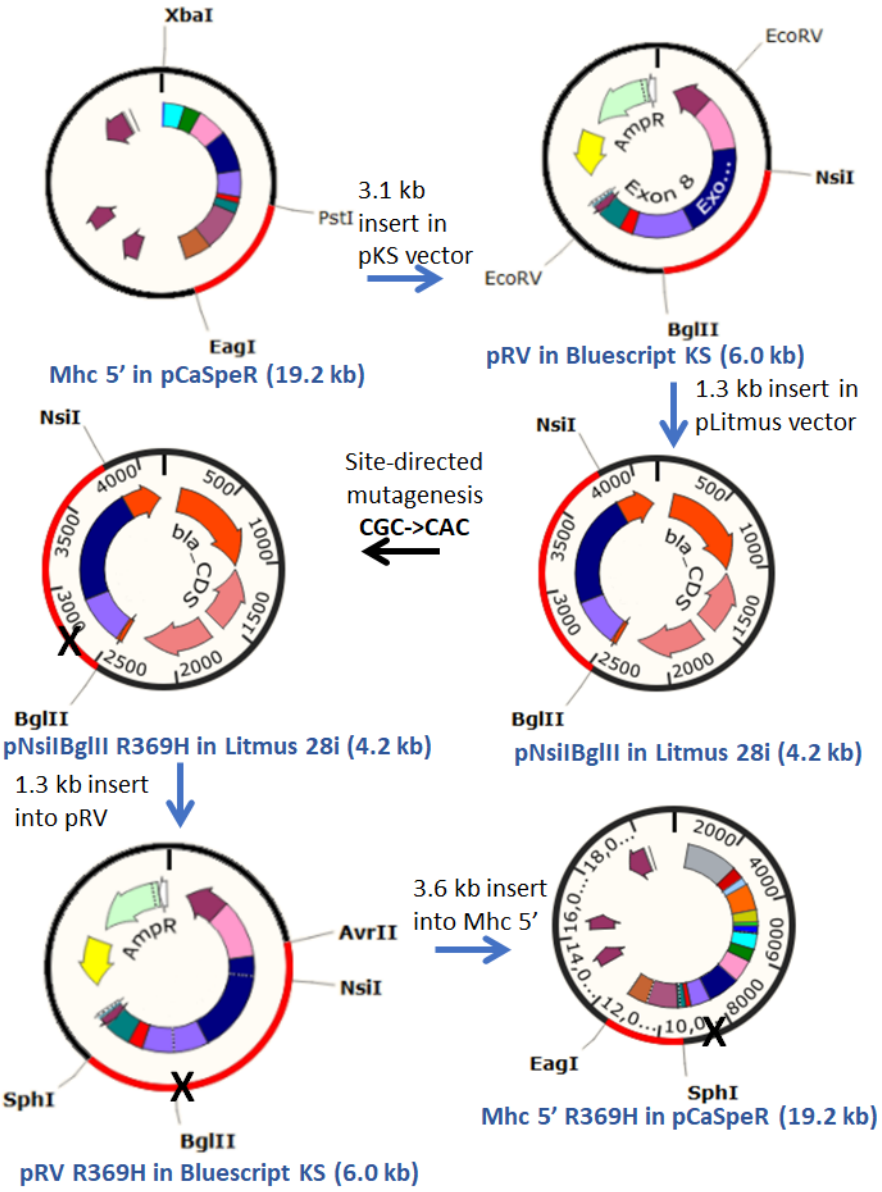

Figure 5.3- Cloning scheme for the non his-tagged Mhc R369H construct, Part I
The sequential steps of restriction enzyme (RE) digestion and ligation are shown by the blue arrows. Each insert generated by RE digestion of the parent vector is shown in red, along with RE cut sites. Site-directed mutagenesis (black arrow) was performed to change the arginine residue to a histidine residue at the 368th amino acid coding position of Drosophila *Mhc* (corresponding to position 369 in human *MYH7*).

The mutated exon was sequenced for confirmation and subclones containing the mutant fragment were inserted into larger cloning intermediates to produce the mutant 5' *Mhc* fragment. For the final cloning step, a 19.2 kb 5' *Mhc* fragment carrying the *R369H* mutation was removed from its vector by EagI digestion, and ligated to a 3' *Mhc* fragment in a pCaSpeR *P* element vector containing the *miniwhite* (w^+) selectable eye color marker (Fig. 5.4). The final clone was purified using the QIAfilter Plasmid Maxi Kit (Qiagen Inc.) and the entire *Mhc* coding region was sequenced for verification by Eton Bioscience.

Embryonic injection was performed by Bestgene, Inc. to incorporate the transgenic insert randomly into the germline via *P* element transformation.[44] A total of 20 transgenic lines were obtained. Several lines mapping to the 3rd chromosome were crossed into the Mhc^{10} myosin-null background. Lines that mapped to the second chromosome were not used since it contains the endogenous *Mhc* gene.

Polyacrylamide gel electrophoresis was performed to determine MHC protein levels in these lines, by comparing the ratio of myosin to actin between transgenic flies and *yw* (wild-type) controls, as described previously.[46] Each lysate consisted of six upper thoraces of 0-2 day-old flies. Only lines with wild-type MHC protein levels were chosen for further experiments.

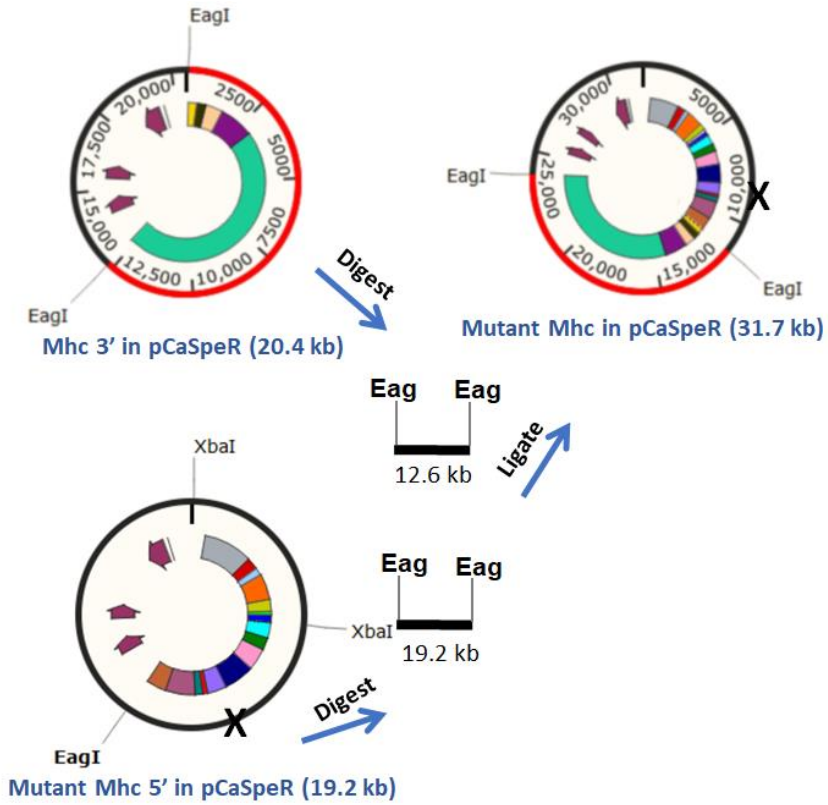

Figure 5.4- Cloning scheme for the non his-tagged Mhc R369H construct, Part II
A 19.2 kb 5' Mhc fragment carrying the R369H mutation was removed from its vector by EagI digestion, and ligated to a Mhc 3' fragment in a pCaSpeR *P* element vector.

RT-PCR confirmed expression of RNA encoding the mutant protein and the absence of endogenous myosin expression in IFMs. Additionally, cDNA was amplified using *Mhc* specific primers to confirm the absence of alternative splicing defects in these lines. RNA isolation, cDNA synthesis, and PCR amplification were performed as described in Section 3.2.2., using the following primer pairs:

Exons 2-8:

(+) 5'-TGGATCCCCGACGAGAAGGA-3'

(-) 5'-GTTCGTCACCCAGGGCCGTA-3'

Exons 8-12:

(+) 5'-TCTGGATACCCAGCAGAAGCGT-3'

(-) 5'-GAGCTTCTTGAAGCCCTTACGG-3'

Exon 15:

(+) 5'-CTCAAGCTCACCCAGGAGGCT-3'

(-) 5'-GGGTGACAGACGCTGCTTGGT-3'

For simplicity, lines *R369H-1*, *R369H-16*, and *R369H-6* were respectively renamed as *R369H-L1*, *R369H-L2*. and *R369H-L3.*

5.2.3. Biochemical assays

The actin co-sedimentation assay was performed as described in Section 3.2.1. The ATPase assay was performed as described in Section 3.2.3.

5.2.4. Organismal tests

Flight and jump tests were performed as described in Section 3.2.5. Transmission electron microscopy of skeletal muscles and cardiac muscles was performed as described in Sections 3.2.6 and 4.2.2. The cardiac physiological analysis was performed as described in Section 4.2.1.

5.3. Results

5.3.1. Actin co-sedimentation

The binding affinity of R369H S1 for F-actin was determined using the co-sedimentation approach. Increasing concentrations F-actin were incubated with a fixed concentration of control or R369H S1. Following high speed centrifugation, S1 remained soluble in S1-only controls, while F-actin was insoluble in F-actin-only controls (Fig. 5.5A). SDS-PAGE gels of centrifuged samples were scanned and densities of S1 bound fractions were fit to a hyperbolic function to determine the B_{max} and dissociation constant (K_d) for F-actin (Fig. 5.5B). R369H S1 exhibited a significantly lower B_{max} value compared to control S1 (0.597 ± 0.085 vs. 1.024 ± 0.211, P= 0.03), indicating reduced maximal binding to F-actin *in vitro*. Values for K_d did not significantly differ for mutants compared to controls (1100 ± 510 nM vs. 1260 ± 963 nM, P= 0.81).

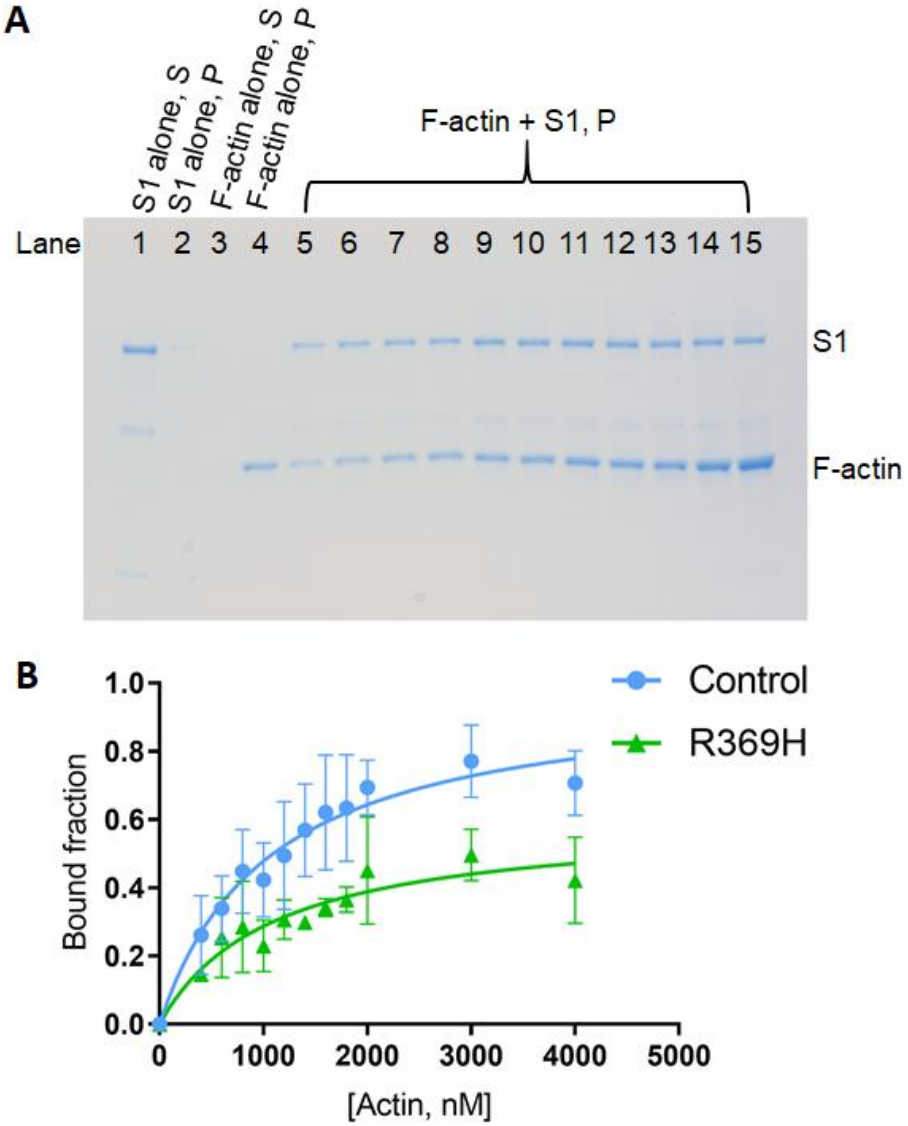

Figure 5.5- Co-sedimentation of R369H IFI S1 and control IFI S1 for F-actin
A) A representative SDS-polyacrylamide gel showing insoluble pellet (P) fractions of F-actin and IFI S1-containing samples over increasing F-actin concentrations (Lanes 5-15: 0.4, 0.6, 0.8, 1, 1.2, 1.4, 1.6, 1.8, 2, 3, and 4 μM). Supernatant (S) and pellet (P) fractions of samples containing S1 or F-actin alone are shown as controls (Lanes 1-4). **B)** The bound fractions in actomyosin-containing samples were determined via densitometry and plotted vs. F-actin concentration. To determine bound fractions, the density of S1 in the pellet fraction relative to total protein content was calculated, and the fraction of pelleted S1 in a S1-only control was subtracted from this value. Data are reported as mean ± SD. To determine actin binding affinity, the dissociation constant of S1 for F-actin (K_d) was defined as the F-actin concentration required to reach half maximal binding (B_{max}).

5.3.2. Fly line validation

To study the biochemical and physiological effects of the R369H mutation, we used *P* element transformation to engineer fly lines harboring the R369H myosin mutation lacking a His-tag. Since lines produced by *P* element transformation can exhibit position effects due to the chromosomal site of insertion, we produced multiple transgenic lines to ensure reproducibility of *in vivo* functional analyses. A total of 20 transgenic lines were obtained. Lines mapping to the third chromosome were crossed into the *Mhc*^{10} genetic background that is null for endogenous myosin in IFMs and jump muscles.[45]

To pursue our study, we selected fly lines with wild-type myosin to actin levels, as determined by SDS-PAGE analysis of upper thoraces of young mutant flies (Table 5.1). RT-PCR of IFM lysates from these lines confirmed expression of RNA encoding mutant myosin, the absence of endogenous myosin expression, and the absence of alternative splicing defects in these lines (Table 5.1).

Table 5.1- Validation of *R369H* fly lines
Protein expression levels in IFMs from *R369H* lines (*L1*, *L2*, and *L3*) relative to wild-type *yw* flies were determined using densitometry. Data are reported as mean ± SEM. RT-PCR of RNA isolated from IFMs was performed to verify that each line expresses transcripts encoding mutant myosin in absence of endogenous myosin, and to verify that alternative exon splicing was not disrupted. ✓ represents verification of the mutation or normal IFI alternative exon.

Genotype	Protein expression	Mutation present	Exon 3b	Exon 7d	Exon 9a	Exon 11e	Exon 15a
R369H-L1	95.3 ± 2.4	✓	✓	✓	✓	✓	✓
R369H-L2	105.4 ± 3.4	✓	✓	✓	✓	✓	✓
R369H-L3	104.6 ± 2.1	✓	✓	✓	✓	✓	✓

5.3.3. ATPase assay

Steady state ATPase parameters of myosins prepared from dissected IFMs were assessed to determine if the R369H mutation affects the enzymatic activity of myosin (Fig. 5.6). Ca-ATPase as well as basal Mg-ATPase activities did not significantly differ between R369H and transgenic wild-type myosin (PwMhc2) myosin. Furthermore, the V_{max} (maximum ATPase

rate) of actin-stimulation, as well as the affinity constant (K_m) of actin required to reach 50% V_{max} did not differ for R369H relative to control myosin.

5.3.4. Flight and jump tests

Mutant lines were tested for flight and jump muscle function compared to *PwMhc2* (*P* element-transformed wild-type) controls to determine if the R369H mutation causes tissue level muscle functional defects (Fig. 5.7). Homozygous mutant lines (*L1-L3*) displayed reduced flight ability compared to controls at ages 2-days [arbitrary units (A.U.) ± S.E.M: 2.72 ± 0.21, 1.14 ± 0.14, and 0.52 ± 0.09 vs. 3.70 ± 0.15 A.U.], 1-week (2.30 ± 0.22, 0.82 ± 0.09, and 0.32 ± 0.07 vs. 3.52 ± 0.12 A.U.), and 3-weeks (0.90 ± 0.14, 0.42 ± 0.08, and 0.22 ± 0.06 vs. 3.32 ± 0.13 A.U.) (Fig. 5.7A). Two-way ANOVAs determined that the effects of genotype ($p<0.0001$) and age ($p<0.0001$) as two independent factors, as well as the interaction between age and genotype ($p<0.0001$), contribute to statistically significant differences between groups. Thus, the R369H mutation causes defects in flight ability that are progressive with age. We also assessed heterozygotes to determine if the R369H mutation causes dominant defects in muscle function. Heterozygous lines (*L1-L3*) display significant reductions in flight ability compared to controls at 3 weeks of age (4.35 ± 0.20, 3.48 ± 0.21, and 4.04 ± 0.17 vs. 4.91 ± 0.15 A.U.; $p= 0.0243$, $p<0.0001$, and $p<0.0001$) (Fig. 5.7B), suggesting that the detrimental effects of the mutation on muscle function are dominant.

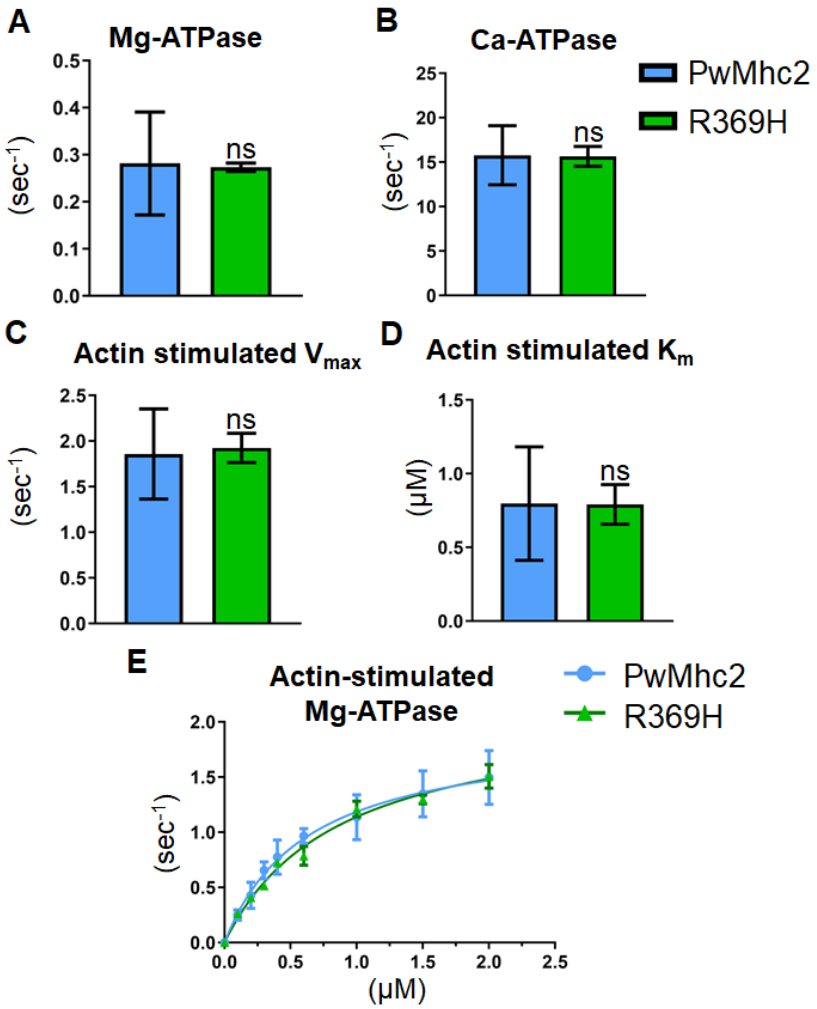

Figure 5.6- ATPase activity of R369H myosin
Full-length myosin isolated from IFMs of *R369H* lines and wild-type transgenic controls (*PwMhc2*) was assessed for the following ATPase parameters: **A)** Basal Mg-ATPase activity, **B)** Ca-ATPase activity, **C)** V_{max} of actin-activated Mg-ATPase, and **D)** actin affinity relative to ATPase (K_m). **E)** To determine actin-activated activity, Mg^{2+} basal ATPase activities were subtracted from measured ATPase values without actin and over increasing concentrations of F-actin. Values were fit with the Michaelis-Menten equation to determine the V_{max} and K_m. Data are reported as mean ± SD. Statistical significance was determined using Student's t-tests (ns= not significant).

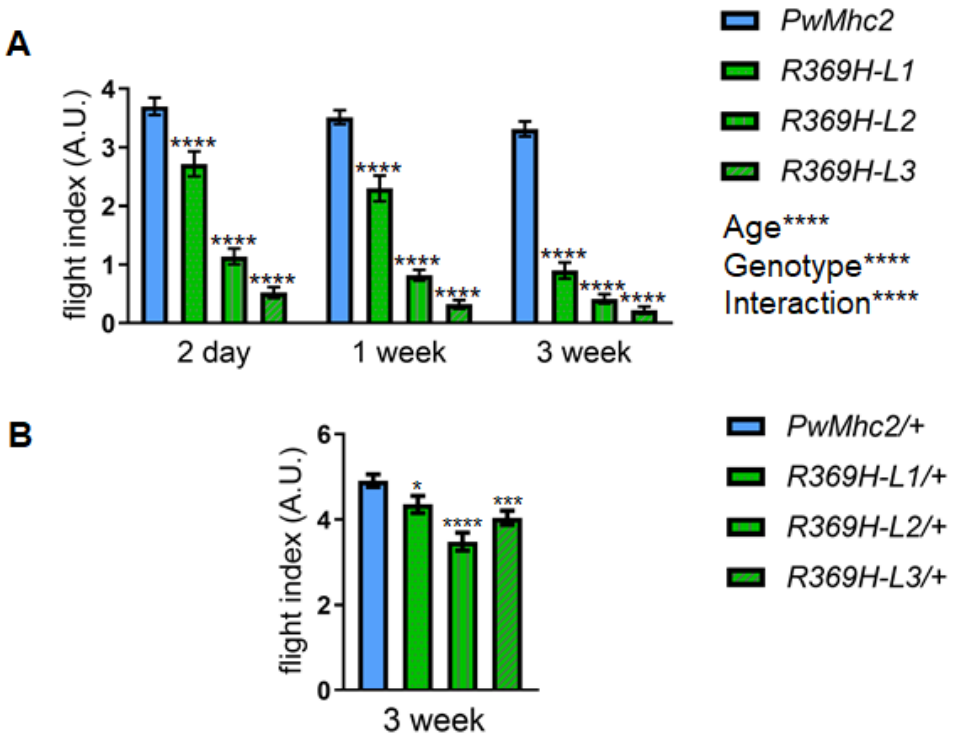

Figure 5.7- Flight abilities of *R369H* mutant lines
Homozygous (**A**) and heterozygous (**B**) *R369H* mutant lines (*L1*, *L2*, and *L3*) were crossed into a Mhc^{10} (myosin-null in IFMs and jump muscles) or Mhc^{10}/+ background, respectively. Flight index was calculated as 6*U/(# flies) +4*H/(# flies) +2*D/(# flies) +0*N/(# flies) where each fly was assigned a score for flight upward (U), horizontally (H), downward (D) or the inability to fly (N). Values represent mean ± S.E.M. A total of N>100 flies were tested for each line/age. **A**) Full genotypes of homozygotes are shown in parenthesis: *R369H* lines (Mhc^{10}/Mhc^{10}; *P[R369H]*/*P[R369H]*); *PwMhc2* transgenic controls (*P[PwMhc2]*/*P[PwMhc2]; Mhc^{10}*/Mhc^{10}). A two-way ANOVA was employed to test if the effects of genotype and age were significant (****p<0.0001). **B)** Full genotypes of heterozygotes are shown in parenthesis, where "-" indicates that no *P* element is present on the homologous chromosome: *R369H*/+ lines (Mhc^{10}/+; *P[R369H]/-*); *PwMhc2/+* transgenic controls (*P[PwMhc2]/-*; Mhc^{10}/+). A one-way ANOVA was employed to determine statistical significance between genotypes (***p<0.001, ****p<0.0001, and ns= non-significant difference compared to controls).

Mean jump distance was also reduced in all three homozygous mutant lines (*L1*, *L2*, and *L3*) compared to controls at ages 2-day (6.09 ± 0.14, 4.58 ± 0.14, and 4.56 ± 0.09 cm vs. 7.08 ± 0.16 cm) and 1-week (6.24 ± 0.12, 5.60 ± 0.12, and 3.97 ± 0.11 cm vs. 7.89 ± 0.14 cm) (Fig. 5.8). Two-way ANOVAs demonstrated significant differences between control and mutant lines ($p<0.0001$), while the effects of age as an independent factor were not statistically significant. Though there was a statistically significant interaction between age and genotype ($p<0.0001$), this could be explained by the increase in jump muscle function observed in controls with age, rather than a deterioration in muscle function with age in mutant lines. Jump muscle function did not worsen from 2-days to 1-week of age in two of the lines tested (*L1* and *L2*), contrary to the progressive and rapid decline in muscle function observed in IFMs.

5.3.5. Transmission electron microscopy of IFMs

Transmission electron microscopy was performed on thin-sectioned IFMs from 3 week-old *R369H* homozygous mutants and controls. Transverse sections of both mutants and controls displayed myofibrils with normal, rounded morphology (Fig. 5.9: A-B), and a normal double hexagonal array of thick and thin filaments (Fig. 5.9: C-D). In longitudinal sections, myofibrils displayed normal parallel organization (Fig. 5.10: A-B), and sarcomeres displayed normal organization with intact myofilaments (Fig. 5.10: C-D). Average inter-thick filament distances (Fig. 5.9E) and sarcomere lengths (Fig. 5.10E) did not differ between mutants and controls. Overall, IFM ultrastructure was not disrupted in *R369H* mutants, suggesting that flight impairment in these lines was not caused by defects in myofibrillar assembly or maintenance.

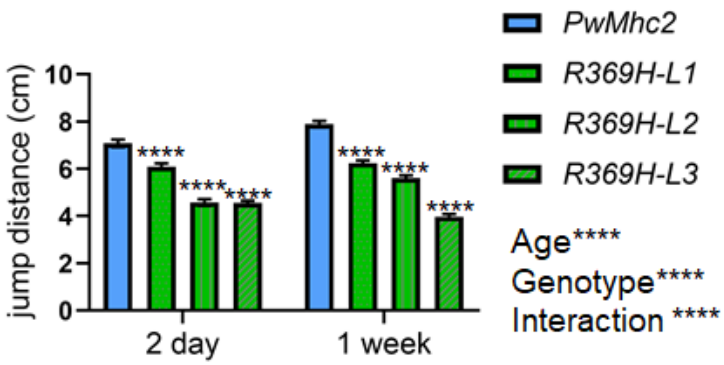

Figure 5.8- Jump abilities of *R369H* mutant lines
Homozygous *R369H* mutant lines (*L1*, *L2*, and *L3*) were crossed into a Mhc^{10} (myosin-null in IFMs and jump muscles) background. The top 3 of 10 jump distances were reported, and a total of N=40 flies were tested per line/age. Full genotypes are shown in parenthesis: *R369H* lines (Mhc^{10}/Mhc^{10}; *P[R369H]*/*P[R369H]*); *PwMhc2* transgenic controls (*P[PwMhc2]/P[PwMhc2]; Mhc^{10}/Mhc^{10}*). Values represent mean ± S.E.M. A two-way ANOVA was employed to test if the effects of genotype and age were significant (****p<0.0001).

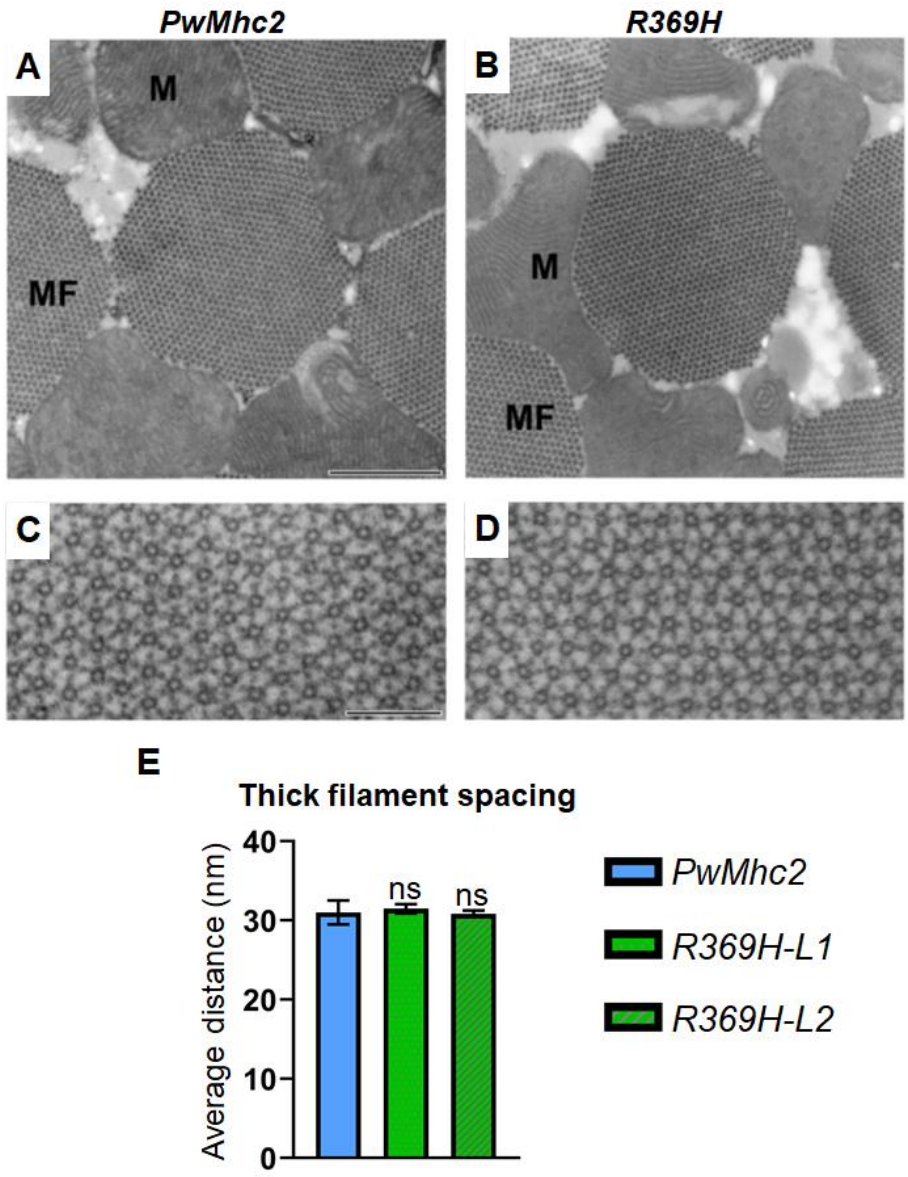

Figure 5.9- Ultrastructure of *R369H* IFMs in transverse orientation
Transmission electron micrographs of thin-sectioned indirect flight muscles (IFMs) in transverse orientation were obtained from 3 week-old homozygous *PwMhc2* control or *R369H* mutant flies in a Mhc^{10} (myosin-null in IFMs and jump muscles) background. Full genotypes are shown in parenthesis: *R369H* lines (Mhc^{10}/Mhc^{10}; *P[R369H]/P[R369H]*); *PwMhc2* transgenic controls (*P[PwMhc2]/P[PwMhc2];* Mhc^{10}/Mhc^{10}). **A-B)** Low magnification images showing myofibrillar morphology. MF- myofibril, M- mitochondrion. Scale bar, 0.5 µm. **C-D)** High magnification images showing hexagonal array of thick and thin filaments. Scale bar, 0.1 µm. **E)** Inter-thick filament spacing averages were determined from micrographs using a custom-written Python script. Values represent mean ± SD. Statistical significance was determined using Student's t-tests (ns= not significant).

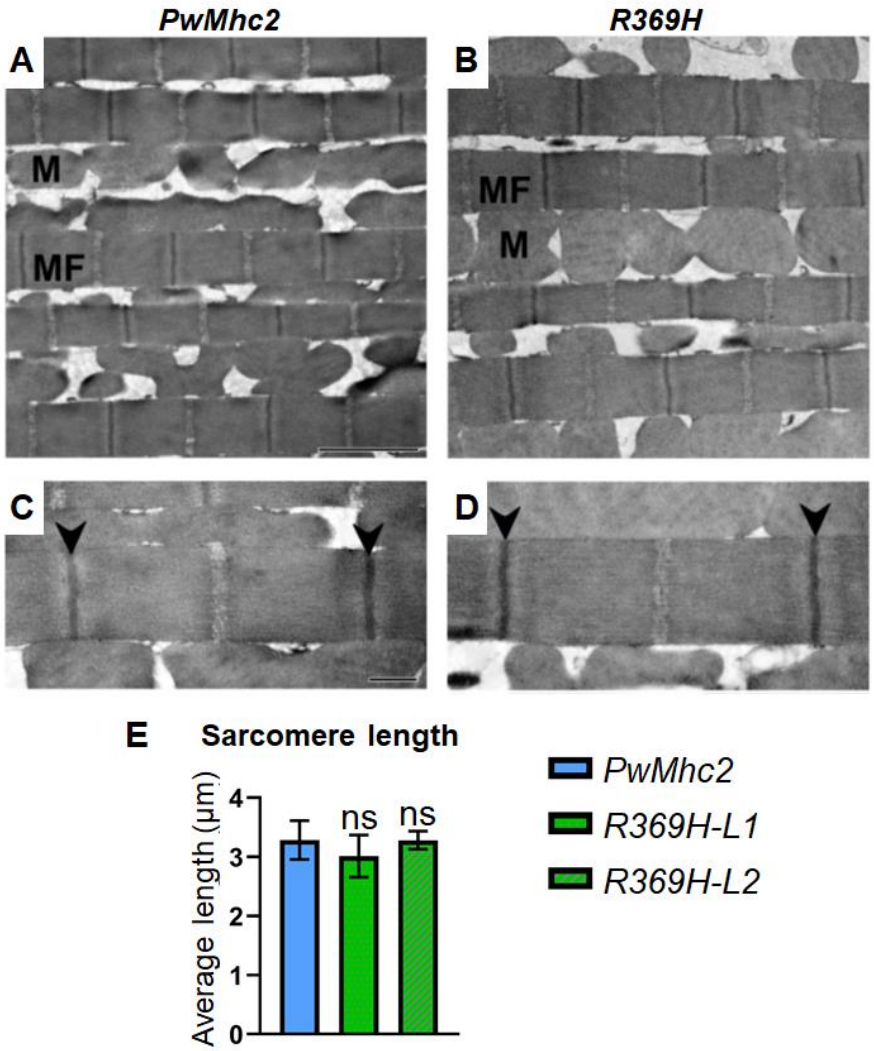

Figure 5.10- Ultrastructure of *R369H* IFMs in longitudinal orientation
Transmission electron micrographs of thin-sectioned indirect flight muscles (IFMs) in longitudinal orientation were obtained from 3 week-old homozygous *PwMhc2* control or *R369H* mutant flies in a Mhc^{10} (myosin-null in IFMs and jump muscles) background. Full genotypes are shown in parenthesis: *R369H* lines (Mhc^{10}/Mhc^{10}; *P[R369H]*/*P[R369H]*); *PwMhc2* transgenic controls (*P[PwMhc2]/P[PwMhc2];* Mhc^{10}/Mhc^{10}). **A-B)** Low magnification images showing myofibrillar organization. MF- myofibril, M- mitochondrion. Scale bar, 2 µm. **C-D)** High magnification images showing sarcomeres bordered by Z-disks (arrowheads). Scale bar, 0.5 µm. **E)** Average sarcomere lengths were determined from micrographs using Image-J software. Values represent mean ± SD. Statistical significance was determined using Student's t-tests, where NS= non-significant difference compared to controls.

5.3.6. Cardiac physiological analysis

To determine the effects of the R369H mutation on cardiac physiology, non His-tagged *Mhc R369H* transgenic flies were crossed into the Mhc^1 myosin null background. Two copies of the *Mhc R369H* transgene rescued lethality of the Mhc^1 homozygotes. Since a majority of homozygotes were not viable beyond the first 4 days of age, only young homozygotes were examined. Aged heterozygotes were viable, permitting the comparison of physiological parameters between young and aged heterozygotes.

Young and aged *R369H/+* flies showed no differences in diastolic (DD) and systolic (SD) diameters, as well as fractional shortening (FS) compared to controls (Fig. 5.11). Control flies displayed an age-associated increase in heart period (HP), which is the length of time required for the completion of a single diastolic and systolic event, from ages 4-days (0.542 ± 0.037 sec) and 3-weeks (Fig. 5.12) (1.392 ± 0.078 sec). Since *R369H/+* lines did not display significant changes in HP with age, the HP durations were significantly lower in 3 week-old mutants relative to controls (0.665 ± 0.045 and 0.595 ± 0.045 sec vs. 1.392 ± 0.078 sec). Durations of DI were also lower relative to controls (0.452 ± 0.039 and 0.401 ± 0.040 sec vs. 1.166 ± 0.075 sec). The effects of genotype ($p<0.0001$), age ($p<0.0001$), and an interaction effect ($p<0.0001$) contribute to differences in HP and DI between groups. Overall, aged *R369H/+* mutants show elevated heart rhythm with no defects in contractility, suggesting that expression of the R369H mutation does not cause dominant reductions in cardiac output.

To determine if expression of two copies of the mutant transgene causes more severe cardiac physiological abnormalities, homozygous *R369H* mutants were crossed into a Mhc^1/Mhc^1 myosin-null background. Both *R369H* homozygous lines tested showed no differences in physiological parameters related to cardiac diameters (i.e. DD, SD, and FS) or contractile dynamics (i.e. HP, DI, and SI) compared to controls (Fig. 5.13).

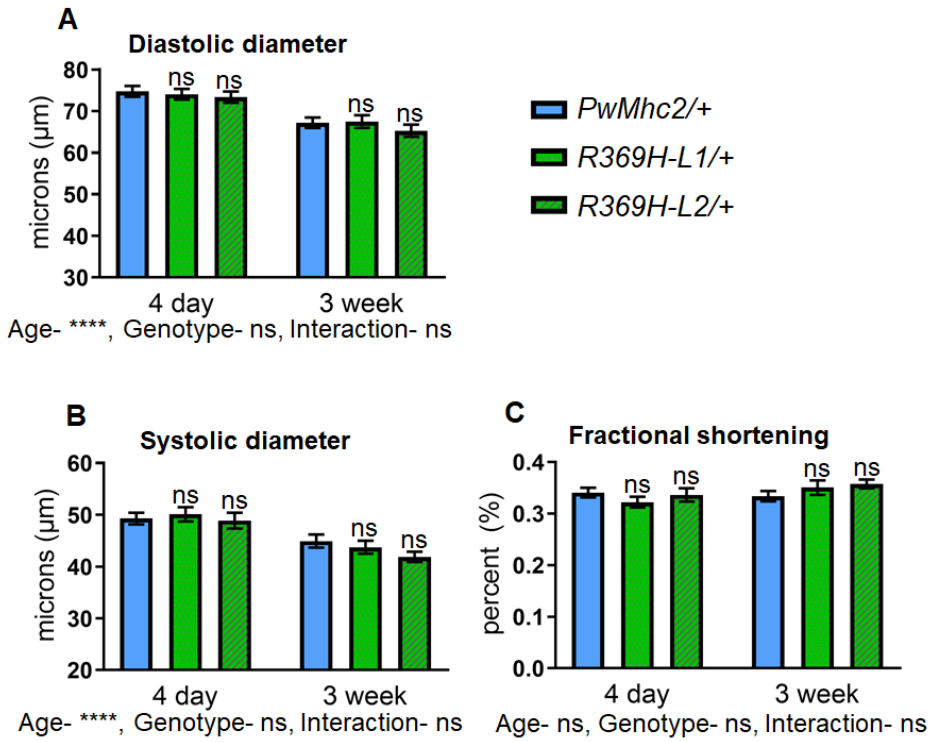

Figure 5.11- Cardiac physiological parameters of *R369H/+* lines, Part I
Cardiac diameters **(A-B)** and fractional shortening **(C)** values of 4 day-old or 3 week-old *PwMhc2* control or mutant *R369H* heterozygous lines (*L1* or *L2*) crossed into a heterozygous *Mhc^{1}-null* background. Full genotypes are shown in parenthesis, where "-" indicates there is no *P* element on the homologous chromosome: *R369H*/+ lines (*Mhc^{1}*/+; *P[R369H]/-*); *PwMhc2/+* transgenic controls (*P[PwMhc2]/-*; *Mhc^{1}*/+). Values represent mean ± S.E.M. Two-way ANOVAs were employed to test if the effects of genotype and age were significant for each cardiac parameter investigated (****p<0.0001 and ns= non-significant).

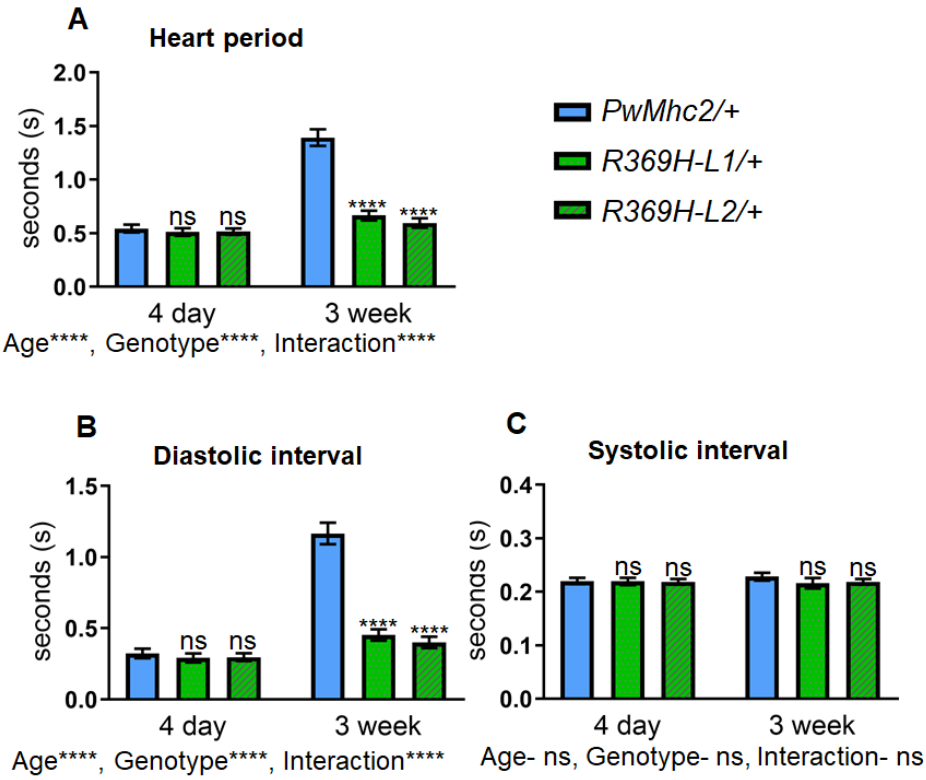

Figure 5.12- Cardiac physiological parameters of *R369H/+* lines, Part II
Heart period **(A)**, diastolic interval **(B)**, and systolic interval **(C)** of 4 day-old or 3 week-old *PwMhc2* control or mutant *R369H* heterozygous lines (*L1* or *L2*) crossed into a heterozygous *Mhc^{1}-null* background. Full genotypes are shown in parenthesis, where "-" indicates there is no *P* element on the homologous chromosome: *R369H*/+ lines (*Mhc^{1}*/+; *P[R369H]*/-); *PwMhc2*/+ transgenic controls (*P[PwMhc2]*/-; *Mhc^{1}*/+). Values represent mean ± S.E.M. Two-way ANOVAs were employed to test if the effects of genotype and age were significant for each cardiac parameter investigated (****p<0.0001 and ns= non-significant).

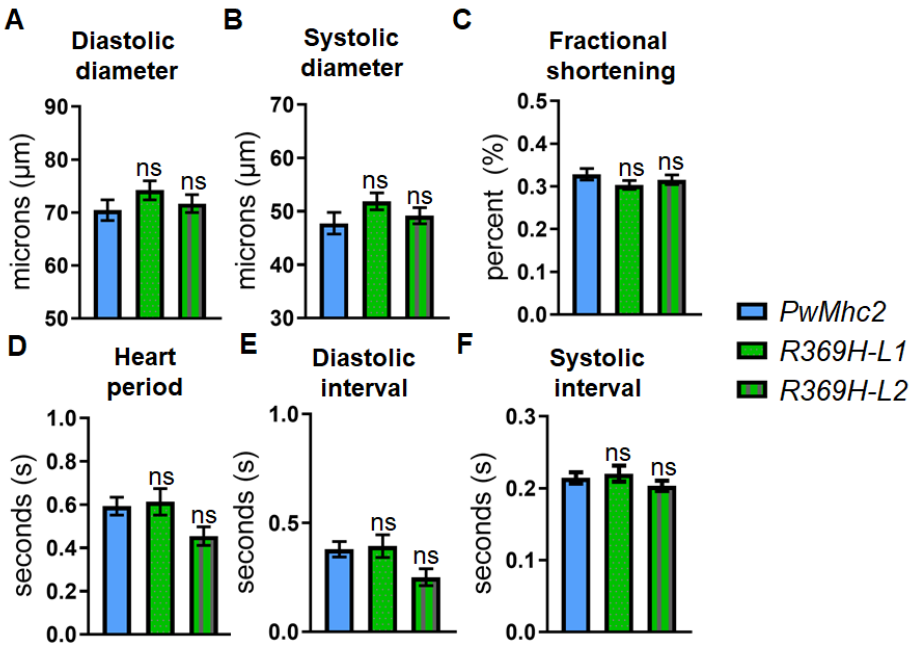

Figure 5.13- Cardiac physiological parameters of *R369H/R369H* lines
Cardiac dimensions **(A-B)**, fractional shortening **(C)**, and dynamics **(D-F)** of 4 day-old *PwMhc2* control or mutant *R369H* homozygous lines (*L1* or *L2*) crossed into a homozygous Mhc^{1}*-null* background. Full genotypes are shown in parenthesis: *R369H* lines (Mhc^{1}/Mhc^{1}; *P[R369H]/P[R369H]*); *PwMhc2* transgenic controls (*P[PwMhc2]/P[PwMhc2];* Mhc^{1}/Mhc^{1}). Values represent mean ± S.E.M. One-way ANOVAs determined statistical significance compared to controls, where ns= non-significant.

5.3.7. Cardiac ultrastructural analysis

Transmission electron microscopy (TEM) was performed to determine if the R369H mutation affects cardiac ultrastructure. For both genotypes, myofibrils are oriented in a circumferential array around the heart tube and contain discontinuous Z-disks (Fig. 5.14: A-B, arrows), as standardly observed in this tissue.[12,13,99-101] Mean cardiac thickness values on the dorsal-side and ventral-side do not differ in 4 day-old homozygous mutants compared to controls (Fig. 5.14: C-D). Overall, myofibrillar ultrastructural properties of cardiomyocytes are similar between 4 day-old *R369H* homozygous mutants and controls, suggesting that both myofibrillar assembly and maintenance are unaffected by the mutation.

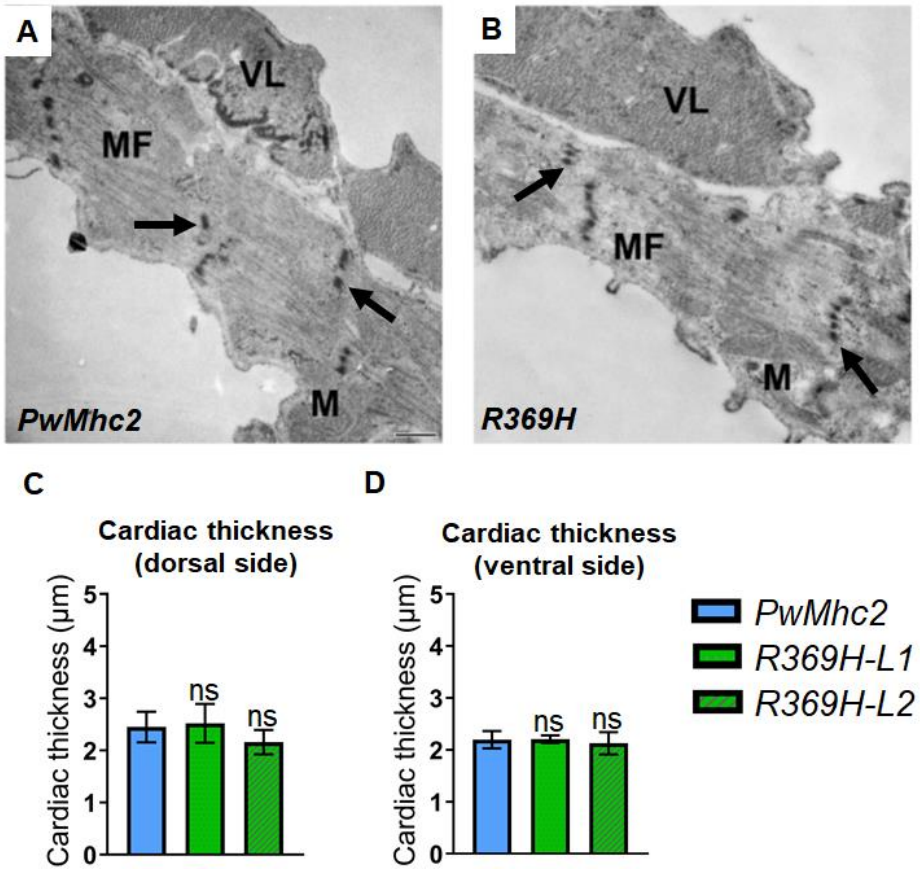

Figure 5.14- Cardiac ultrastructure of *R369H* lines

(A-B) Transmission electron micrographs of hearts of 4 day-old *PwMhc2* control or mutant line *R369H-L2* in a homozygous *Mhc^{1}-null* background. Micrographs show transverse sections of the heart tube between the third and fourth sets of ostia. MF-myofibril. M- mitochondrion. VL-supportive ventral-longitudinal fibers. Scale bar, 0.5 µm. **C-D)** Cardiac thickness of dorsal-side **(C)** and ventral-side **(D)** areas of the heart were measured using ImageJ. Values represent mean ± standard deviation. Student's t-tests determined statistical significance compared to controls, where ns= non-significant.

5.4. Discussion

A human DCM patient was shown to have a de novo glutamine substitution at the conserved R369 residue of β-MyHC.[117] This residue is located within loop 4 of myosin, within its upper 50 kDa subdomain.[118,119] Previous cryo-electron microscopy (cryo-EM) work revealed that loop 4 is one of multiple surface loops at the actomyosin interface.[31,32,52] Here we introduced a conservative R369H mutation into muscle myosin in the Drosophila model system to probe the role of loop 4 in regulating myosin function at the biochemical, ultrastructural and physiological levels.

Previous reports support the hypothesis that loop 4 binds actin. Proteolytic cleavage of loop 4 reduced actin affinity >100-fold in bovine β-MyHC.[120] Fluorescence and kinetic measurements revealed that the mutation of loop 4 residues to glycine reduced actin binding in Dictyostelium myosin II.[118] Additionally, the mutation of a loop 4 G362 residue to alanine reduced actin affinity in chicken gizzard smooth muscle heavy meromyosin.[119] An interaction between loop 4 and actin is further supported by cryo-EM work. A molecular dynamics simulation[31] of a cryo-EM structure of actomyosin[52] incorporating the myosin II[25] and myosin V[121] crystal structures revealed that the R371 residue, which is homologous to β-MyHC R369, forms an electrostatic interaction with D311 of actin in the rigor conformation.[31] This model also revealed that myosin R371 forms hydrogen bonds with residues K328 and Q314 of actin. Additionally, a cryo-EM structure of actin-tropomyosin-myosin[55] incorporating the crystal structure of Dictyostelium myosin-IE[54] revealed direct binding of this residue to the SD3 subunit of actin in the rigor conformation.[55] Finally, a cryo-EM structure of skeletal muscle myosin II bound to F-actin also supports a direct interaction between loop 4 and actin under rigor conditions.[50]

Though the R369H mutation does not result in a charge change at that residue, it introduces a bulky imidazole ring which may sterically hinder an electrostatic interaction with

actin. We found that mutant myosin isolated from indirect flight muscles (IFMs) displayed reduced maximal binding to F-actin *in vitro*, suggesting that the R369 residue is important for actin interaction. Consistent with this hypothesis, fluorimetry experiments utilizing turkey gizzard smooth muscle myosin revealed that a mutation of the R370 residue (homologous to β-MyHC R369) to alanine weakened actin affinity.[119]

During the crossbridge cycle, weak binding of myosin to actin triggers conformational changes that promote release of the products of ATP hydrolysis [inorganic phosphate (P_i), followed by ADP].[77] When P_i is released, further intermolecular interactions at the actin interface stabilize a state in which myosin is strongly bound to actin.[50,77,122] These events are coupled with two lever arm movements (powerstroke steps) that induce force generation. We observed no change in ATPase parameters of Drosophila MHC R369H relative to control MHC. Thus, it is possible that the transition from weak to strong actin binding is not disrupted by the mutation. The K_m of actin affinity relative to ATPase is unchanged, consistent with our co-sedimentation data that the actin binding affinity (K_d) does not differ relative to controls. Since the B_{max} of actin co-sedimentation is reduced in the mutant, it is possible that the mutation disrupts interactions important for stabilizing the strong actin binding state(s). In support of this hypothesis, a cryo-EM model of actomyosin incorporating myosin crystal structures showed that loop 4 directly interacts with actin in the strongly-bound rigor state but not when myosin is weakly bound to actin.[50] Future approaches can employ transient kinetics analyses to determine the exact chemomechanical steps affected by the R369H mutation.

Since the R369H mutation reduces maximal actin binding, we hypothesized and that its expression in Drosophila would yield muscle functional deficits. *R369H/+* flies displayed dominant reductions in flight ability at 3 weeks of age. Additionally, progressive defects in flight ability were observed in *R369H/R369H* flies from ages 2-day to 3-weeks. The causes of functional decline with age remain unknown. Ultrastructural properties of IFMs are normal in 3-week-old *R369H/R369H* flies, suggesting that the severe reductions in muscle function at this

age are not caused by structural deterioration of myofibrils. However, age-related changes in gene expression[81-83], protein expression[84], as well as damage to lipids, proteins[85,86], and organelles[85] may play a role in exacerbating muscle functional deficits. Jump distances were also reduced in *R369H/R369H* flies, but did not decline with age. Overall, these data suggest that the R369 actin binding residue is critical for contractile function. In support of our hypothesis, the aforementioned human DCM patient harboring the R369Q mutation exhibited a deficit in fractional shortening (FS).[117]

We assesed cardiac physiological parameters to determine whether *R369H/+* lines exhibit a dilated phenotype and fractional shortening deficit similar to a human DCM patient harboring a mutation at this residue[117]. Though cardiac diameters and FS were normal in *R369H/+* flies, contractile dynamics were altered in aged flies. An age-associated increase in heart period (i.e. decrease in heart rate) was observed in *PwMhc2/+* controls from ages 4 days to 3 weeks. Similarly, age-associated reductions in heart rate were previously reported in older flies and were linked to impaired relaxation caused by a longer Ca^{2+} decay time[105] or electrophysiological defects.[107] It is also possible that altered expression of genes controlling cardiac ion channel function[106], metabolism[82,108], protein synthesis[83], and protein folding[83] may further influence heart rate decline with age. In contrast to controls, heart period did not change with age in *R369H/+* flies. Thus, heart period was significantly lower in aged mutant hearts, which was associated with reduced diastolic intervals. Since contractility was not altered, the enhanced rhythmicity in *R369H/+* flies increased cardiac output. It is possible that *R369H/+* flies compensate for contractile deficits during development or cell stressors by altering one or more gene expression pathways that preserve cardiac output. For *R369H/R369H* homozygous flies at 4 days of age, cardiac physiological and ultrastructural parameters did not differ compared to controls. Aged *R369H/R369H* lines were not viable in the Mhc^{1}/Mhc^{1} myosin-null background, and were thus not examined. Overall, cardiac physiological parameters were mildly affected by the R369H mutation and did not reveal a DCM phenotype. Since the mutation does not

introduce a charge change, it is not surprising that its effects in Drosophila hearts are mild compared to the severe DCM phenotype in a human *R369Q/+* patient. Interestingly, in Drosophila, the effects of the mutation are more severe in skeletal muscles compared to cardiac muscle, which may arise from differences in the amino acid backbone of the myosin isoforms or muscle physiological properties.

In summary, we exploited the Drosophila model system to elucidate the importance of a conserved actin binding residue. We found that a conservative R369H mutation at this residue impairs maximal actin binding and reduces skeletal muscle function. A better understanding of the intermolecular interactions between myosin and actin may yield insight into the mechanistic basis for cardiomyopathies caused by impaired actomyosin binding.

Chapter 5, in full, contains unpublished material coauthored by Trujillo, Adriana S.; Hsu, Karen; Viswanathan, Meera; Cammarato, Anthony R.; Bernstein, Sanford I. The dissertation author was the primary investigator and author of this chapter.

References

1 McNally, E. M., Golbus, J. R. & Puckelwartz, M. J. Genetic mutations and mechanisms in dilated cardiomyopathy. *J Clin Invest* **123**, 19-26, (2013).

2 Seidman, J. G. & Seidman, C. The genetic basis for cardiomyopathy: from mutation identification to mechanistic paradigms. *Cell* **104**, 557-567, (2001).

3 Lodish, H., Berk, A., Zipursky, S. L., Matsudaira, P., Baltimore, D. & Darnell, J. *Molecular Cell Biology*. 4 edn, (W. H. Freeman, 2000).

4 Geeves, M. A. & Holmes, K. C. in *Advan Protein Chem* Vol. 71 (eds M. Squire John & A. D. Parry David) 161-193 (Academic Press, 2005).

5 Kamisago, M., Sharma, S. D., DePalma, S. R., Solomon, S., Sharma, P., McDonough, B., Smoot, L., Mullen, M. P., Woolf, P. K., Wigle, E. D., Seidman, J. G. & Seidman, C. E. Mutations in sarcomere protein genes as a cause of dilated cardiomyopathy. *N Engl J Med* **343**, 1688-1696, (2000).

6 Warshaw, D. The in vitro motility assay: a window into the myosin molecular motor. *News Physiol Sci* **11**, 1-7, (1996).

7 Lymn, R. W. & Taylor, E. W. Mechanism of adenosine triphosphate hydrolysis by actomyosin. *Biochemistry* **10**, 4617-4624, (1971).

8 Ujfalusi, Z., Vera, C. D., Mijailovich, S. M., Svicevic, M., Yu, E. C., Kawana, M., Ruppel, K. M., Spudich, J. A., Geeves, M. A. & Leinwand, L. A. Dilated cardiomyopathy myosin mutants have reduced force-generating capacity. *J Biol Chem* **293**, 9017-9029, (2018).

9 Lakdawala, N. K., Thune, J. J., Colan, S. D., Cirino, A. L., Farrohi, F., Rivero, J., McDonough, B., Sparks, E., Orav, E. J., Seidman, J. G., Seidman, C. E. & Ho, C. Y. Subtle abnormalities in contractile function are an early manifestation of sarcomere mutations in dilated cardiomyopathy. *Circ Cardiovasc Genet* **5**, 503-510, (2012).

10 Richard, P., Villard, E., Charron, P. & Isnard, R. The genetic bases of cardiomyopathies. *J Am Coll Cardiol* **48**, A79-A89, (2006).

11 Lu, Q. W., Wu, X. Y. & Morimoto, S. Inherited cardiomyopathies caused by troponin mutations. *Journal of geriatric cardiology : JGC* **10**, 91-101, (2013).

12 Kronert, W. A., Bell, K. M., Viswanathan, M. C., Melkani, G. C., Trujillo, A. S., Huang, A., Melkani, A., Cammarato, A., Swank, D. M. & Bernstein, S. I. Prolonged cross-bridge binding triggers muscle dysfunction in a Drosophila model of myosin-based hypertrophic cardiomyopathy. *eLife* **7**, e38064, (2018).

13 Achal, M., Trujillo, A. S., Melkani, G. C., Farman, G. P., Ocorr, K., Viswanathan, M. C., Kaushik, G., Newhard, C. S., Glasheen, B. M., Melkani, A., Suggs, J. A., Moore, J. R., Swank, D. M., Bodmer, R., Cammarato, A. & Bernstein, S. I. A restrictive cardiomyopathy mutation in an invariant proline at the myosin head/rod junction

enhances head flexibility and function, yielding muscle defects in Drosophila. *J Mol Biol* **428**, 2446-2461, (2016).

14 Hales, K. G., Korey, C. A., Larracuente, A. M. & Roberts, D. M. Genetics on the fly: a primer on the Drosophila model system. *Genetics* **201**, 815-842, (2015).

15 Reiter, L. T., Potocki, L., Chien, S., Gribskov, M. & Bier, E. A systematic analysis of human disease-associated gene sequences in Drosophila melanogaster. *Genome Res* **11**, 1114-1125, (2001).

16 Pandey, U. B. & Nichols, C. D. Human disease models in Drosophila melanogaster and the role of the fly in therapeutic drug discovery. *Pharmacol Rev* **63**, 411-436, (2011).

17 Bernstein, S. I., Mogami, K., Donady, J. J. & Emerson, C. P., Jr. Drosophila muscle myosin heavy chain encoded by a single gene in a cluster of muscle mutations. *Nature* **302**, 393-397, (1983).

18 Swank, D. M., Wells, L., Kronert, W. A., Morrill, G. E. & Bernstein, S. I. Determining structure/function relationships for sarcomeric myosin heavy chain by genetic and transgenic manipulation of Drosophila. *Microsc Res Tech* **50**, 430-442, (2000).

19 Caldwell, J. T., Melkani, G. C., Huxford, T. & Bernstein, S. I. Transgenic expression and purification of myosin isoforms using the Drosophila melanogaster indirect flight muscle system. *Methods* **56**, 25-32, (2012).

20 Bernstein, S. I., O'Donnell, P. T. & Cripps, R. M. Molecular genetic analysis of muscle development, structure, and function in Drosophila. *Int Rev Cytol* **143**, 63-152, (1993).

21 Bier, E. & Bodmer, R. Drosophila, an emerging model for cardiac disease. *Gene* **342**, 1-11, (2004).

22 Mestroni, L. & Taylor, M. R. Genetics and genetic testing of dilated cardiomyopathy: a new perspective. *Discov Med* **15**, 43-49, (2013).

23 Houdusse, A., Szent-Gyorgyi, A. G. & Cohen, C. Three conformational states of scallop myosin S1. *Proc Natl Acad Sci U S A* **97**, 11238-11243, (2000).

24 Fisher, A. J., Smith, C. A., Thoden, J., Smith, R., Sutoh, K., Holden, H. M. & Rayment, I. X-ray structures of the myosin motor domain of dictyostelium discoideum complexed with MgADP.BeFx and MgADP.AlF4-. *Biochemistry* **34**, 8960-8972, (1995).

25 Rayment, I., Rypniewski, W. R., Schmidt-Base, K., Smith, R., Tomchick, D. R., Benning, M. M., Winkelmann, D. A., Wesenberg, G. & Holden, H. M. Three-dimensional structure of myosin subfragment-1: a molecular motor. *Science* **261**, 50-58, (1993).

26 Craig, R., Greene, L. E. & Eisenberg, E. Structure of the actin-myosin complex in the presence of ATP. *Proc Natl Acad Sci U S A* **82**, 3247-3251, (1985).

27 Volkmann, N., Lui, H., Hazelwood, L., Trybus, K. M., Lowey, S. & Hanein, D. The R403Q myosin mutation implicated in familial hypertrophic cardiomyopathy causes disorder at the actomyosin interface. *PloS one* **2**, e1123, (2007).

28 Volkmann, N., Liu, H., Hazelwood, L., Krementsova, E. B., Lowey, S., Trybus, K. M. & Hanein, D. The structural basis of myosin V processive movement as revealed by electron cryomicroscopy. *Mol Cell* **19**, 595-605, (2005).

29 Volkmann, N., Ouyang, G., Trybus, K. M., DeRosier, D. J., Lowey, S. & Hanein, D. Myosin isoforms show unique conformations in the actin-bound state. *Proc Natl Acad Sci U S A* **100**, 3227-3232, (2003).

30 Schmitt, J. P., Debold, E. P., Ahmad, F., Armstrong, A., Frederico, A., Conner, D. A., Mende, U., Lohse, M. J., Warshaw, D., Seidman, C. E. & Seidman, J. G. Cardiac myosin missense mutations cause dilated cardiomyopathy in mouse models and depress molecular motor function. *Proc Natl Acad Sci U S A* **103**, 14525-14530, (2006).

31 Lorenz, M. & Holmes, K. C. The actin-myosin interface. *Proc Natl Acad Sci U S A* **107**, 12529-12534, (2010).

32 Holmes, K. C., Schroder, R. R., Sweeney, H. L. & Houdusse, A. The structure of the rigor complex and its implications for the power stroke. *Philos Trans R Soc Lond B Biol Sci* **359**, 1819-1828, (2004).

33 Koppole, S., Smith, J. C. & Fischer, S. The structural coupling between ATPase activation and recovery stroke in the myosin II motor. *Structure* **15**, 825-837, (2007).

34 Cowtan, K. Phase problem in X-ray crystallography, and its solution. *eLS* **10**, 1038 (2011).

35 Dessau, M. A. & Modis, Y. Protein crystallization for X-ray crystallography. *J Vis Exp*, (2011).

36 Tang, C. Y. & Yang, Z. Membrane characterization. Ch. 8- Transmission electron microscopy. *Elsevier*, 145-159, (2017).

37 Lyumkis, D. Challenges and opportunities in cryo-EM single-particle analysis. *J Biol Chem* **294**, 5181-5197, (2019).

38 Thompson, R. F., Walker, M., Siebert, C. A., Muench, S. P. & Ranson, N. A. An introduction to sample preparation and imaging by cryo-electron microscopy for structural biology. *Methods* **100**, 3-15, (2016).

39 Merk, A., Bartesaghi, A., Banerjee, S., Falconieri, V., Rao, P., Davis, M. I., Pragani, R., Boxer, M. B., Earl, L. A., Milne, J. L. S. & Subramaniam, S. Breaking cryo-EM resolution barriers to facilitate drug discovery. *Cell* **165**, 1698-1707, (2016).

40 Czarnocki-Cieciura, M. & Nowotny, M. Introduction to high-resolution cryo-electron microscopy. *Postepy biochemii* **62**, 383-394, (2016).

41 von der Ecken, J., Heissler, S. M., Pathan-Chhatbar, S., Manstein, D. J. & Raunser, S. Cryo-EM structure of a human cytoplasmic actomyosin complex at near-atomic resolution. *Nature* **534**, 724-728, (2016).

42 Kronert, W. A., Melkani, G. C., Melkani, A. & Bernstein, S. I. Alternative relay and converter domains tune native muscle myosin isoform function in Drosophila. *J Mol Biol* **416**, 543-557, (2012).

43 Swank, D. M., Bartoo, M. L., Knowles, A. F., Iliffe, C., Bernstein, S. I., Molloy, J. E. & Sparrow, J. C. Alternative exon-encoded regions of Drosophila myosin heavy chain modulate ATPase rates and actin sliding velocity. *J Biol Chem* **276**, 15117-15124, (2001).

44 Bischof, J., Maeda, R. K., Hediger, M., Karch, F. & Basler, K. An optimized transgenesis system for Drosophila using germ-line-specific phiC31 integrases. *Proc Natl Acad Sci U S A* **104**, 3312-3317, (2007).

45 Collier, V. L., Kronert, W. A., O'Donnell, P. T., Edwards, K. A. & Bernstein, S. I. Alternative myosin hinge regions are utilized in a tissue-specific fashion that correlates with muscle contraction speed. *Genes Dev* **4**, 885-895, (1990).

46 Suggs, J. A., Cammarato, A., Kronert, W. A., Nikkhoy, M., Dambacher, C. M., Megighian, A. & Bernstein, S. I. Alternative S2 hinge regions of the myosin rod differentially affect muscle function, myofibril dimensions and myosin tail length. *J Mol Biol* **367**, 1312-1329, (2007).

47 Gilmour, D. Myosin and adenylpyrophosphatase in insect muscle. *J Biol Chem* **175**, 477, (1948).

48 Ludtke, S. J., Baldwin, P. R. & Chiu, W. EMAN: semiautomated software for high-resolution single-particle reconstructions. *J Struct Biol* **128**, 82-97, (1999).

49 Moriya, T., Saur, M., Stabrin, M., Merino, F., Voicu, H., Huang, Z., Penczek, P. A., Raunser, S. & Gatsogiannis, C. High-resolution single particle analysis from electron cryo-microscopy images using SPHIRE. *J Vis Exp* **123**, 55448, (2017).

50 Fujii, T. & Namba, K. Structure of actomyosin rigour complex at 5.2 Å resolution and insights into the ATPase cycle mechanism. *Nat Commun* **8**, 13969, (2017).

51 Scheres, S. H. RELION: implementation of a Bayesian approach to cryo-EM structure determination. *J Struct Biol* **180**, 519-530, (2012).

52 Holmes, K. C., Angert, I., Kull, F. J., Jahn, W. & Schroder, R. R. Electron cryo-microscopy shows how strong binding of myosin to actin releases nucleotide. *Nature* **425**, 423-427, (2003).

53 Sweeney, H. L. & Houdusse, A. Structural and functional insights into the myosin motor mechanism. *Annual review of biophysics* **39**, 539-557, (2010).

54 Kollmar, M., Dürrwang, U., Kliche, W., Manstein, D. J. & Kull, F. J. Crystal structure of the motor domain of a class-I myosin. *EMBO J* **21**, 2517-2525, (2002).

55 Behrmann, E., Muller, M., Penczek, P. A., Mannherz, H. G., Manstein, D. J. & Raunser, S. Structure of the rigor actin-tropomyosin-myosin complex. *Cell* **150**, 327-338, (2012).

56 Alias, M., Ayuso-Tejedor, S., Fernandez-Recio, J., Cativiela, C. & Sancho, J. Helix propensities of conformationally restricted amino acids. Non-natural substitutes for helix breaking proline and helix forming alanine. *Organic & biomolecular chemistry* **8**, 788-792, (2010).

57 Geeves, M. A. The dynamics of actin and myosin association and the crossbridge model of muscle contraction. *Biochem J* **274 (Pt 1)**, 1-14, (1991).

58 Stein, L. A., Chock, P. B. & Eisenberg, E. Mechanism of the actomyosin ATPase: effect of actin on the ATP hydrolysis step. *Proc Natl Acad Sci U S A* **78**, 1346-1350, (1981).

59 Cammarato, A., Dambacher, C. M., Knowles, A. F., Kronert, W. A., Bodmer, R., Ocorr, K. & Bernstein, S. I. Myosin transducer mutations differentially affect motor function, myofibril structure, and the performance of skeletal and cardiac muscles. *Molecular biology of the cell* **19**, 553-562, (2008).

60 Reubold, T. F., Eschenburg, S., Becker, A., Kull, F. J. & Manstein, D. J. A structural model for actin-induced nucleotide release in myosin. *Nature structural biology* **10**, 826-830, (2003).

61 Wang, Y., Melkani, G. C., Suggs, J. A., Melkani, A., Kronert, W. A., Cammarato, A. & Bernstein, S. I. Expression of the inclusion body myopathy 3 mutation in Drosophila depresses myosin function and stability and recapitulates muscle inclusions and weakness. *Molecular biology of the cell* **23**, 2057-2065, (2012).

62 Rao, D. S., Kronert, W. A., Guo, Y., Hsu, K. H., Sarsoza, F. & Bernstein, S. I. Reductions in ATPase activity, actin sliding velocity, and myofibril stability yield muscle dysfunction in Drosophila models of myosin-based Freeman-Sheldon syndrome. *Molecular biology of the cell* **30**, 30-41, (2019).

63 Viswanathan, M. C., Tham, R. C., Kronert, W. A., Sarsoza, F., Trujillo, A. S., Cammarato, A. & Bernstein, S. I. Myosin storage myopathy mutations yield defective myosin filament assembly in vitro and disrupted myofibrillar structure and function in vivo. *Human molecular genetics* **26**, 4799-4813, (2017).

64 Bell, K. M., Kronert, W. A., Huang, A., Bernstein, S. I. & Swank, D. M. The R249Q hypertrophic cardiomyopathy myosin mutation decreases contractility in Drosophila by impeding force production. *J Physiol* **597**, 2403-2420, (2019).

65 Drummond, D. R., Hennessey, E. S. & Sparrow, J. C. Characterisation of missense mutations in the Act88F gene of Drosophila melanogaster. *Mol Gen Genet* **226**, 70-80, (1991).

66 Swank, D. M. Mechanical analysis of Drosophila indirect flight and jump muscles. *Methods* **56**, 69-77, (2012).

67 Palmer, B. M., Schmitt, J. P., Seidman, C. E., Seidman, J. G., Wang, Y., Bell, S. P., Lewinter, M. M. & Maughan, D. W. Elevated rates of force development and MgATP binding in F764L and S532P myosin mutations causing dilated cardiomyopathy. *J Mol Cell Cardiol* **57**, 23-31, (2013).

68 Taft, M. H., Behrmann, E., Munske-Weidemann, L. C., Thiel, C., Raunser, S. & Manstein, D. J. Functional characterization of human myosin-18A and its interaction with F-actin and GOLPH3. *J Biol Chem* **288**, 30029-30041, (2013).

69 Dose, A. C., Ananthanarayanan, S., Moore, J. E., Burnside, B. & Yengo, C. M. Kinetic mechanism of human myosin IIIA. *J Biol Chem* **282**, 216-231, (2007).

70 Price, M. G., Landsverk, M. L., Barral, J. M. & Epstein, H. F. Two mammalian UNC-45 isoforms are related to distinct cytoskeletal and muscle-specific functions. *J Cell Sci* **115**, 4013-4023, (2002).

71 Kawai, M. & Brandt, P. W. Sinusoidal analysis: a high resolution method for correlating biochemical reactions with physiological processes in activated skeletal muscles of rabbit, frog and crayfish. *J Muscle Res Cell Motil* **1**, 279-303, (1980).

72 Swank, D. M., Vishnudas, V. K. & Maughan, D. W. An exceptionally fast actomyosin reaction powers insect flight muscle. *Proc Natl Acad Sci U S A* **103**, 17543-17547, (2006).

73 Mulieri, L. A., Barnes, W., Leavitt, B. J., Ittleman, F. P., LeWinter, M. M., Alpert, N. R. & Maughan, D. W. Alterations of myocardial dynamic stiffness implicating abnormal crossbridge function in human mitral regurgitation heart failure. *Circ Res* **90**, 66-72, (2002).

74 Aksel, T., Choe Yu, E., Sutton, S., Ruppel, K. M. & Spudich, J. A. Ensemble force changes that result from human cardiac myosin mutations and a small-molecule effector. *Cell Rep* **11**, 910-920, (2015).

75 Spudich, J. A. Hypertrophic and dilated cardiomyopathy: four decades of basic research on muscle lead to potential therapeutic approaches to these devastating genetic diseases. *Biophys J* **106**, 1236-1249, (2014).

76 Kronert, W. A., Melkani, G. C., Melkani, A. & Bernstein, S. I. A failure to communicate: myosin residues involved in hypertrophic cardiomyopathy affect inter-domain interaction. *J Biol Chem* **290**, 29270-29280, (2015).

77 Houdusse, A. & Sweeney, H. L. How myosin generates force on actin filaments. *Trends Biochem Sci* **41**, 989-997, (2016).

78 Muretta, J. M., Petersen, K. J. & Thomas, D. D. Direct real-time detection of the actin-activated power stroke within the myosin catalytic domain. *Proc Natl Acad Sci U S A* **110**, 7211-7216, (2013).

79 Onishi, H., Mikhailenko, S. V. & Morales, M. F. Toward understanding actin activation of myosin ATPase: the role of myosin surface loops. *Proc Natl Acad Sci U S A* **103**, 6136-6141, (2006).

80 Debold, E. P., Schmitt, J. P., Patlak, J. B., Beck, S. E., Moore, J. R., Seidman, J. G., Seidman, C. & Warshaw, D. M. Hypertrophic and dilated cardiomyopathy mutations differentially affect the molecular force generation of mouse alpha-cardiac myosin in the laser trap assay. *Am J Physiol Heart Circ Physiol* **293**, H284-291, (2007).

81 Zahn, J. M., Sonu, R., Vogel, H., Crane, E., Mazan-Mamczarz, K., Rabkin, R., Davis, R. W., Becker, K. G., Owen, A. B. & Kim, S. K. Transcriptional profiling of aging in human muscle reveals a common aging signature. *PLoS genetics* **2**, e115, (2006).

82 Carlson, K. A., Gardner, K., Pashaj, A., Carlson, D. J., Yu, F., Eudy, J. D., Zhang, C. & Harshman, L. G. Genome-wide gene expression in relation to age in large laboratory cohorts of Drosophila melanogaster. *Genet Res Int* **2015**, 835624, (2015).

83 Landis, G. N., Abdueva, D., Skvortsov, D., Yang, J., Rabin, B. E., Carrick, J., Tavare, S. & Tower, J. Similar gene expression patterns characterize aging and oxidative stress in Drosophila melanogaster. *Proc Natl Acad Sci U S A* **101**, 7663-7668, (2004).

84 Fleming, J. E., Quattrocki, E., Latter, G., Miquel, J., Marcuson, R., Zuckerkandl, E. & Bensch, K. G. Age-dependent changes in proteins of Drosophila melanogaster. *Science* **231**, 1157-1159, (1986).

85 Miller, M. S., Lekkas, P., Braddock, J. M., Farman, G. P., Ballif, B. A., Irving, T. C., Maughan, D. W. & Vigoreaux, J. O. Aging enhances indirect flight muscle fiber performance yet decreases flight ability in Drosophila. *Biophys J* **95**, 2391-2401, (2008).

86 Das, N., Levine, R. L., Orr, W. C. & Sohal, R. S. Selectivity of protein oxidative damage during aging in Drosophila melanogaster. *Biochem J* **360**, 209-216, (2001).

87 Bloemink, M. J., Melkani, G. C., Dambacher, C. M., Bernstein, S. I. & Geeves, M. A. Two Drosophila myosin transducer mutants with distinct cardiomyopathies have divergent ADP and actin affinities. *J Biol Chem* **286**, 28435-28443, (2011).

88 Liu, Y., White, H. D., Belknap, B., Winkelmann, D. A. & Forgacs, E. Omecamtiv Mecarbil modulates the kinetic and motile properties of porcine beta-cardiac myosin. *Biochemistry* **54**, 1963-1975, (2015).

89 Winkelmann, D. A., Forgacs, E., Miller, M. T. & Stock, A. M. Structural basis for drug-induced allosteric changes to human beta-cardiac myosin motor activity. *Nat Commun* **6**, 7974, (2015).

90 Malik, F. I., Hartman, J. J., Elias, K. A., Morgan, B. P., Rodriguez, H., Brejc, K., Anderson, R. L., Sueoka, S. H., Lee, K. H., Finer, J. T., Sakowicz, R., Baliga, R., Cox, D. R., Garard, M., Godinez, G., Kawas, R., Kraynack, E., Lenzi, D., Lu, P. P., Muci, A., Niu, C., Qian, X., Pierce, D. W., Pokrovskii, M., Suehiro, I., Sylvester, S., Tochimoto, T., Valdez, C., Wang, W., Katori, T., Kass, D. A., Shen, Y. T., Vatner, S. F. & Morgans, D. J. Cardiac myosin activation: a potential therapeutic approach for systolic heart failure. *Science* **331**, 1439-1443, (2011).

91 Kaplinsky, E. & Mallarkey, G. Cardiac myosin activators for heart failure therapy: focus on omecamtiv mecarbil. *Drugs Context* **7**, 212518, (2018).

92 Teerlink, J. R., Felker, G. M., McMurray, J. J., Solomon, S. D., Adams, K. F., Jr., Cleland, J. G., Ezekowitz, J. A., Goudev, A., Macdonald, P., Metra, M., Mitrovic, V., Ponikowski, P., Serpytis, P., Spinar, J., Tomcsanyi, J., Vandekerckhove, H. J., Voors, A. A., Monsalvo, M. L., Johnston, J., Malik, F. I. & Honarpour, N. Chronic oral study of

myosin activation to increase contractility in heart failure (COSMIC-HF): a phase 2, pharmacokinetic, randomised, placebo-controlled trial. *Lancet* **388**, 2895-2903, (2016).

93 Wasserthal, L. T. Drosophila flies combine periodic heartbeat reversal with a circulation in the anterior body mediated by a newly discovered anterior pair of ostial valves and 'venous' channels. *J Exp Biol* **210**, 3707-3719, (2007).

94 Xie, M., Burchfield, J. S. & Hill, J. A. Pathological ventricular remodeling. *Circulation* **128**, 1021-1030, (2013).

95 Holubarsch, C., Ruf, T., Goldstein, D. J., Ashton, R. C., Nickl, W., Pieske, B., Pioch, K., Ludemann, J., Wiesner, S., Hasenfuss, G., Posival, H., Just, H. & Burkhoff, D. Existence of the Frank-Starling mechanism in the failing human heart. Investigations on the organ, tissue, and sarcomere levels. *Circulation* **94**, 683-689, (1996).

96 Ocorr, K., Vogler, G. & Bodmer, R. Methods to assess Drosophila heart development, function and aging. *Methods* **68**, 265-272, (2014).

97 Ocorr, K., Perrin, L., Lim, H. Y., Qian, L., Wu, X. & Bodmer, R. Genetic control of heart function and aging in Drosophila. *Trends Cardiovasc Med* **17**, 177-182, (2007).

98 O'Donnell, P. T. & Bernstein, S. I. Molecular and ultrastructural defects in a Drosophila myosin heavy chain mutant: differential effects on muscle function produced by similar thick filament abnormalities. *J Cell Biol* **107**, 2601-2612, (1988).

99 Bhide, S., Trujillo, A. S., O'Connor, M. T., Young, G. H., Cryderman, D. E., Chandran, S., Nikravesh, M., Wallrath, L. L. & Melkani, G. C. Increasing autophagy and blocking Nrf2 suppress laminopathy-induced age-dependent cardiac dysfunction and shortened lifespan. *Aging cell* **17**, e12747, (2018).

100 Kaushik, G., Spenlehauer, A., Sessions, A. O., Trujillo, A. S., Fuhrmann, A., Fu, Z., Venkatraman, V., Pohl, D., Tuler, J., Wang, M., Lakatta, E. G., Ocorr, K., Bodmer, R., Bernstein, S. I., Van Eyk, J. E., Cammarato, A. & Engler, A. J. Vinculin network-mediated cytoskeletal remodeling regulates contractile function in the aging heart. *Sci Transl Med* **7**, 292ra299, (2015).

101 Melkani, G. C., Trujillo, A. S., Ramos, R., Bodmer, R., Bernstein, S. I. & Ocorr, K. Huntington's disease induced cardiac amyloidosis is reversed by modulating protein folding and oxidative stress pathways in the Drosophila heart. *PLoS genetics* **9**, e1004024, (2013).

102 Schultheiss, H. P., Fairweather, D., Caforio, A. L. P., Escher, F., Hershberger, R. E., Lipshultz, S. E., Liu, P. P., Matsumori, A., Mazzanti, A., McMurray, J. & Priori, S. G. Dilated cardiomyopathy. *Nat Rev Dis Primers* **5**, 32, (2019).

103 Fink, M., Callol-Massot, C., Chu, A., Ruiz-Lozano, P., Izpisua Belmonte, J. C., Giles, W., Bodmer, R. & Ocorr, K. A new method for detection and quantification of heartbeat parameters in Drosophila, zebrafish, and embryonic mouse hearts. *Biotechniques* **46**, 101-113, (2009).

104 Chang, K., Kang, P., Liu, Y., Huang, K., Miao, T., Sagona, A. P., Nezis, I. P., Bodmer, R., Ocorr, K. & Bai, H. TGFB-INHB/activin signaling regulates age-dependent autophagy and cardiac health through inhibition of MTORC2. *Autophagy*, 1-16, (2019).

105 Santalla, M., Valverde, C. A., Harnichar, E., Lacunza, E., Aguilar-Fuentes, J., Mattiazzi, A. & Ferrero, P. Aging and CaMKII alter intracellular Ca2+ transients and heart rhythm in Drosophila melanogaster. *PloS one* **9**, e101871, (2014).

106 Ocorr, K., Reeves, N. L., Wessells, R. J., Fink, M., Chen, H. S., Akasaka, T., Yasuda, S., Metzger, J. M., Giles, W., Posakony, J. W. & Bodmer, R. KCNQ potassium channel mutations cause cardiac arrhythmias in Drosophila that mimic the effects of aging. *Proc Natl Acad Sci U S A* **104**, 3943-3948, (2007).

107 Paternostro, G., Vignola, C., Bartsch, D. U., Omens, J. H., McCulloch, A. D. & Reed, J. C. Age-associated cardiac dysfunction in Drosophila melanogaster. *Circ Res* **88**, 1053-1058, (2001).

108 Cannon, L., Zambon, A. C., Cammarato, A., Zhang, Z., Vogler, G., Munoz, M., Taylor, E., Cartry, J., Bernstein, S. I., Melov, S. & Bodmer, R. Expression patterns of cardiac aging in Drosophila. *Aging cell* **16**, 82-92, (2017).

109 van Berlo, J. H., Maillet, M. & Molkentin, J. D. Signaling effectors underlying pathologic growth and remodeling of the heart. *J Clin Invest* **123**, 37-45, (2013).

110 Lehmacher, C., Abeln, B. & Paululat, A. The ultrastructure of Drosophila heart cells. *Arthropod Struct Dev* **41**, 459-474, (2012).

111 Caldwell, J. T., Mermelstein, D. J., Walker, R. C., Bernstein, S. I. & Huxford, T. X-ray crystallographic and molecular dynamic analyses of Drosophila melanogaster embryonic muscle myosin define domains responsible for isoform-specific properties. *J Mol Biol* **432**, 427-447, (2020).

112 Rotstein, B. & Paululat, A. On the morphology of the Drosophila heart. *J Cardiovasc Dev Dis* **3**, (2016).

113 Nishimura, M., Ocorr, K., Bodmer, R. & Cartry, J. Drosophila as a model to study cardiac aging. *Exp Gerontol* **46**, 326-330, (2011).

114 Miyata, S., Minobe, W., Bristow, M. R. & Leinwand, L. A. Myosin heavy chain isoform expression in the failing and nonfailing human heart. *Circ Res* **86**, 386-390, (2000).

115 Lompre, A. M., Mercadier, J. J., Wisnewsky, C., Bouveret, P., Pantaloni, C., D'Albis, A. & Schwartz, K. Species- and age-dependent changes in the relative amounts of cardiac myosin isoenzymes in mammals. *Developmental biology* **84**, 286-290, (1981).

116 Viswanathan, M. C., Schmidt, W., Rynkiewicz, M. J., Agarwal, K., Gao, J., Katz, J., Lehman, W. & Cammarato, A. Distortion of the actin A-triad results in contractile disinhibition and cardiomyopathy. *Cell Rep* **20**, 2612-2625, (2017).

117 Dellefave, L. M., Pytel, P., Mewborn, S., Mora, B., Guris, D. L., Fedson, S., Waggoner, D., Moskowitz, I. & McNally, E. M. Sarcomere mutations in cardiomyopathy with left ventricular hypertrabeculation. *Circ Cardiovasc Genet* **2**, 442-449, (2009).

118 Gyimesi, M., Tsaturyan, A. K., Kellermayer, M. S. & Malnasi-Csizmadia, A. Kinetic characterization of the function of myosin loop 4 in the actin-myosin interaction. *Biochemistry* **47**, 283-291, (2008).

119 Ajtai, K., Halstead, M. F., Nyitrai, M., Penheiter, A. R., Zheng, Y. & Burghardt, T. P. The myosin C-loop is an allosteric actin contact sensor in actomyosin. *Biochemistry* **48**, 5263-5275, (2009).

120 Ajtai, K., Garamszegi, S. P., Watanabe, S., Ikebe, M. & Burghardt, T. P. The myosin cardiac loop participates functionally in the actomyosin interaction. *J Biol Chem* **279**, 23415-23421, (2004).

121 Coureux, P. D., Sweeney, H. L. & Houdusse, A. Three myosin V structures delineate essential features of chemo-mechanical transduction. *EMBO J* **23**, 4527-4537, (2004).

122 Tsukamoto, O. Direct sarcomere modulators are promising new treatments for cardiomyopathies. *Int J Mol Sci* **21**, (2019).